$$\left\{ B > \frac{1}{N} \sum_{i=1}^{N} x_i \right\}$$

«Be Greater Than Average»

Kennedy Space Center

to all the people
who believed in me

University of Messina

Department of Engineering

PhD in Engineering and Chemistry of Materials and Constructions

---

Experimental and numerical study on bond behavior in composite materials and strengthening systems

PhD student ***SantiURSO***

Tutor ***Prof.ssa Chiara Borsellino***

Co-tutor ***Prof. Ing. Antonino Recupero***

Co-tutor ***Prof. Qingda Yang***

XXXII cycle (2016-2019)

Acknowledgments

The author gratefully acknowledges Prof.ssa Chiara Borsellino and Prof. Antonino Recupero (University of Messina) for giving him the opportunity to work on this topic during his PhD studies.

The author would like to thank Prof. Antonio Nanni and Prof. Qingda Yang (University of Miami) for their priceless guidance and for giving him the opportunity to perform the experimental work at University of Miami.

The author would like to express his appreciation to Ruredil S.p.A. of San Donato Milanese, Italy, for providing the composite materials for the experimental campaign.

Index of Contents

Index of Contents ..... **i**

Index of Figures ..... **v**

Index of Tables ..... **xi**

Summary **1**

Chapter 1. Adhesive joints: an overview **3**

1.1 General aspects 3

1.2 Why to use adhesive joints 4

1.3 Adhesive types 5

1.4 Joint geometry and design criteria 7

1.4.1 Joint design criteria 8

1.4.2 Failure type 10

1.5 Cohesive Zone Model 10

Chapter 2. Experimental tests on adhesive joints **13**

2.1 Compatibility and temperature effect on hybrid bonded joints made of glass-aluminum and glass-GFRP 14

2.1.1 Materials and methods 15

2.1.2 Test set up and test program 19

2.1.3 Results and discussion 20

2.1.4 Discussion 30

2.2 Compatibility and temperature effect on hybrid painted bonded joints made of glass-aluminum 31

2.2.1 Materials and methods 31
2.2.2 Test set up and test program 34
2.2.3 Results and discussion 34
2.3 Tensile test on dog-bone specimens 36

Chapter 3. FEM Models on adhesive joints 41
3.1 Numerical model of the adhesive joint in a Tensegrity floor 41
3.1.1 Experimental test 41
3.1.2 Numerical model 44

Chapter 4. Strengthening systems with composite materials 49
4.1 Strengthening systems with externally bonded composite materials 49
4.2 Fabric Reinforced Cementitious Matrix 51
4.2.1 Design of FRCM strengthening 52
4.3 Research on strengthening systems with composite material: temperature and moisture influence 53
4.4 Numerical models on FRCM strengthening system 55

Chapter 5. Experimental tests on FRCM/FRP strengthening systems ... 57
5.1 Introduction 57
5.2 Experimental campaign 60
5.2.1 Materials 60
5.2.2 Specimens preparation 63
5.2.4 Environmental conditioning 67
5.3 Experimental results 68
5.3.1 Force-displacement curves and failure modes of beams with PBO-FRCM system 68
5.3.2 Force-displacement curves and failure modes of beams with CFRP system 71
5.4 Discussion of experimental results 74

5.4.1 Interpretation of the force-displacement curve in the PBO-FRCM system 74

5.4.2 Indirect method to evaluate the interfacial stress-slip curve for FRCM system 79

5.4.2 Influence of environmental conditioning on the CFRP system 82

5.5 Conclusion 84

Chapter 6. FEM Models of FRCM 87

6.1 2D Finite Element model using Augmented-FEM 87

6.1.1 Introduction 87

6.1.2 Augmented Finite Element Method (A-FEM) 90

6.1.3 Assumptions and simplifications 92

6.1.4 Numerical and experimental results of direct tensile 98

6.1.5 Parametric study and comparison 100

6.1.6 Single-lap shear test (SLS) 103

6.1.7 Results of single-lap shear test model 103

6.1.8 Conclusion 105

6.2 3D Finite Element model using Augmented-FEM 106

6.2.1 Introduction 106

6.2.2 Assumptions and simplifications 106

6.2.3 Calibration of a new cohesive law 112

6.2.4 Comparison with experimental results (SLS) 118

6.2.5 Discussion and conclusion 121

Conclusions 123

Bibliography 125

Index of Figures

Figure 1.1 Adhesive classification 6

Figure 1.2 Most common configurations of adhesive joints 8

Figure 1.3 Loading condition for adhesive joints 8

Figure 1.4 Tensile force on lap joint showing (a) unloaded joint, (b) joint under stress, and (c) stress distribution in adhesive. 9

Figure 1.5 Failure type: (a) adhesive failure; (b) cohesive failure; (c) mixed failure. 10

Figure 1.6 Different cohesive laws 11

Figure 2.1 Double-lap specimens geometry 18

Figure 2.2 a)Testing machine; b) Specimen positioning. 19

Figure 2.3 Representative load-displacement curves of glass-aluminum double-lap specimens, bonded with three epoxy adhesives (a), and three acrylic adhesives (b). 21

Figure 2.4 Representative load-displacement curves of glass-GFRP double-lap specimens, bonded with three epoxy adhesives (a), and three acrylic adhesives (b). 22

Figure 2.5 Comparison between mechanical trends at different temperatures of glass-aluminum adhesive joints. 24

Figure 2.6 Comparison between mechanical trends at different temperatures of glass-GFRP adhesive joints. 25

Figure 2.7 Percentage reduction of the maximum carried load of the aluminum/glass double lap joint at high temperatures: a) Tw and b)Tm 25

Figure 2.8 Percentage reduction of the maximum carried load of the GFRP/glass double lap joint at high temperatures: a) Tw and b)Tm 26

Figure 2.9 Failure modes of glass-GFRP/aluminum double lap joints: adhesive failure. 27

Figure 2.10 Failure modes of glass-GFRP/aluminum double lap joints: cohesive failure. 27

Figure 2.11 Failure modes of glass-GFRP/aluminum double lap joints: light-fiber-tear failure. 28

Figure 2.12 Failure modes of glass-GFRP/aluminum double lap joints: mixed failure. 28

Figure 2.13 Comparison between mechanical trends at different temperatures of two combinations: (a) glossy aluminum-painted glass: (b) glossy aluminum-transparent glass. 35

Figure 2.14 Test specimen, adapted from UNI EN ISO 527-2. 36

Figure 2.15 Stress strain curve of dog-bone specimens at environmental temperature 37

Figure 2.16 Stress strain curve of dog-bone specimens at work temperature (Tw=50 °C) 37

Figure 2.17 Stress strain curve of dog-bone specimens at maximum service temperature (Tm=80°C) 37

Figure 2.18 Comparison on stress-strain characteristic curve at the three test temperatures 39

Figure 2.19 Typical failure mode of tensile test on dog-bone specimen 40

Figure 3.1 Geometric configuration of the hybrid system [mm] 42

Figure 3.2 Cyclic load for flexural test 42

Figure 3.3 Flexural test: a) test set-up; b) static model; c) transducers position. 43

Figure 3.4 FEM model 44

Figure 3.5 Mesh configuration: a) whole system; b) particular of the meshed joint 45

Figure 3.6 Displacement color map 46

Figure 3.7 Stress map of whole system 47

Figure 4.1 Example of FRP strengthening applied on a concrete substrate 50

Figure 4.2 Example of FRCM application 52

Figure 4.3 Direct tensile test setup per AC434 53

Figure 4.4 Variation of Modulus E with Temperature 54

Figure 4.5 3D numerical model for direct tensile test according to AC434 55

Figure 5.1 Representative carbon sheet and PBO grid used in the experimental campaign 62

Figure 5.2 Curing process of the specimens: a) after demolding; b) wrapping of specimens to prevent evaporation of water during the 28 days curing time..... 63

Figure 5.3 Specimen dimensions according to ASTM D7958/D7958M (2017) regulations (dimensions in mm): a) front view; b) bottom view..... 64

Figure 5.4 Preparation of concrete beams before application of the strengthening system 64

Figure 5.5 Application of FRP system: a) application of primer; b) application of first layer of resin; c) application of carbon fabric; d) application of second layer of resin..... 65

Figure 5.6 Application of the FRCM system: a) wet of bonding area; b) application of first layer of mortar; c) application of PBO grid; d) application of second layer of mortar 66

Figure 5.7 Test setup: a) front view of the specimen in three-point bending test configuration; b) details of the LVDT for the deflection measurement 67

Figure 5.8 Layout of the environmental conditioning phase in curing tank at controlled temperature..... 67

Figure 5.9 Force-displacement curves of non-conditioned beam specimens with PBO-FRCM system..... 69

Figure 5.10 Force-displacement curves of beam specimens with PBO-FRCM system conditioned at temperature Tw=30°C..... 69

Figure 5.11 Force-displacement curves of beam specimens with PBO-FRCM system conditioned at temperature Tc=50°C..... 70

Figure 5.12 Typical failure of PBO-FRCM strengthened beams with significant elongation of the PBO fibers and mortar keeping attached to the concrete substrate..... 71

Figure 5.13 Force-displacement curves of non-conditioned beam specimens with CFRP system 72

Figure 5.14 Force-displacement curves of beam specimens with CFRP system conditioned at temperature Tw=30°C..... 72

Figure 5.15 Force-displacement curves of beam specimens with CFRP system conditioned at temperature Tc=50°C..... 73

Figure 5.16 Typical failure of CFRP-strengthened beams with adhesive failure for Tc=50°C conditioning, and adhesive failure accompanied by partial concrete detachment for nc and Tw=30°C conditioning..... 74

Figure 5.17 Representative Force-displacement curve of notched beam specimens 75

Figure 5.18 Distribution of strains and stresses in the mid-span cross-section of the beam for identification of load level of point A..... 76

Figure 5.19 Influence of the environmental conditioning on the first peak load FA (left) and on the second peak load Fc (right) of the Force-displacement curve of beams with PBO-FRCM system 79

Figure 5.20 Analysis of right-body motion of the PBO-FRCM strengthened beam and evaluation of rotation angle for the determination of the stress-global slip curve of the bond behavior 80

Figure 5.21 Stress-global slip curve obtained by processing the force-displacement results of the notched beam test setup for FRCM_nc_1 specimen 82

Figure 5.22 Influence of the environmental conditioning on the peak load (Fmax) of the Force-displacement curve of CFRP-strengthened beams 83

Figure 6.1 Direct tensile test setup configuration according to AC434 88

Figure 6.2 Single-lap Shear test setup configuration according to Rilem 89

Figure 6.3 Six different failure mode for Single-Lap Shear test 90

Figure 6.4 Illustration of an element from (a) a regular element, to (b) an A-FE with two quadrilateral sub- domains, or to (c) an A-FE with one triangular sub-domain and one pentagonal sub-domain 91

Figure 6.5 Real cross-section of sample for direct tensile test [mm], (b) Homogenized model geometry 93

Figure 6.6 (a) Top view of the fabric mortar geometry, (b) detail of contribution of mortar within and fabric 93

Figure 6.7 Single layer specimen for direct tensile test [mm] according to AC434 94

Figure 6.8 Mesh size of different elements [mm] – schematic figure 94

Figure 6.9 boundary and conditions for direct tension simulation 95

Figure 6.10 Shape of fracture laws for Mode I and Mode II 96

Figure 6.11 Cohesive traction-separation law 97

Figure 6.12 Cohesive laws 98

Figure 6.13 Numerical stress-strain curve 99

Figure 6.14 Experimental results: a) one layer, b) two layers, c) three layers 100

Figure 6.15 Comparison of stress-strain curves with different cracks number 101

Figure 6.16 Comparison between experimental and numerical results (DT) – a) one ply model, b) two plies model, c) three plies model 102

Figure 6.17 Geometry on Single-Lap Shear test specimen [mm] 103

Figure 6.18 Comparison between 2D numerical and experimental results (SLS) 104

Figure 6.19 Theoretical curve that describe bond mechanism..... 104

Figure 6.20 Evolution of bond length 105

Figure 6.21 Schematic representation of elements of the models..... 107

Figure 6.22 Element illustration for (a) a regular 4-node tetrahedron element with two possible different crack planes; (b) an A-FE with a tetrahedron and a wedge sub-domains; (c) an A-FE with two wedge sub-domains. 108

Figure 6.23 Building of a brick element through six tetrahedron elements 109

Figure 6.24 Mortar layers 109

Figure 6.25 Fabric yarns..... 110

Figure 6.26 "Link-cohesive elements" 110

Figure 6.27 Cohesive laws for (a) (matrix) shear damage mode; (b) fiber tensile rupture/compressive kinking damage mode; (c) matrix tension/compression damage mode. 111

Figure 6.28 Cohesive law proposed by D'Antino et al. (2018) 112

Figure 6.29 Comparison between numerical and experimental results (DT) ... 113

Figure 6.30 Cohesive laws with τ=0.6 - parametric study on the stiffness of the first branch (k1) 114

Figure 6.31 Comparison between numerical and experimental results (DT), first parametric study (τ=0.6) 114

Figure 6.32 Cohesive laws with τ=0.5 - parametric study on the stiffness of the first branch 115

Figure 6.33 Comparison between numerical and experimental results (DT), second parametric study (τ1=0.5)..... 115

Figure 6.34 Cohesive laws with τ1=0.7 - parametric study on the stiffness of the first branch 116

Figure 6.35 Comparison between numerical and experimental results (DT), third parametric study (τ1=0.7) 116

Figure 6.36 Cohesive laws with τ1=0.6 and τ2=0.06 - parametric study on the stiffness of the second branch 117

Figure 6.37 Comparison between numerical and experimental results (DT), third parametric study (τ1=0.6) 117

Figure 6.38 Comparison between three different cohesive laws with fixed first branch stiffness and varying τ1 (0.5, 0.6 and 0.7)..... 118

Figure 6.39 Comparison between numerical and experimental results (DT), (τ1=0.5, 0.6 and 0.7), ... 118

Figure 6.40 A-FEM configuration of the SLS test set up 119

Figure 6.41 Comparison between 3D numerical and experimental results (SLS) 119

Figure 6.42 Evolution of bond length 120

Index of Tables

Table 2.I Nomenclature 15

Table 2.II Glass mechanical properties according to manufacture' s data sheet 16

Table 2.III Aluminum mechanical properties according to manufacture' s data sheet 16

Table 2 IV GFRP mechanical properties according to manufacture' s data sheet 16

Table 2.V Technical and mechanical characteristics of the adhesives reported by manufacturers 17

Table 2.VI Test program 20

Table 2.VII Mechanical properties of the glass-aluminum double-lap specimens 21

Table 2.VIII Mechanical properties of the glass-GFRP double-lap specimens. 21

Table 2.IX Mechanical properties of the glass-aluminum double-lap specimens at high temperatures 23

Table 2.X Mechanical properties of the glass-GFRP double-lap specimens at high temperatures. 23

Table 2.XI Failure modes of aluminum-glass double lap joints 29

Table 2.XII Failure modes of GFRP-glass double lap joints 30

Table 2.XIII Glass mechanical properties according to manufacturer's data sheet 32

Table 2.XIV Aluminum mechanical properties according to manufacturer's data sheet 32

Table 2.XV Typical uncured physical properties 32

Table 2.XVI Typical cured thermal properties 33

Table 2.XVII Test program 34

Table 2.XVIII Mechanical properties of the double-lap specimens at three temperatures. 34

Table 2.XIX Stiffness of the double-lap specimens at three temperatures. 35

Table 2.XX Different test specimens, adapted from UNI EN ISO 527-2. 36

Table 2.XXI Mechanical properties of adhesive EPX4 38

Table 2.XXII Young Modules of adhesive EPX4 38

Table 3.I Glass and steel properties according to manufacturer's data sheet 44

Table 3.II Data of mechanical properties in tensile test of the adhesives 46

Table 3.III Displacement of hybrid samples, experimental and FEM results 46

Table 5.I Concrete compressive strength 61

Table 5.II Concrete flexural strength 61

Table 5.III Mechanical properties of mortar used in the PBO-FRCM system .. 61

Table 5.IV Mechanical and geometrical properties of the PBO-FRCM grid system 62

Table 5.V Mechanical properties of primer and epoxy used in the CFRP system 62

Table 5.VI Mechanical properties of CFRP system 62

Table 5.VII Test program 68

Table 5.VIII Experimental results of three-point bending tests on beams with PBO-FRCM system 79

Table 5.IX Experimental results of three-point bending tests on beams with CFRP system 83

Table 6.I Mechanical properties of PBO fabric and mortar 95

Table 6.II Fracture properties of mortar 95

Table 6.III Mortar fracture parameters 97

Table 6.IV Mechanical and fracture properties of concrete block 103

Summary

The mechanism of stress transfer across different materials bonded each other is one of the most discussed topic in research field. Different approaches can be used in order to study this topic: analytical approach, experimental approach and numerical approach.

In this thesis these approaches are applied in order to study the bonding mechanism in various engineering field.

In the first part, the attention is focused on adhesive joints for mechanical application in which aluminum, GFRP and glass materials are used. Two experimental campaigns are performed in order to evaluate the mechanical performances of double-lap joints using different type of adhesives and adherends. The influence of temperature on joint performances is also studied and results show the strong influence of this parameter on the mechanical strength of the adhesive joint.

In a third experimental study, the mechanical performance of the adhesive joints in a steel-glass connection is investigated. The aim of part is to verify the applicability of the adhesive bonds on a tensegrity floor; that is a hybrid system characterized by a particular steel-glass adhesive junction that permits an effective cooperation between the two structural elements (a glass panel and a steel subframe). Experimental tests on hybrid system are performed with a stepwise cyclic loading and a numerical validation of the whole system is done through a Finite Element Model of the tested samples.

The second part of the dissertation is focused on new strengthening systems for civil application. In the last few decades, the construction industry has had a rapid expansion of interest regarding strengthening and retrofitting of existing reinforced concrete (RC) and masonry structures. In fact, new strengthening systems for existing structures were investigated e optimized in terms of efficiency, easy application, durability and cost.

Externally bonded composite materials, FRP (Fiber Reinforced Polymer) and FRCM (Fabric Reinforced Cementitious System), are studied in this section. The bond behavior between composite system and concrete substrate is investigated. An experimental campaign on strengthened beams with FRP (carbon sheet fibers) and FRCM (PBO fabric) applied at different environmental

conditions are conducted in order to study the durability problems. Results, in term of force-displacement curve, are interpreted with an analytical approach.

Finally, numerical models on FRCM system are carried out in order to develop a tool aimed to the optimization of the system. Augmented-FEs are implemented in numerical codes and used for 2D and 3D models. Tensile behavior of FRCM coupon is numerically simulated in all three stages of its characteristic behavior. Results of this study show a good agreement with experimental ones.

The last part is focused on developing a new cohesive law, calibrated on experimental results, for 3D models of FRCM system. Parametric studies are conducted and then the proposed approach is validated by modeling different test setup.

Chapter 1

Adhesive joints: an overview

The main aim of this Chapter is to give general, preliminary definitions that may be useful in reading this thesis. Different type of adhesives, their failure mode and analysis methods are following described. The concept is to introduce the problem of bonding between different materials in the field of mechanical application but they have found application also in other different field like civil application.

1.1 General aspects

The gluing technique allows to connect permanently two different substrates, joined by an adhesive. The adhesive is defined as a non-metallic material, capable of connecting different materials by surface fixation (adhesion) in order to obtain a joint that has enough internal strength (cohesion).

In the cohesion zone, the adhesive is present in its normal state. In the adhesion zone, the adhesive has a modified structure and composition due to adhesion to the substrate surfaces. The structure and composition are different from those found in the cohesion area. As a consequence, also the macroscopic properties of the adhesive in the adhesion zone will be different.

In the transition zone, between the adhesion and cohesion areas, the structure, composition and macroscopic properties of the adhesive continuously change.

Adhesion zone

The adhesive has a modified molecular structure in the adhesion zone due to the bonding on the substrate surface. The adhesion phenomenon is caused by the molecular interactions between the substrate surface and the adhesive.

Chemical bonds are formed, however, only in the presence of very few substrate/adhesive combinations. It has been shown for some of these glued

joints that chemical bonds account for up to 50% of all interactions. The long-term stability of these bonds depends directly on their resistance to moisture.

Nevertheless, in addition to the chemical and intermolecular adhesion forces, also the bonding mechanism called "micromechanical adhesion" can have effects, depending on the morphology of the substrate surface. In general, "micromechanical adhesion" is considered of secondary importance. However, if there are regular interstices on the substrate - possibly created for design reasons - in which the adhesive penetrates, the joint strength is increased.

Transition zone

The transition zone, in which the chemical, mechanical and optical properties of the adhesive are altered, has a variable thickness, from some nanometers up to some millimeter extensions. The thickness depends on the nature of the substrate surface, the adhesive and the hardening conditions. If large transition zones or thin glued joints are present, the behavior of the entire glued joint may depend on the properties of the transition zone since in this case there is no cohesion zone.

Cohesive zone

In the cohesion area, the adhesive has the nominal properties shown in the data sheet. These properties depend on the following molecular forces:

- Molecular bonds within polymers;
- Chemical bonds deriving from polymer cross-linking;
- Intermolecular interactions between molecules in the adhesive;
- Mechanical fastening between various molecules in the adhesive.

Just like in a chain, the weakest link in a glued joint determines which loads the joint can withstand.

1.2 Why to use adhesive joints

As discussed in the previous parts, adhesive bonding is a useful technique because has many advantages:

- uniform distribution of stress and largest stress-bearing area;
- allow to join materials of any shape, similar and dissimilar;
- resist fatigue and cyclic loads;

- seal joints against a variety of environments;
- insulate against heat transfer and electrical conductance;
- the heat required to set the joint is usually too low to reduce the strength of the metal parts;
- dampen vibration and absorb shock;
- quicker and/or cheaper to form than mechanical fastening.

Clearly there are also many disadvantages:

- the bond doesn't permit visual examination of the bond area;
- careful surface preparation is required to obtain durable bonds;
- exposure to solvents used in cleaning or solvent cementing may present health problems;
- the useful life of the adhesive joint depends on the environment to which it is exposed;

The basic requirements for a good adhesive bond are:

- proper choice of adhesive;
- good joint design;
- cleanliness of surfaces: wetting of surfaces that are to be bonded together;
- proper adhesive bonding process (solidification and cure).

1.3 Adhesive types

All the most popular adhesives can be classified according to their chemical composition, source, function and physical form, as summarized in Figure 1.1.In particular:

- Natural adhesives, including materials of animal or vegetable origin;
- Thermoplastic adhesives, including natural and synthetic resins;
- Thermosetting adhesives, based on synthetic polymers;
- Elastomeric adhesives, including rubber-like materials of natural or synthetic origin;
- Biopolymer adhesives, generally consisting of elements of previous categories

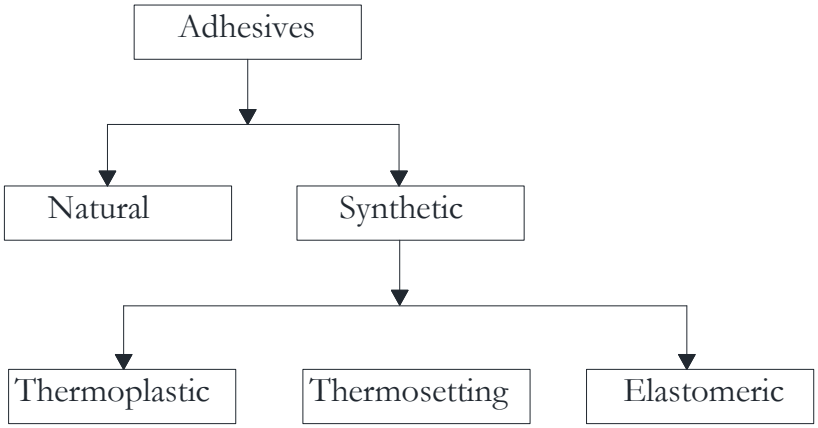

Figure 1.1 Adhesive classification

Natural adhesives

They are the simplest, commonly used and they resulting from animals and plants. They are characterized by a good resistance to heat and to chemical agents, on the contrary, to a poor resistance to moisture. They can be used only for paper bonding and industrial packaging.

Thermoplastic adhesives

Thermoplastic resins are linear or branched polymers that can be melted due to an appropriate amount of heat, as well as at high temperature they are subject to softening, instead under tension they are subjected to viscous sliding. They can be forged and re-forged in any form with techniques such as injection molding and extrusion. These polymers, whose fusion is obtained through heat, thanks to a contact with the walls of the mold, solidify for cooling without causing any problem to the performance of the resin. The thermoplastic polymers can be characterized by two different phases: an amorphous phase and a crystalline one. The first is characterized by the glass transition temperature, T_g, the temperature that marks the transition from a glassy state to a rubbery one. The second one is characterized by a melting temperature, T_m, representative of the passage from an ordered state, crystalline solid, to a disordered state, liquid.

Thermosetting adhesives

These adhesives solidify by polymerization thanks to the action of the curing agents (first of all heat and chemical catalysts), like thermoplastic adhesives, but,

unlike the latter, they cannot be melted and processed after the first cooling, because they would face degradation and decomposition. The thermosetting adhesives produce stronger adhesives than other adhesives and they are therefore more suitable for certain structural components. The properties of viscous sliding and shear strength are good, but the peeling resistance is discreet, furthermore the glues are brittle and have low impact strength.

Elastomeric adhesives

Elastomers, more commonly called "rubbers", are materials capable of undergoing big deformations under the action of relatively small loads, and returning to their original shape once the effort has ended.

1.4 Joint geometry and design criteria

The main aim of adhesive joints is to transfer the load between the structural elements as efficiently as possible and within the safety limits. Bonding often produces joints that are more reliable in operation and cheaper than those made with conventional connections. A safe design must not exceed the strength and durability limits of the adhesive and the structure while maintaining a light and economical configuration, complying with safety standards codes. In order to optimize the performance of a project, general principles have to be followed:

- Stress the adhesive in the direction of maximum resistance;
- provide for the maximum bonding area;
- make the adhesive layer as uniform as possible;
- maintain a thin and continuous adhesive layer;
- avoid stress concentrations.

The importance of the thickness of the adhesive film is in its influence on the resistance of the joint, in fact thin layers demonstrate high shear strength. The most common configurations of a bonded composite-composite or metal-composite joints are (see Figure 1.2):

- single-lap joint;
- double-lap joint;
- single-strap joint;
- double-strap joint;
- Scarf joint.

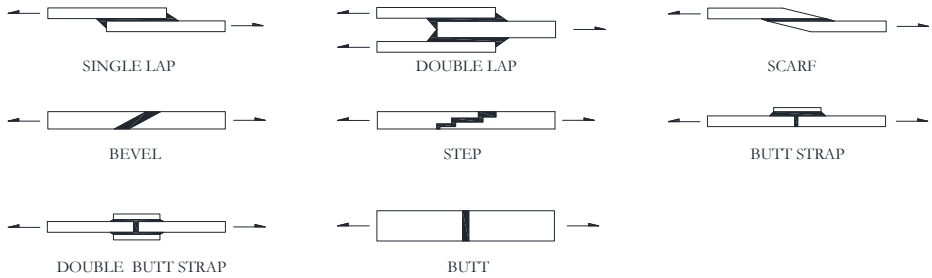

Figure 1.2 Most common configurations of adhesive joints

Is important to know the right stress distribution of the joint in order to obtain a good adhesion and for this reason there are two rules:

- to use the maximum area in order to increase the strength of joint;
- to choose the best geometry according to joint design.

An adhesive joint can be subject to different loading condition. There are five different loading condition as shown in Figure 1.3:

a. Compression
b. Tension
c. Shear
d. Peel
e. Cleavage

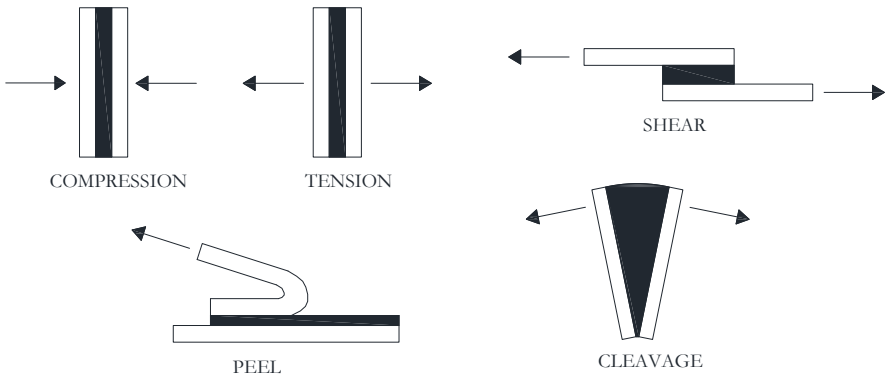

Figure 1.3 Loading condition for adhesive joints

1.4.1 Joint design criteria

The bonded area should be large enough to resist the greatest force that the joint will be subjected to in service. The calculation of stress in the adhesive joint is not a reliable way of determining the exact dimensions required. It is relatively

difficult to decide on an allowable stress. The strength of the bond is affected by environmental conditions, age, temperature of cure, composition and size of adherends, and the thickness of the adhesive layer.

The stress in the adhesive is ordinarily a combination of various stresses, in Figure 1.4 is described the stress distribution in a single lap joint. The relative flexibility of the adhesive to that of the adherends has a pronounced effect on the stress distribution. The greater part of the lap (adjacent to the center) carries a comparatively low stress. Therefore, if the overlap length is doubled, the load-carrying capability of the joint is increased by a relatively low percentage. The greatest gain in strength is obtained by increasing the joint width. Increasing the width of the joint results in a proportionate increase in strength, while increasing the overlap length (*L*) beyond a certain limit has very little effect.

In addition to overlap length and width, the strength of the lap joint is dependent on the yield strength of the adherend. The modulus and thickness of the adherend determine its yield strength, which should not exceed the joint strength. The yield strength of thin metal adherends can be exceeded where an adhesive with a high tensile strength is employed with a relatively small joint overlap.

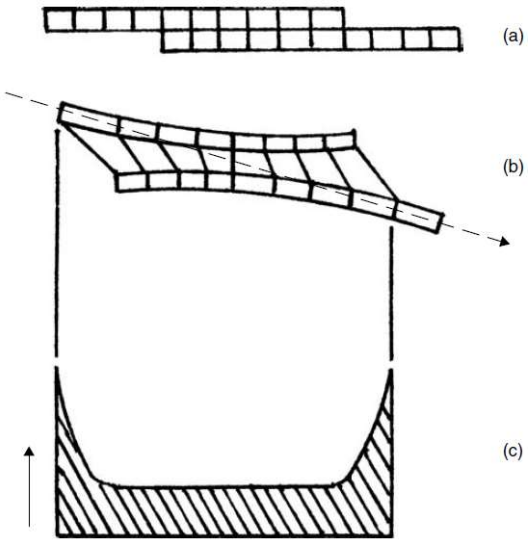

Figure 1.4 Tensile force on lap joint showing (a) unloaded joint, (b) joint under stress, and (c) stress distribution in adhesive.

1.4.2 Failure type

When the joint is subjected to a load during destructive tests, the adhesive will separate from the substrate through three types of breakage: adhesive, cohesive and mixed as shown in Figure 1.5.

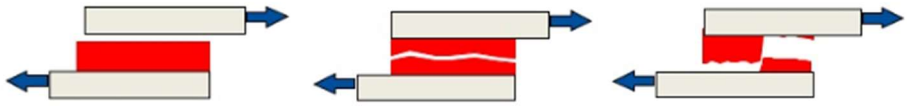

(a) (b) (c)

Figure 1.5 Failure type: (a) adhesive failure; (b) cohesive failure; (c) mixed failure.

Failure mode depends by several variables, like adhesive, substrates, surface preparation, temperature, environmental condition and by the stress distribution among the junction. For this reason, it's important study the functionality of joints in its configuration by experimental, numerical and analytical approach.

1.5 Cohesive Zone Model

The Cohesive Zone Model (CZM) describes material separation with a traction-separation law and links the micro-structural failure mechanism to the continuum deformation field.

CZM offers an alternative way to assess failure in materials or along material interfaces. It is a phenomenological model instead of an exact physical representation of material behavior in the fracture process zone, where distributed micro-cracking or void formation takes place.

The Cohesive Zone Model (CZM) removes the crack tip singularity and represents physics of the fracture process at the atomic scale. It regards fracture as a gradual phenomenon in which material separation takes place across an extended crack tip (cohesive zone) and is resisted by cohesive forces. A cohesive traction-separation law governs the constitutive behavior of crack opening in addition to the bulk stress-strain relation of surrounding material. No additional criterion is needed for fracture to occur. New crack surfaces are created as a natural result of constitutive evolvement, thus maintaining continuity conditions mathematically despite the physical separation. Furthermore, the CZM is able not only to represent the toughness at the crack tip but also to describe the entire fracture process including crack initiation and propagation. The presence of an initial crack is not essential as is required, instead, by conventional fracture mechanics.

Despite the fact that the CZM is a phenomenological model and does not define the actual physical process of fracture, the validity of the method has been witnessed in various applications. Over the years, the CZM has been successfully applied for studying and rationalizing crack growth simulation in materials spanning the domains of metals, concretes, ceramics, polymers, and their composite counterparts. It has been used to describe micromechanical separation processes such as void growth and nucleation, atomic separation.

Different shapes of cohesive laws are available in literature and implemented in the softwares for FEM analysis as shown in Figure 1.6.

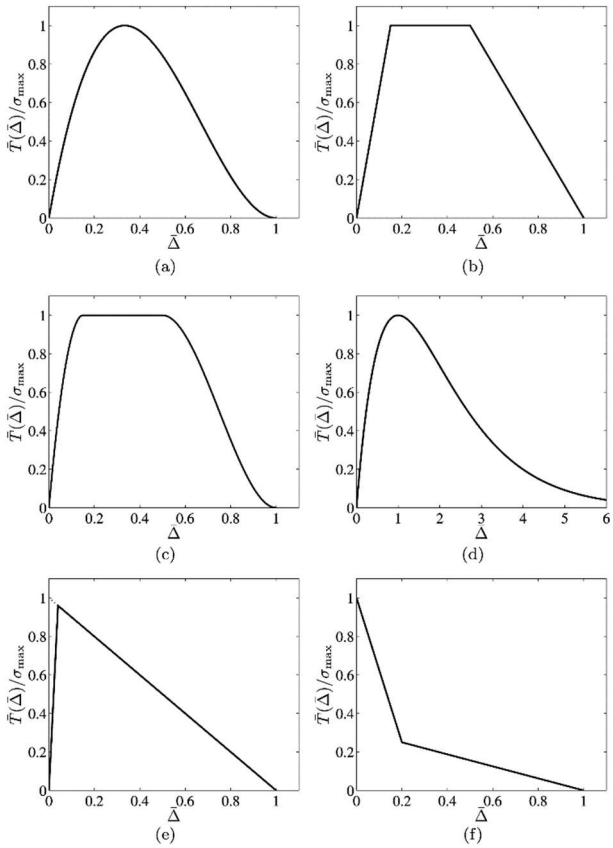

Figure 1.6 Different cohesive laws

Cohesive laws are in important in order to describe interface behavior between adhesive and substrate and they are used in FEM codes. In the FE models herein analyzed, further discussed in the next chapters, cohesive laws were used in order to connect different materials.

Chapter 2

Experimental tests on adhesive joints

In this Chapter, a series of mechanical tests were conducted on different type of specimens. Tensile tests were done on double-lap joint and tensile test on bone dog specimen. Different types of adhesives (epoxy and acrylic) were compared and three temperature conditions (room temperature, work temperature and maximum service temperature) were investigated.

The first part of the experimental study describes the results of tensile tests conducted in order to verify the compatibility of the bonding system at room temperature, then, the second part illustrates the degradation of the adhesive bonding due to high temperatures.

The results evidenced that the mechanical performance of adhesive junctions is considerably reduced as the temperature increases. This phenomenon is more evident in acrylic adhesives rather than epoxy ones. The highest load carrying capacity was always obtained with the epoxy adhesives, while the acrylic ones showed the highest joint elongations. The different failure modes, observed at room temperature, were classified as:

- Adhesive Failure (AF);
- Cohesive Failure (CF);
- Light-Fiber-Tear Failure (LFTF);
- Mixed Failure (MF).

At high temperatures, only "adhesive failure" were observed. The experimental campaign demonstrates that high temperatures have a remarkable impact on the mechanical properties of adhesive junctions. Such effect should be taken into account suitably in the design and verification phase of components.

Results of tensile tests on dog-bone specimens have shown that at different test temperatures, mechanical behavior changes not only in terms of reduction of maximum strength but also in terms of different constitutive behavior.

2.1 Compatibility and temperature effect on hybrid bonded joints made of glass-aluminum and glass-GFRP

In the field of civil and mechanical engineering, in the last decades, an increasing interest has been addressed towards new building materials, such as Glass Fiber-Reinforced Polymer (GFRP) (Stazi et al. 2016a), structural adhesives (Stazi et al. 2015), solar control glass coatings (Stazi et al. 2016b) and structural glass. GFRP can be used in alternative to conventional materials in bridges and buildings (Keller 2001), electricity transmission towers (Godat et al. 2013), and windows frames (Appelfeld et al. 2010, Dispenza et al. 2006). Structural glass has been utilized for wall façade system, glass floor (Overend et al. 2011), glass columns and beams (Foraboschi 2007, Bati et al. 2009, Biolzi et al. 2010 and Speranzini & Agnetti 2013). GFRP pultruded profiles present several advantages if compared to traditional materials, for example high specific yield strength, light weight, low electrical and thermal conductivity and non-corrodibility, rapid installation time and low life-cycle costs (Godat et al. 2013, Hollaway 2010 and Wu et al. 2015). At the same time, several factors, like their orthotropic nature (Turvey 2013), the brittleness in bolted connections (de Castro & Keller 2008a and 2008b), and the low elastic modulus if compared to steel (up to ten times lower, see (Wu et al. 2015, Kim & Lee 2012 and Qureshi & Mottram 2013), make impossible to apply GFRP to many applications, especially when concentrated bearing loads are applied (Wu & Bai 2014, Borowicz & Bank 2010 and Turbey & Zhang 2006). Furthermore, the extreme sensitivity of GFRP to fire remains a problem of great complexity. With regard to structural glass joined with other materials, its intrinsic brittle behavior makes the classic bolted connection not suitable, so the adhesive conjunction should be preferred. The new capabilities of adhesives led to the development of hybrid structures composed of glass and steel (Machalická & Eliášová 2017) An extended experimental campaign demonstrated the effectiveness of an adhesive junction between two GFRP profiles (Stazi et al. 2015) and between GFRP profiles and steel (Giampaoli et al. 2017).

However, even if adhesive bonding is suitable to be used for bonding dissimilar materials, it is necessary to consider that these materials may have very different coefficients of thermal expansion (Da Silva 2010 and Marques et al. 2015). This implies that in the design phase of the adhesive joint not only the mechanical acting forces should be taken into account, but also the elements to which it is exposed during service. Mechanical stress, elevated temperatures, and high relative humidity can be a fatal combination for certain adhesives if all occur at the same time. In particular, it is important to consider thermal effects because these generally lead to a joint strength reduction (Apalak et al. 2003, Srivastava

2003, Al-Samhan & Darwish 2005 and Viana et al. 2017) even though in some cases the opposite happens (Da Silva et al. 2004 and San Román 2005). In this first experimental campaign, the mechanical properties of two hybrid adhesive, i.e. glass-aluminum and glass-GFRP are studied.

The first aim of the study is verifying the compatibility of the bonding system at room temperature, through tensile tests on double-lap specimens with different adhesives (three epoxy and three acrylic), in order to select the best product. Then, since different materials with different thermal expansion coefficients are tested, the second aim of the research work is quantifying the decay of the mechanical performances as the temperature rises. To this purpose, further tests were carried on at various temperature conditions, i.e. work temperature and maximum service temperature,

The experimentation demonstrates that high temperatures affect considerably the mechanical properties of hybrid adhesives junctions, the experiments and the outcomes to justify this statement are thoroughly presented and discussed in the following sections.

2.1.1 Materials and methods

In this section, the used materials and the experimental conditions are presented. Table 2.Isummarizes the nomenclature used in this section.

Table 2.I Nomenclature

α	Thermal coefficient of expansion
ACR1-2-3	First, second and third acrylic adhesive
A_t	Application temperature
EPX1-2-3	First, second and third epoxy adhesive
E_t	Young modulus in tension
k	Stiffness
S_t	Service temperature
W_t	Working time at 22 °C
ε_t	Tensile strain
σ_t	Tensile strength
σ_{ys}	Tensile yield strength
τ	Shear strength
T_g	Glass transition temperature

In order to verify the compatibility and the temperature effect of glass-aluminum/glass-GFRP junctions, tensile tests on adhesively bonded double lap joints were conducted.

Adherends

Three different materials were used in this work, float glass, aluminum, and GFRP. The mechanical properties of the three materials, provided by the manufacturers, are reported in Table 2.II, Table 2.IIIandTable 2 IV.

Table 2.II Glass mechanical properties according to manufacture' s data sheet

Glass		
α	E_t	σ_t
[°C^{-1}]	[GPa]	[MPa]
9x10^{-6}	75	40

Table 2.III Aluminum mechanical properties according to manufacture' s data sheet

Aluminum profiles				
α	E_t	σ_{ys}	σ_t	ε_t
[°C^{-1}]	[GPa]	[MPa]	[MPa]	[%]
23.2x10^{6}	69	250	295	8

Table 2 IV GFRP mechanical properties according to manufacture' s data sheet

Gfrp profiles			
α	E_t	σ_t	ε_t
[°C^{-1}]	[GPa]	[MPa]	[%]
11x10^{-6}	26	400	1.5

Notice that the used GFRP profiles are made of pultruded E-glass fiber reinforced vinyl ester composite; this material consists of alternating layers of unidirectional fiber roving and chopped strand mat embedded in vinyl ester matrix. A polyester surface veil is used to protect the matrix against environmental actions.

Adhesives

Nowadays, there is still a lack of guidelines and standards for selecting suitable adhesives to be used in glass-aluminum and/or glass-GFRP joints. For this reason, it's important investigate the mechanical performance of junction with different nature of adhesives in order to find the best combination and

optimize the it. In this work six different adhesives, from two different manufacturers, three epoxy (*EPX*) and three acrylic (*ACR*), were selected, namely:

- 3M™Scotch-Weld™ Epoxy Adhesive 7260 F/C (EPX1);
- Gurit Spabond 340LV (EPX2);
- Gurit Spabond 345 (EPX3);
- 3M™ VHB ™ Tape 4941 (ACR1);
- 3M™ VHB ™ Tape 4950 (ACR2);
- 3M™ VHB ™ Tape 4991 (ACR3).

The products were chosen following two criteria:

i. the adhesive should be suitable for glass-aluminum/ glass-GFRP connections;
ii. the set of adhesives should be heterogeneous in load capacity, stiffness and thermal coefficient of expansion.

Table 2.Vsummarizes the technical and mechanical characteristics of the selected adhesives reported by manufacturers data sheet.

Table 2.V Technical and mechanical characteristics of the adhesives reported by manufacturers

Adhesives	EPX1	EPX2	EPX3	ACR1	ACR2	ACR3
Chemical base	Two-part epoxy adhesive	Two-part epoxy adhesive	Two-part epoxy adhesive	Acrilyc	Acrilyc	Acrilyc
Consistency	Controlled flow	Pasty	Pasty	Tape	Tape	Tape
W_t [min]	90-300	16	17	/	/	
A_t [°C]	15-25	15-25	15-25	21-38	20-40	21-38
S_t [°C]	-50+120	-40+80	-40+84	-35+90	-35+110	-35+90
T_g [°C]	73	55	54.6	/	/	/
α [°C^{-1}]	1x10^{-4}	/	/	18x10^{-5}	18x10^{-5}	18x10^{-5}
Surface treatments	Sand	Sand and degrease	Sand and degrease	Sand and degrease	Sand and degrease	Sand and degrease
τ^* [MPa]	33.50	29.40	36.60	0.48	0.55	0.45
σ_t [MPa]	/	/	/	0.59	0.97	0.48
E_t [MPa]	3000	1800	2600	0.9	1.8	0.9
ε_t [%]	3	/	/	/	/	
Use	Structural	Semi-structural	Semi-structural	Structural	Structural	Structural

Experiments

The experimental tests consist in tensile test on adhesively bonded glass-GFRP and glass-aluminum double lap joints. Such tests allow evaluating the compatibility between glass-aluminum and glass-GFRP and comparing the mechanical behavior of the double lap joints bonded with three epoxy and three acrylic adhesives, in terms of their load carrying capacity, displacement, and stiffness. The specimens were manufactured according to ASTM D5573-99(2019); the used geometry is illustrated in Figure 2.1.

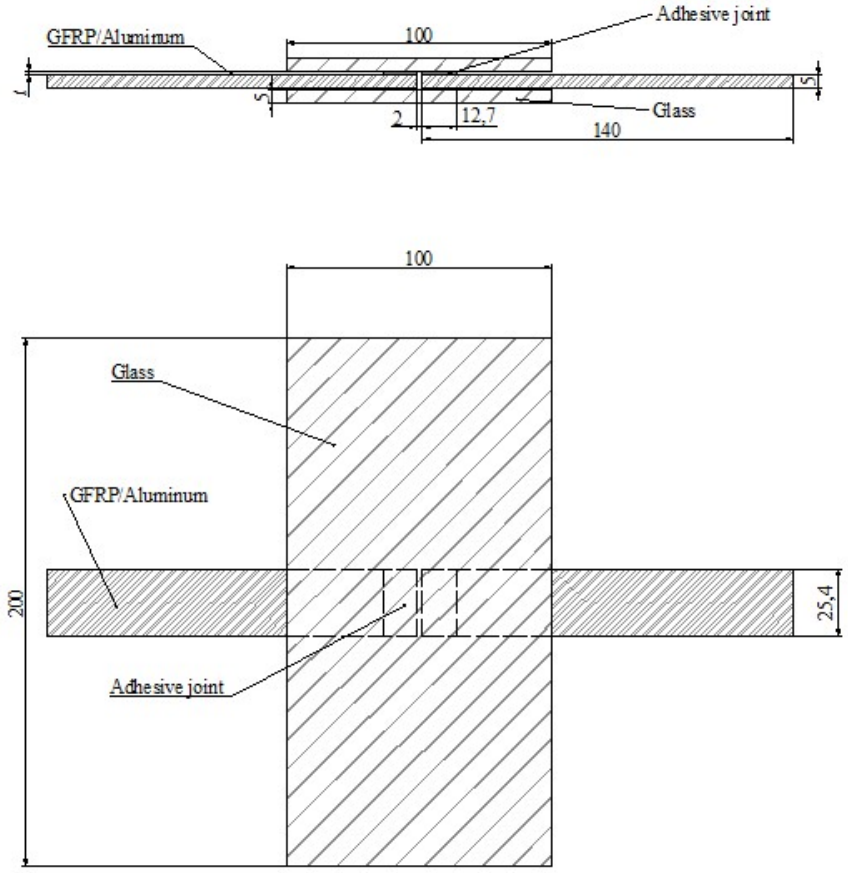

Figure 2.1 Double-lap specimens geometry

For each experiment, three repetitions were conducted, therefore three specimens per type of test and adhesive type where produced.

The dimension of the glass panels was 200 x 100 mm, 5 mm thick, while the dimension of the aluminum and GFRP laminates was 25.4 x 140 mm, 5 mm thick. The total overlap length where the adhesive was applied is 25.4 mm, 12.7 in each

side of the double lap joint. Among the three epoxy adhesives, a different bonding thickness (t) was employed as recommended by the manufacturer, i.e. 0.3 mm for EPX1 and 2 mm for EPX2 and EPX3. With regard to the acrylic adhesives, instead, the bonding thickness depends on the tape thickness, i.e. 1.1 mm for ACR1 and ACR2 and 2.3 mm for ACR3.

Since the study is focused on the shear strength of the joint, in the connections zone, the double-lap specimens are separated by a 2 mm interspace, where the adhesive is not present, in order to avoid the connection between the two adherents. All surfaces were cleansed with isopropyl alcohol, furthermore, as recommended by manufacturers, the glass was treated with a silane primer when acrylic adhesives were used, and a primer stick was applied on GFRP/aluminum laminates.

The specimens were manufactured under laboratory conditions (temperature of 18°C, relative humidity of 70%) and cured at room temperature for 23 days, according to specifications.

2.1.2 Test set up and test program

All tests were carried out according to ASTM D3528-16 (2016), under displacements control, with a crosshead speed of 1,27 mm/min. All specimens were loaded up to the joint fracture, identified as a force drop larger than 80% with respect to the maximum one. Figure 2.2 shows the test configuration.

The load was applied at the same rate of 1.27 mm/min used for the previous test and the specimens were again loaded up to the joint failure.

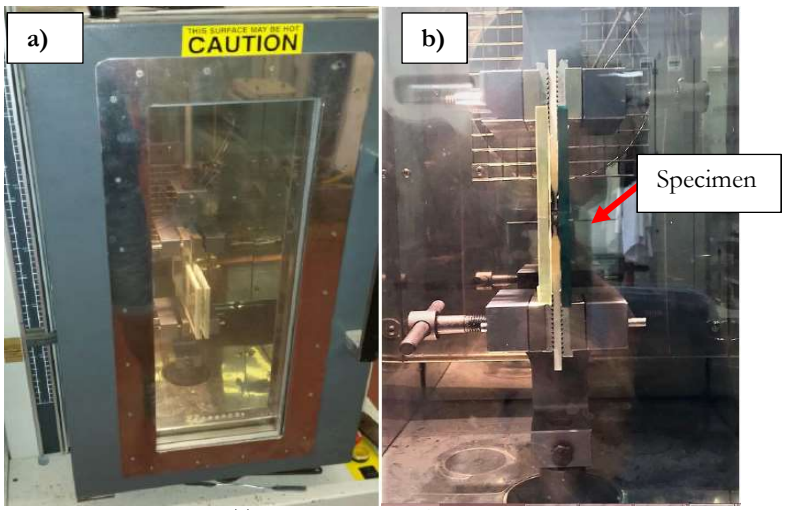

Figure 2.2 a)Testing machine; b) Specimen positioning.

As mentioned before, for each type test three repetitions were performed, thus a series of 18 specimens per adhesive type, subdivided according to the temperature conditions, were tested: three at room temperature (T_0), three at work temperature (T_w, namely 50°C) and three at maximum service temperature (T_m=85°C for *EPX* and 90°C for *ACR*) for each of the two adherents.

The test program is summarized in Table 2.VI.It is worth noting that the *ACR3* was tested only at room temperature. As further specified, this adhesive showed a poor compatibility in the first test and therefore was accordingly excluded from the following analysis.

Table 2.VI Test program

Adhesives	T_0	T_w	T_m
EPX1	3	3	3
EPX2	3	3	3
EPX3	3	3	3
ACR1	3	3	3
ACR2	3	3	3
ACR3	3	-	-

2.1.3 Results and discussion

In this section, the load-elongation response and the failure modes of double-lap joints are presented and analyzed, the results are presented in terms of mean value and standard deviation, computed with respect to the three repetitions. The results are subdivided according to the used temperature conditions (T_0, T_w and T_m).

Mechanical performances of double-lap joints at laboratory conditions

Tensile tests were conducted on the double lap joints under laboratory conditions (registered temperature 20°C and relative humidity 50%). Table 2.VIIand Table 2.VIII summarize the identified mechanical properties of aluminum and GFRP double-lap specimens, in terms of load carrying capacity (kN), maximum elongation (mm) and stiffness (kN/mm).

These parameters are needed for a smart design way in order to allow the maximum workability of the adhesive junction.

Table 2.VII Mechanical properties of the glass-aluminum double-lap specimens

Series	Fmax		Displacement*		k	
	[kN]		[mm]		[kN/mm]	
	Mean Value	Standard Deviation	Mean Value	Standard Deviation	Mean Value	Standard Deviation
EPX1	8.09	2.217	0.14	0.024	74.82	7.244
EPX2	3.93	0.609	0.16	0.041	34.05	3.510
EPX3	3.45	0.775	0.14	0.045	34.05	3.510
ACR1	0.30	0.008	10.41	0.641	0.03	0.364
ACR2	0.30	0.020	7.71	0.274	0.04	1.667
ACR3	0.15	0.021	11.23	1.466	0.01	0.077

Table 2.VIII Mechanical properties of the glass-GFRP double-lap specimens.

Series	Fmax		Displacement*		k	
	[kN]		[mm]		[kN/mm]	
	Mean Value	Standard Deviation	Mean Value	Standard Deviation	Mean Value	Standard Deviation
EPX1	11.72	2.573	0.33	0.068	43.77	3.931
EPX2	5.86	0.964	0.23	0.009	33.66	0.087
EPX3	4.51	0.501	0.20	0.069	29.69	1.972
ACR1	0.34	0.049	12.09	0.476	0.03	0.003
ACR2	0.35	0.021	10.43	1.056	0.03	0.001
ACR3	0.13	0.012	11.37	1.276	0.01	0.000

The overall stiffness of the joints was computed through a linear fit of the force-displacement curve, the fitting was limited to the initial part of the curve, before the damage initiation that produces a non-linear behavior. The corresponding load-displacement curves for the three epoxy and acrylic adhesives, are shown in Figure 2.3 and Figure 2.4.

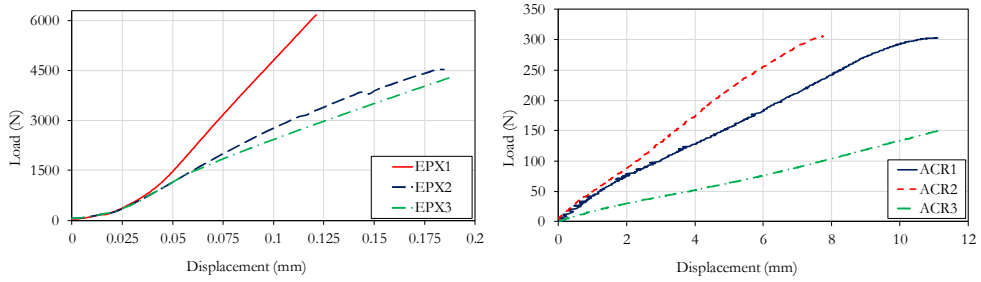

(a) **(b)**

Figure 2.3 Representative load-displacement curves of glass-aluminum double-lap specimens, bonded with three epoxy adhesives (a), and three acrylic adhesives (b).

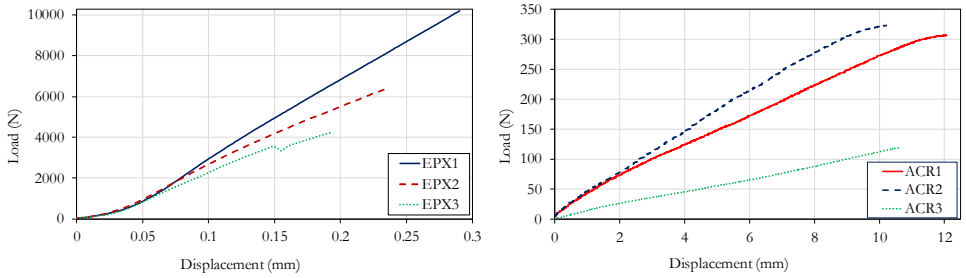

(a) **(b)**

Figure 2.4 Representative load-displacement curves of glass-GFRP double-lap specimens, bonded with three epoxy adhesives (a), and three acrylic adhesives (b).

The mechanical properties are remarkably different between epoxy and acrylic adhesive. In particular, as shown in Table 2.VIIand Table 2.VIII, epoxy adhesives have much higher load carrying capacity and stiffness, while acrylic adhesives present grater joint elongation. *EPX2* and *EPX3* had an almost similar behavior in terms of load-joint elongation r and maximum load, while the best performances were achieved by *EPX1*, which bore the highest load. i.e. 10.51 kN for glass-aluminum and 14.70 kN for glass-GFRP. *ACR1* and *ACR2* showed mainly the same behavior, while *ACR3* resulted in a poor performance with very low maximum load (0.13 kN) and joint stiffness (0,01 kN/mm). For this reason, ACR3 was excluded from the following analysis on high temperatures. Looking at the comparison between epoxy and acrylic adhesives, there is a large difference in terms of stiffness, in particular, the stiffness of epoxy joint is more than 1000 times higher than the corresponding acrylic one. The maximum load is around 10 times higher in epoxy joints while the maximum elongation is 10 times higher in acrylic ones. Therefore, the choice between epoxy or acrylic adhesives depends on the intended purpose of the junctions: if high load carrying capacity is required, epoxy ones should be used, otherwise, if a certain level of deformability is necessary, acrylic ones should be preferred. Furthermore, from the analysis of Figure 2.3 and Figure 2.4, it turns out that epoxy joints are also influenced by the adherent, in particular, glass-GFRP joints have a load carrying capacity around 30-50% higher than the glass-aluminum ones, due to the GFRP higher superficial roughness. This influence is less evident in acrylic joints.

Mechanical performances of double-lap joints at high temperatures

Tensile tests were conducted on the double lap joints at work temperature (T_w = 50°C) and at maximum service temperature (T_m=85°C for *EPX* and 90°C for *ACR*), the results are summarized in Table 2.IX and Table 2.X, the same mechanical properties before investigated are listed. All adhesives presented a

drastic reduction of the load carrying capacity. *EPX1* presented the best behavior by maintaining almost similar stiffness at both temperatures, while the acrylic tapes shown the worst behavior.

The same consideration can be done for both aluminum and GFRP double-lap specimens, meaning that the performance reduction is obviously due only to the adhesive behavior.

Table 2.IX Mechanical properties of the glass-aluminum double-lap specimens at high temperatures.

Series	Test Temperature	Fmax		Displacement*		k	
	[°C]	[kN]		[mm]		[kN/mm]	
		Mean Value	Standard Deviation	Mean Value	Standard Deviation	Mean Value	Standard Deviation
EPX1	T_w	3.01	0.746	0.69	0.085	3.98	0.119
	T_m	1.18	0.057	0.51	0.009	2.53	0.028
EPX2	T_w	2.96	0.463	0.80	0.085	4.09	0.058
	T_m	0.33	0.010	1.29	0.060	0.37	0.032
EPX3	T_w	4.21	0.247	1.28	0.028	3.43	0.022
	T_m	0.49	0.014	1.00	0.065	0.51	0.008
ACR1	T_w	0.10	0.025	16.66	3.006	0.01	0.000
	T_m	0.03	0.004	5.76	0.913	0.01	0.000
ACR2	T_w	0.14	0.007	15.84	1.516	0.01	0.001
	T_m	0.05	0.001	7.60	0.362	0.01	0.000

Table 2.X Mechanical properties of the glass-GFRP double-lap specimens at high temperatures.

Series	Test Temperature	Fmax		Displacement*		k	
	[°C]	[kN]		[mm]		[kN/mm]	
		Mean Value	Standard Deviation	Mean Value	Standard Deviation	Mean Value	Standard Deviation
EPX1	T_w	3.95	0.240	1.64	0.226	3.48	0.370
	T_m	0.94	0.093	0.40	0.039	2.55	0.155
EPX2	T_w	4.95	0.235	2.04	0.255	2.95	0.439
	T_m	0.21	0.030	0.66	0.110	0.26	0.006
EPX3	T_w	6.00	0.951	3.44	0.397	2.55	0.400
	T_m	0.55	0.075	1.12	0.130	0.50	0.004
ACR1	T_w	0.16	0.006	19.89	1.691	0.01	0.000
	T_m	0.03	0.000	5.56	0.244	0.01	0.001
ACR2	T_w	0.13	0.026	17.62	1.198	0.01	0.000
	T_m	0.05	0.002	7.57	0.157	0.01	0.000

The corresponding load-displacement curves for the three epoxy adhesives and for the two acrylic adhesives, are shown in Figure 2.5 and Figure 2.6 where the comparison between the mechanical trends at different temperatures of the tested double-lap joints with aluminum and GFRP supports, respectively, are depicted.

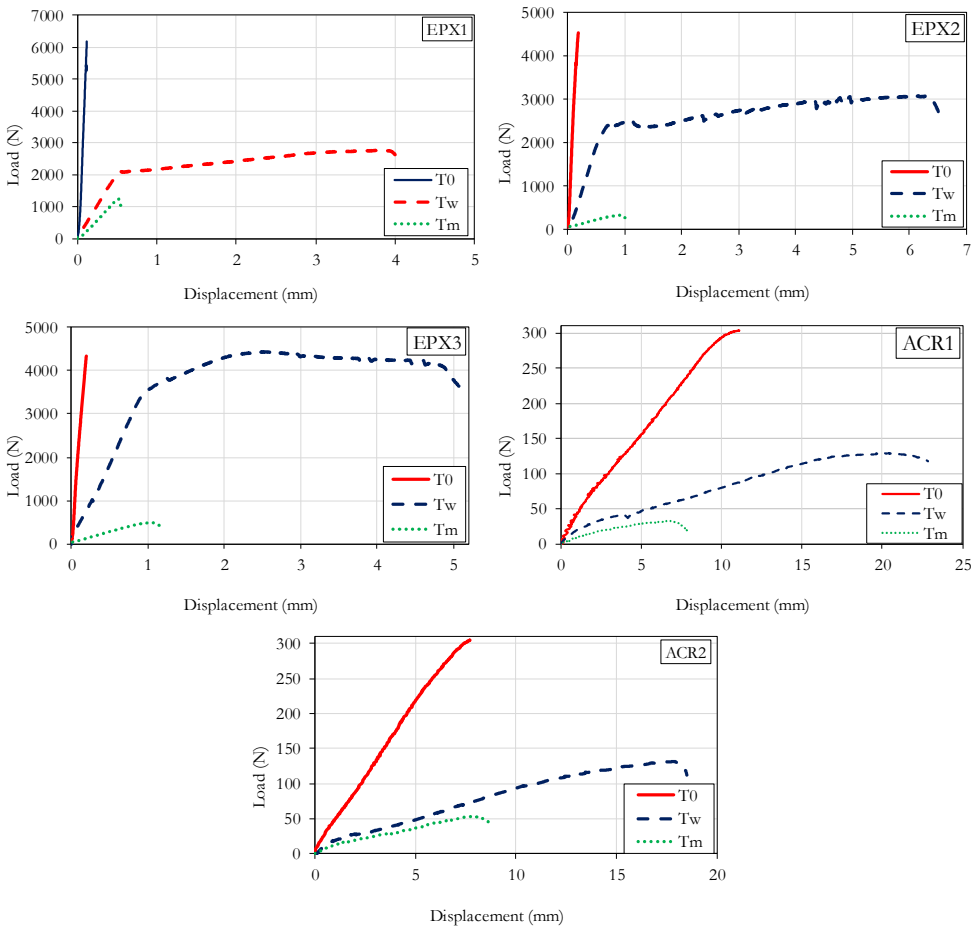

Figure 2.5 Comparison between mechanical trends at different temperatures of glass-aluminum adhesive joints.

It can be evidenced that, for all the adhesives, there is a drastic reduction of the joint stiffness, together with an increment of the joint elongation response. This second plastic branch is correlated to the higher deformability of the adhesive at high test temperature. Figure 2.7 and Figure 2.8 show the percentage reduction of the maximum carried load of the glass-aluminum and glass-GFRP double-lap joints, respectively, with respect to the room temperature performances.

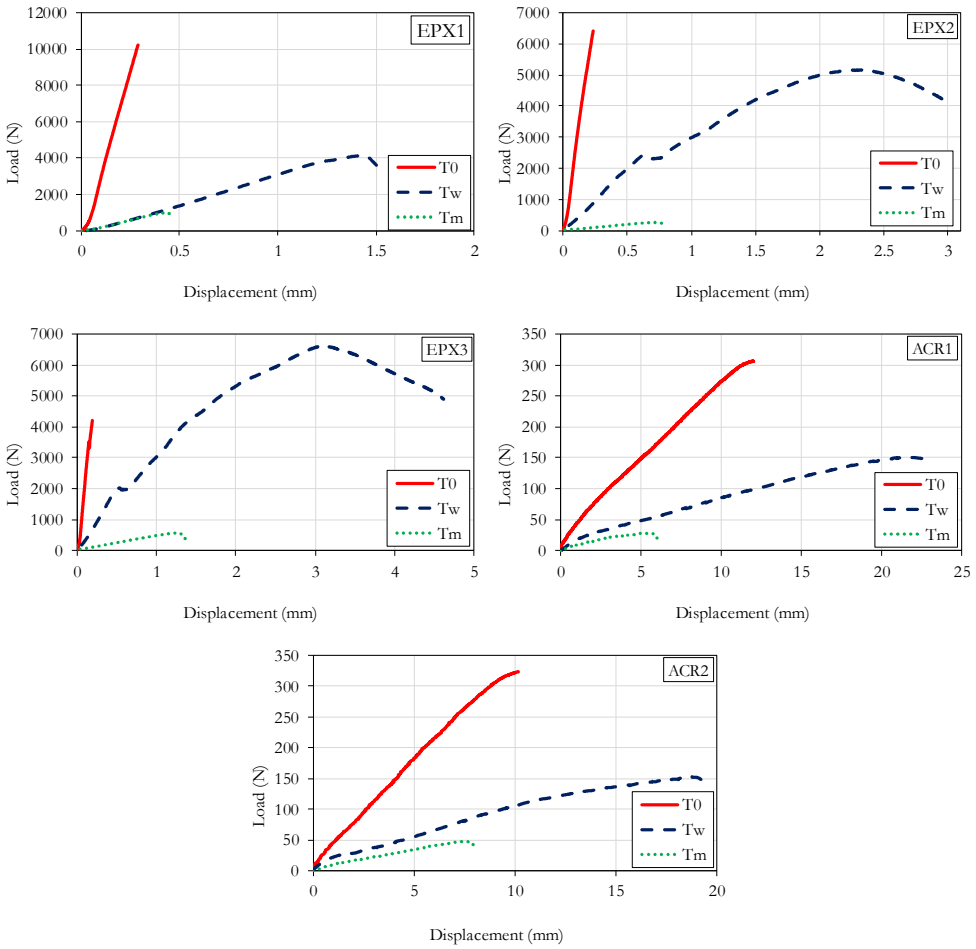

Figure 2.6 Comparison between mechanical trends at different temperatures of glass-GFRP adhesive joints.

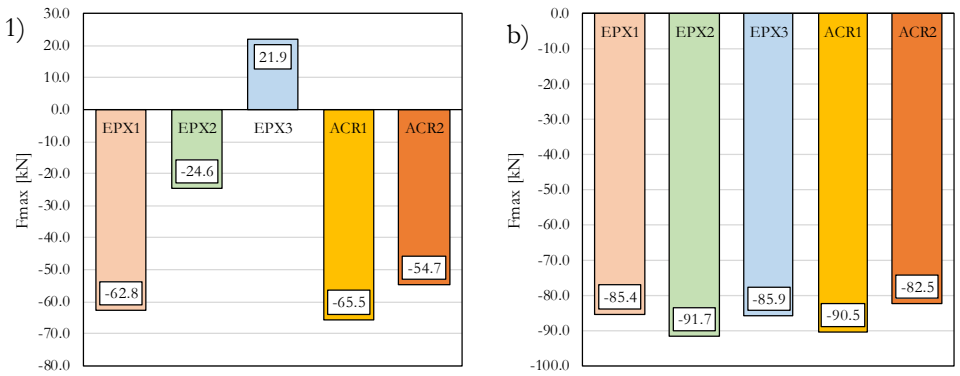

Figure 2.7 Percentage reduction of the maximum carried load of the aluminum/glass double lap joint at high temperatures: a) T_w and b)T_m

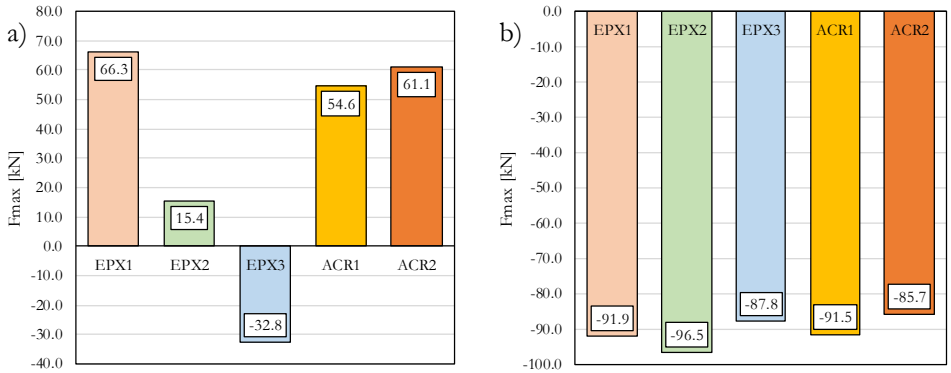

Figure 2.8 Percentage reduction of the maximum carried load of the GFRP/glass double lap joint at high temperatures: a) T_w and b)T_m

EPX2 and *EPX3* shown the best behavior at work temperature, with a contained reduction of the maximum load; in particular, *EPX3* presented even an improvement of the performance, that can be explained through a further adhesive catalyzation with the high temperature. Moreover, this improvement can be associated to a change in the failure mode: the tested samples showed a fragile failure at T_0, while, at T_w, the failure mode changed, exhibiting a plastic deformation, which is, instead, not present at T_m. As a matter off act all adhesives presented a drastic reduction of the load carrying capacity at T_m, that is correctly identified by the manufacturer as the maximum service temperature indeed.

Failure modes

In this section, the failure modes of the tested specimens are described and analyzed. The failure modes are classified according to ASTM D3528-16 (2016); in Figure 2.9- Figure 2.12the four types of failure modes occurred during the tests are depicted:

- The first is an "Adhesive Failure" (AF – Figure 2.9) and occurred at the interface between the adherent and the adhesive.
- The second is a "Cohesive Failure" (CF – Figure 2.10), occurring within the adhesive layer: this reveals a good compatibility between adhesive and adherents.
- In the third picture (Figure 2.11), a "Light-Fiber-Tear Failure" (LFTF) is showed that occurred within the GFRP adherent, with few glass fibers transferred from the adherent to the adhesive.

- In Figure 2.12 there is an example of "Mixed Failure" (MF), which combines two of the failure modes described above (AF and CF, for example).

Figure 2.9 Failure modes of glass-GFRP/aluminum double lap joints: adhesive failure.

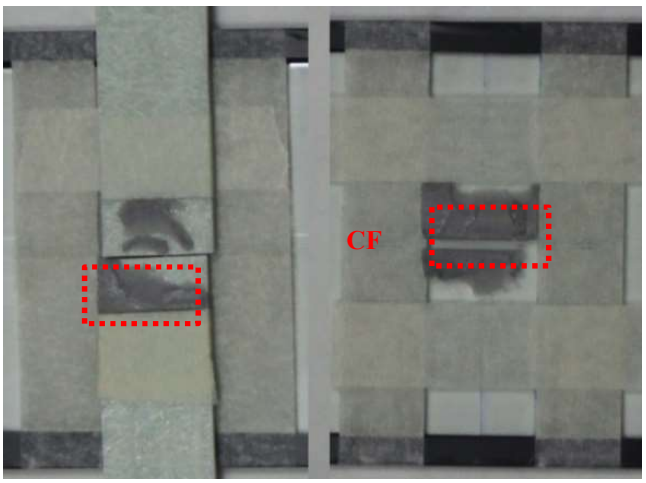

Figure 2.10 Failure modes of glass-GFRP/aluminum double lap joints: cohesive failure.

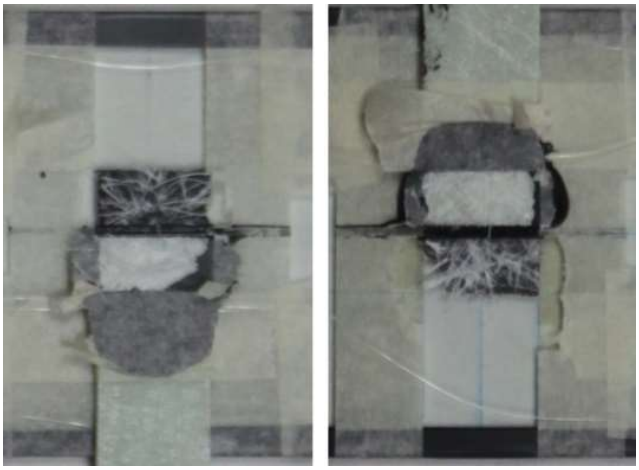

Figure 2.11 Failure modes of glass-GFRP/aluminum double lap joints: light-fiber-tear failure.

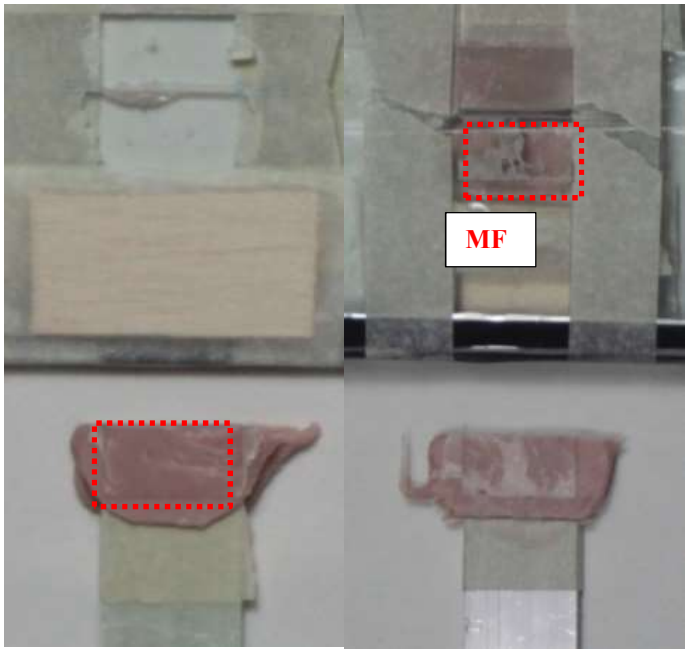

Figure 2.12 Failure modes of glass-GFRP/aluminum double lap joints: mixed failure.

Table 2.XIand Table 2.XIIsummarize the failure modes of glass-aluminum and glass-GFRP joints, respectively.

Glass-Aluminum specimens presented mainly AF, while glass-GFRP showed LFTF or CF, showing a greater compatibility of the bonding system at T_0. For both epoxy and acrylic adhesives, the adherence with the laminates is reduced by the exposition to high temperatures, i.e. the majority of the observed failures became AF.

Table 2.XI Failure modes of aluminum-glass double lap joints

Series	Specimen n°	Failure mode T_0	Failure mode T_w	Failure mode T_m
EPX1	1	AF	AF	AF
	2	AF	AF	AF
	3	AF	AF	AF
EPX2	1	MF: 60% AF / 40% CF	AF	AF
	2	Glass delamination	AF	AF
	3	AF	AF	AF
EPX3	1	AF	AF	AF
	2	AF	AF	AF
	3	AF	AF	AF
ACR1	1	AF	AF	AF
	2	CF	AF	AF
	3	CF	AF	AF
ACR2	1	AF	AF	AF
	2	AF	AF	AF
	3	AF	AF	AF
ACR3	1	-	-	-
	2	-	-	-
	3	-	-	-

Table 2.XII Failure modes of GFRP-glass double lap joints

Series	Specimen n°	Failure mode	Failure mode T_w	Failure mode T_m
EPX1	1	LFTF	MF	AF
	2	LFTF	MF	AF
	3	LFTF	Glass failure	AF
EPX2	1	MF: 95% AF / 5% CF	AF	AF
	2	MF: 95% AF / 5% CF	AF	AF
	3	Glass delamination	AF	AF
EPX3	1	AF	MF	AF
	2	AF	MF	AF
	3	AF	MF	AF
ACR1	1	CF	MF	AF
	2	CF	MF	AF
	3	AF	MF	AF
ACR2	1	CF	MF	MF
	2	CF	MF	LFTF
	3	MF: 60% AF / 40% CF	MF	MF
ACR3	1	-	-	-
	2	-	-	-
	3	-	-	-

2.1.4 Discussion

Tensile tests demonstrated the compatibility of the glass-GFRP and glass-aluminum- bonding system, and the best mechanical performance of the first epoxy adhesive (*EPX1*) was observed, for both adherents. Epoxy joints are influenced by the adherent, in particular the load carrying capacity is higher in GFRP joints with respect to the aluminum ones, due to the GFRP higher superficial roughness; instead, in acrylic joints this influence is less evident.

In an unexpected way EPX3, presented an improvement of the performance at work temperature, which could be explained through a further adhesive catalization with the high temperature. All the adhesives presented a drastic reduction of the load carrying capacity at T_m. Glass-aluminum specimens presented adhesive failure, while glass-GFRP showed LFTF or CF, showing a greater compatibility of the bonding system at T_0. Exposition to high

temperatures deteriorates the adhesion between laminates and adhesive, changing in many cases the failure modes to AF.

In summary both at room temperature and high temperatures the highest load carrying capacity was shown by the epoxy adhesives, while, on the other hand, the highest load elongation was obtained with the acrylic ones. Therefore, if a structural performance is needed, epoxy adhesive are more appropriated hybrid joints with glass-aluminum and glass-GFRP. Furthermore, even if exposition to high temperatures leads to a decay of the joint mechanical performances, which has to be taken into account with an appropriate safety factor in the design phase, the joint elongation for epoxy adhesives is contained within a suitable functionality limit.

2.2 Compatibility and temperature effect on hybrid painted bonded joints made of glass-aluminum

In this second experimental campaign, the mechanical properties of different adhesive joints were investigated. The attention was focused on painted aluminum and cloudy glass. In the field of window frame these materials are much used and it's important to verify the compatibility between them and the adhesive.

Furthermore, in this work the influence of temperature was investigated in order to evaluate the limit of functionality of adhesive joint. Tensile test on double-lap joints were performed and the results will be discussed in the following sections.

Moreover, in this project, the attention was focused on the adhesive DP460 3M^{TM} (EPX4) and for this reason, a mechanical characterization of the selected adhesive was done. Tensile test at three temperatures on bone dog shape specimens were performed in order to evaluate the constitutive law.

2.2.1 Materials and methods

In order to verify the compatibility and the temperature effect of painted glass/transparent glass junctions, tensile tests on adhesively bonded double lap joints were carried on. In this section, the used materials and the experimental conditions are shown. The combinations were:

- Painted glass – glossy aluminum
- Transparent glass – glossy aluminum

Adherends

Different materials were used in this work, supplied by local producers: float transparent glass, float painted glass and glossy aluminum. The mechanical properties of the materials, provided by the manufacturers, are reported in the following Table 2.XIIIand Table 2.XIV:

Table 2.XIII Glass mechanical properties according to manufacturer's data sheet

Glass		
α	E_t	σ_t
[°C^{-1}]	[GPa]	[MPa]
9x10^{-6}	75	40

Table 2.XIV Aluminum mechanical properties according to manufacturer's data sheet

Aluminum profiles				
α	E_t	σ_{yz}	σ_t	ε_t
[°C^{-1}]	[GPa]	[MPa]	[MPa]	[%]
23.2x10^{-6}	69	250	295	8

Adhesives

In the following are summarized the technical, physical and mechanical characteristics (see Table 2.XV and Table 2.XVI) of the selected adhesive reported by manufacturers data sheet. Only available data are reported.

Table 2.XV Typical uncured physical properties

Product		3M™ Scotch-Weld™ Epoxy Adhesive DP460 Off-White	3M™ Scotch-Weld™ Epoxy Adhesive DP460NS
Viscosity (approx.) @ 73°F (23°C)	Base Accelerator	20,000-50,000 cps 8,000-14,000 cps	150,000-275,000 cps 8,000-14,000 cps
Base Resin	Base Accelerator	epoxy amine	epoxy amine
Color	Base Accelerator	white amber	white amber
Net Weight Lbs./Gallon	Base Accelerator	9.3-9.7 8.8-9.2	9.3-9.7 8.8-9.2
Mix Ratio (B:A)	Volume Weight	2:1 2:0.96	2:1 2:0.96
Work life, 73°F (23°C)	20 g mixed 10 g mixed 5 g mixed	60 minutes 75 minutes 90 minutes	60 minutes 60 minutes 60 minutes

Table 2.XVI Typical cured thermal properties

Product	3M™ Scotch-Weld™ Epoxy Adhesive DP460 Off-White	3M™ Scotch-Weld™ Epoxy Adhesive DP460NS
Physical Color	Off-white	Off-white
Shore D Hardness	75-80	78-84
Thermal Coefficient of Thermal Expansion (in./in./°C) Below Tg / Above Tg	59 x 10^{-6} / 159 x 10^{-6}	74.44 x 10^{-6} / 166 x 10^{-6}
Thermal Conductivity (btu - ft./ft.² - hr. - °F) @ 45°C	0.104	0.104
Electrical Dielectric Strength (ASTM D 149)	1100 volts/mil	727 volts/mil
Volume Resistivity (ASTM D 257)	2.4 x 10^{14} ohm-cm	3.25 x 10^{15} ohm-cm

Experiments

The experimental tests consist in tensile test on adhesively bonded double lap joints according to ASTM D3528-96 (2016). All combinations are tested:

- Painted glass – glossy aluminum
- Transparent glass – glossy aluminum.

Such tests allow evaluating the compatibility between glass-aluminum and comparing the mechanical behavior of the double lap joints bonded with an epoxy adhesive, in terms of their load carrying capacity and displacement.

For each experiment at least five repetitions were conducted, therefore five specimens per type of test and adhesive type where produced. The same bonding thickness (t) of 0.3mm was used for two adhesives. Since the study is focused on the shear strength of the joint, in the connections zone, the double-lap specimens are separated by a 2 mm interspace, where the adhesive is not present, in order to avoid the connection between the two adherents.

No surface treatments were applied to the adherents, since the effect of the superficial roughness was not investigated. All surfaces were cleansed with isopropyl alcohol, furthermore, as recommended by manufacturers. The specimens were manufactured under laboratory conditions (temperature of 20°C, relative humidity of 50%).

2.2.2 Test set up and test program

All tests were carried out according to ASTM D3528-96 (2016), under displacements control, with a crosshead speed of 1,27 mm/min. All specimens were loaded up to the joint fracture, identified as a force drop larger than 80% with respect to the maximum one. The load was applied at the same rate of 1.27 mm/min used for the previous test and the specimens were again loaded up to the joint failure. As mentioned before, for each type test five repetitions were performed subdivided according to the temperature conditions; five at room temperature (T_0), five at work temperature (T_w, namely 50°C) and five at maximum service temperature (T_m=80°C) for each of the four adherents. The test program is summarized in the following Table 2.XVII.

Table 2.XVII Test program

Combination DP460 (EPX4)	T_0	T_w	T_m
Painted glass – Glossy aluminum	5	5	5
Transparent glass – Glossy aluminum	5	5	5

2.2.3 Results and discussion

Tensile tests were conducted on the double lap joints under laboratory conditions. Table 2.XVIIIsummarize the identified mechanical properties of painted glass-glossy aluminum and transparent glass-glossy aluminum double-lap specimens at three test temperatures, in terms of load carrying capacity (N) and maximum elongation (mm).

Table 2.XVIII Mechanical properties of the double-lap specimens at three temperatures.

Comb	Test Temperature	Fmax		Displacement*	
	[°C]	[N]		[mm]	
		Mean Value	Standard Deviation	Mean Value	Standard Deviation
PG-GA	T_0	2622.44	494.89	0.571	0.054
	T_w	2928.42	59.02	1.836	0.049
	T_m	748.75	29.91	0.920	0.027
TG-GA	T_0	1723.21	120.89	0.386	0.055
	T_w	2523.39	295.82	1.678	0.135
	T_m	872.31	160.55	1.029	0.072

Table 2.XIX Stiffness of the double-lap specimens at three temperatures.

Comb	Test Temperature	k_1		k_2	
	[°C]	[N/mm]		[N/mm]	
		Mean Value	Standard Deviation	Mean Value	Standard Deviation
PG-GA	T_0	22307.34	3148.65	3932.54	349.91
	T_w	/	/	1519.09	60.54
	T_m	/	/	835.33	36.09
TG-GA	T_0	19237.12	2476.73	3134.31	452.94
	T_w	/	/	1648.70	269.21
	T_m	/	/	909.37	135.39

From the analysis of results is possible see that performance at T_w, for each combination, are better than those at T_0 in terms of maximum load and maximum displacement. At T_0 the junction presents a bilinear behavior with a short first branch. This happen due to a less deformability of the adhesive at environmental temperature, as investigated in the following section though tensile tests on dog-bone specimens.

Moreover, as shown in Figure 2.13, curves at T_w have less deviation and only one branch, elastic up to failure.

The corresponding load-displacement curves for the three temperatures and two combinations are shown in Figure 2.13.

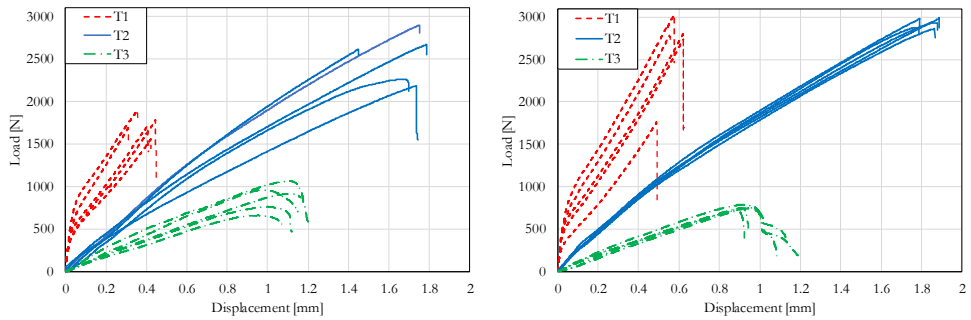

(a) **(b)**

Figure 2.13 Comparison between mechanical trends at different temperatures of two combinations: (a) glossy aluminum-painted glass: (b) glossy aluminum-transparent glass.

2.3 Tensile test on dog-bone specimens

Related to last experimental tests, tensile tests were conducted on adhesive EPX4, in order to have a complete mechanical characterization of the material. Dog-bone specimens were made according to UNI EN ISO 527-1/2 (2012) as shown in Figure 2.14, specimen type 1B (see Table 2.XX).

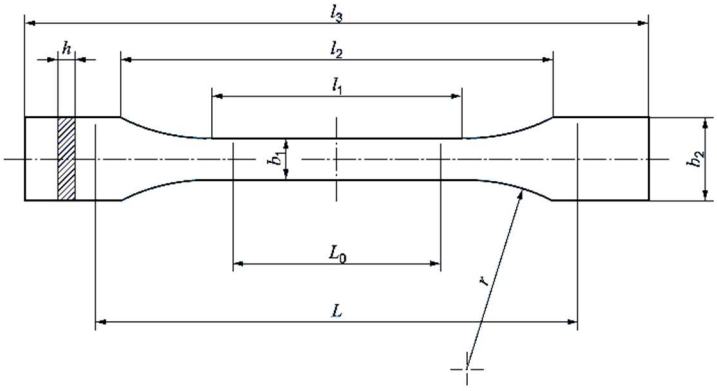

Figure 2.14 Test specimen, adapted from UNI EN ISO 527-2.

Table 2.XX Different test specimens, adapted from UNI EN ISO 527-2.

Dimensions in millimetres

	Specimen type	1A	1B
l_3	Overall length[a]	170	≥150
l_1	Length of narrow parallel-sided portion	80 ± 2	60,0 ± 0,5
r	Radius	24 ± 1	60 ± 0,5
l_2	Distance between broad parallel-sided portions [b]	109,3 ± 3,2	108 ± 1,6
b_2	Width at ends	20,0 ± 0,2	
b_1	Width at narrow portion	10,0 ± 0,2	
h	Preferred thickness	4,0 ± 0,2	
L_0	Gauge length (preferred)	75,0 ± 0,5	50,0 ± 0,5
	Gauge length (acceptable if required for quality control or when specified)	50,0 ± 0,5	
L	Initial distance between grips	115 ± 1	115 ± 1

[a] The recommended overall length of 170 mm of the type 1A is consistent with ISO 294-1 and ISO 10724-1. For some materials, the length of the tabs may need to be extended (e.g. l_3 = 200 mm) to prevent breakage or slippage in the jaws of the testing machine.

[b] $l_2 = l_1 + [4r(b_2 - b_1) - (b_2 - b_1)^2]^{1/2}$, resulting from l_1, r, b_1 and b_2, but within the indicated tolerances.

Also for this experimental campaign the effect of temperature on mechanical behavior of the material was evaluated. In particular, tensile test on dog-bone specimens at three temperatures were carried out. The three temperatures were the same of the previous paragraph, T_0, T_w and T_m. Results in terms of stress-strain curves are following reported in Figure 2.15, Figure 2.16 and Figure 2.17.

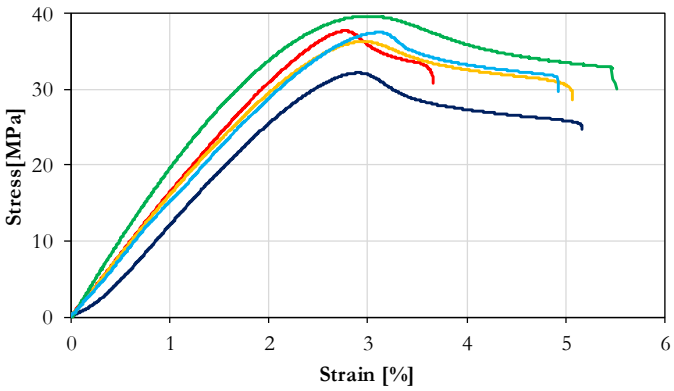

Figure 2.15 Stress strain curve of dog-bone specimens at environmental temperature

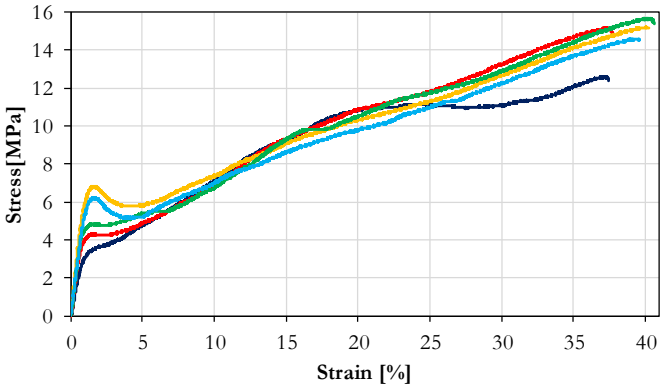

Figure 2.16 Stress strain curve of dog-bone specimens at work temperature (T_w=50 °C)

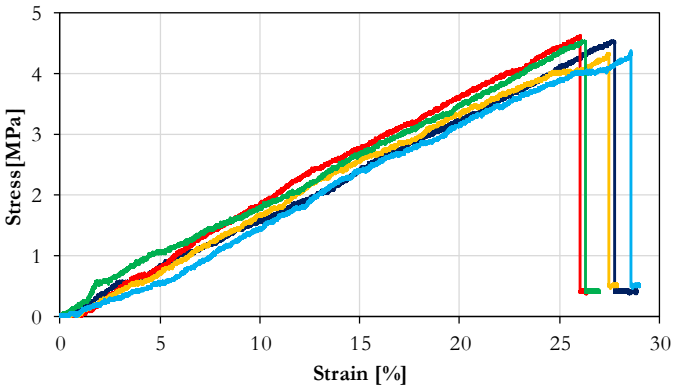

Figure 2.17 Stress strain curve of dog-bone specimens at maximum service temperature (T_m=80°C)

Table 2.XXI Mechanical properties of adhesive EPX4

Test Temperature	σ_{ys}		ε_{ys}		σ_{max}		ε_{max}	
[°C]	[MPa]		[mm/mm]		[MPa]		[mm/mm]	
	Mean Value	Standard Deviation	Mean Value	Standard Deviation	Mean Value	Standard Deviation	Mean Value	Standard Deviation
T_0	36.65	2.78	0.0295	0.0013	36.66	2.78	0.0487	0.0070
T_w	5.15	1.36	0.0159	0.0005	38.85	1.47	0.1464	0.0120
T_m	4.49	0.12	0.27190	0.0108	4.49	0.12	0.27190	0.0108

Table 2.XXII Young Modules of adhesive EPX4

Test Temperature	E_1		E_2	
[°C]	[MPa]		[MPa]	
	Mean Value	Standard Deviation	Mean Value	Standard Deviation
T_0	1382.713	49.69	/	/
T_w	585.004	119.74	30.239	6.880
T_m	17.015	0.564	/	/

In Table 2.XXI and Table 2.XXII are summarized the mechanical properties of EPX4. It's possible doing some consideration from results:

- At T_0 EPX4 shows an elastoplastic softening behaviour, with a Young modulus of 1382.7 [MPa] and last strain of 0.0487 [mm/mm].
- At T_w a drastic reduction of the maximum stress is observed. Moreover, it exhibits an elastoplastic behaviour with a hardening second branch. Maximum strain increased up a value of 0.1464 [mm/mm].
- At T_m another reduction of the peak stress is showed, with an elastic brittle behaviour. Comparison of three characteristic curves, one of each temperature, is displayed in Figure 2.18.

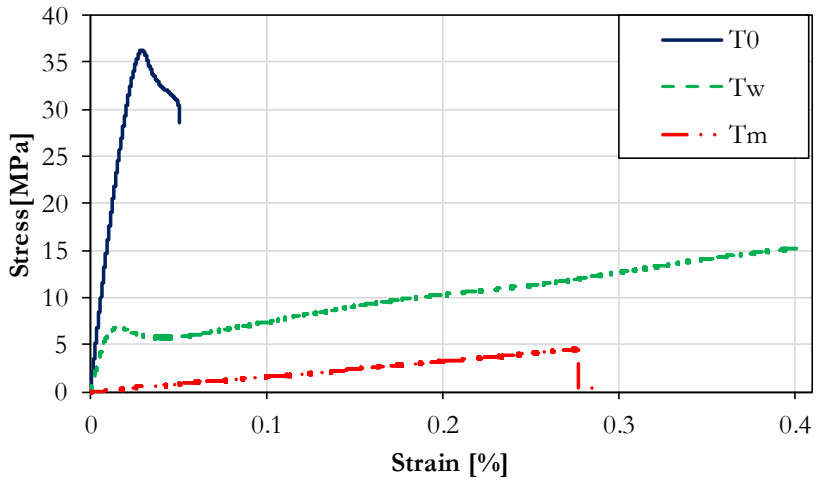

Figure 2.18 Comparison on stress-strain characteristic curve at the three test temperatures

Figure 2.18 shows the comparison between the representative curves at the three test temperatures; from this figure it is possible to notice that at work temperature the selected adhesive shows a higher maximum strain related to a reduced maximum stress if compared to the laboratory condition curve.

The obtained result is fundamental during the design phase of the mechanical component, especially for those elements that are often exposed to high work temperature. For this reason, it is necessary to consider that the adhesive behavior changes drastically at high temperatures and the reliability of the joint depends from that.

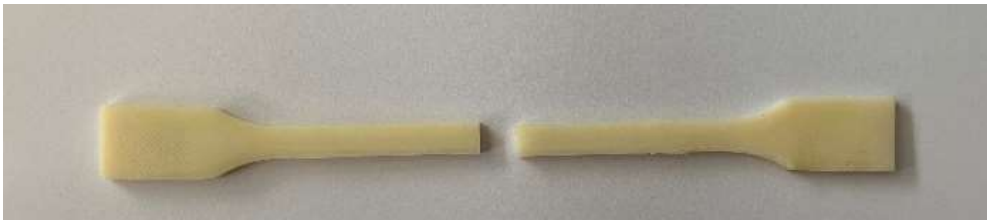

Figure 2.19 Typical failure mode of tensile test on dog-bone specimen

As shown in Figure 2.19 the exhibited dog-bone failure is a classic tensile failure within the gauge length; at high temperatures, within the monitoring length a necking is observed, that is regained when the specimens reaches again the laboratory condition.

Chapter3

FEM Models on adhesive joints

In the field of adhesive joints, for a safety design phase, a right modeling procedure is of key importance. In this Chapter, a numerical model on tensegrity floor is discussed and results are compared with the experimental ones, showing the good agreement.

3.1 Numerical model of the adhesive joint in a Tensegrity floor

This research work is a preliminary study in order to verify the applicability of the adhesive joint in a tensegrity floor system and to quantify the collaboration between the glass pane and the steel sub-frame in terms of stiffness increase.

The innovation of this structure is related to the cooperation of the above mentioned elements; in fact, in those applications where the glass represents the floor decking, the adhesive glass-metal junctions have already been used, but the glass panel has not been considered as a cooperating element.

After the conducted extensive experimental campaign, a numerical model of the proposed system has been developed in order to verify the correspondence between the experimental and the numerical results.

3.1.1 Experimental test

Flexural tests were performed to reproduce the stress of the whole "Tensegrity" floor when it is subjected to the pedestrian live load. In fact, this load condition occurs in the design of the structures belonging to the C2/C3 building category according to the Italian building code (NTC 2008). The geometry of the analyzed system is depicted in Figure 3.1.

The samples were cured for 35 days in laboratory conditions and later were tested through flexural test with cyclic loading as shown in Figure 3.2.

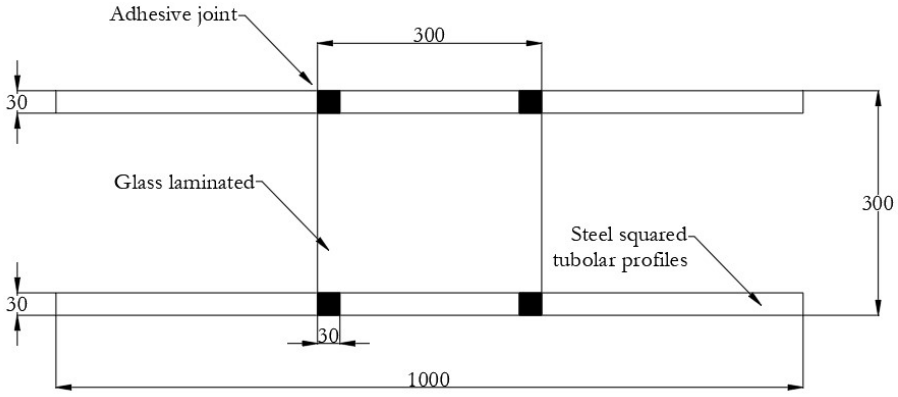

Figure 3.1 Geometric configuration of the hybrid system [mm]

Twenty-one samples were tested: three different adhesives and three for the simply supported system, where the glass panel is not bonded on the steel sub-frame. The sample was composed by two steel squared tubular profiles of AISI 304 (thickness 2 mm) and a laminated glass panel (thickness 4/4mm with PVB interlayer 0.76 mm), connected through a glued joint. The adhesive bonding thickness for all specimens was 3 mm, except for the acrylic tape that was 2.3 mm; in order to avoid, under load application, the contact between the glass panel and the steel elements, which can cause brittle fractures, a soft tape of polychloroprene (3 mm) was interposed between the glass panel and the steel profiles. All surfaces were cleansed with isopropyl alcohol except for the acrylic tape. For the latter two types of primer were used: one for glass and the other for steel profiles.

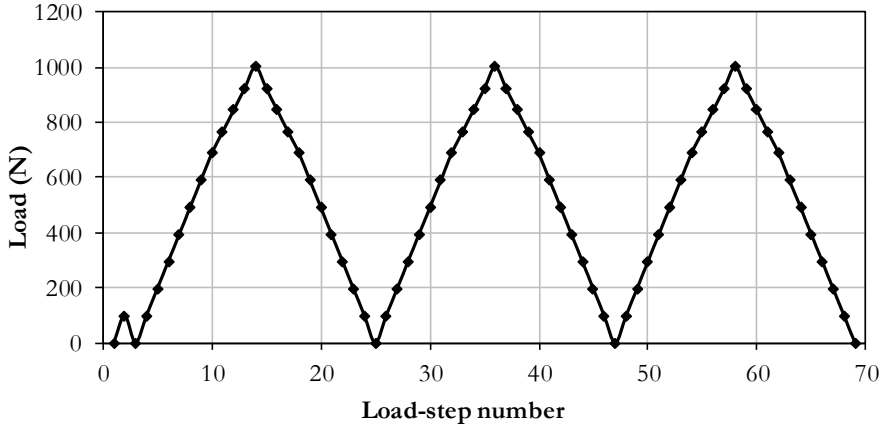

Figure 3.2 Cyclic load for flexural test

Figure 3.3 shows the flexural test set-up: the specimens were positioned on two steel beams, with a span of 800 mm (Figure 3.3a)); Figure 3.3b) shows the corresponding static scheme and Figure 3.3 c) show the transducers position.

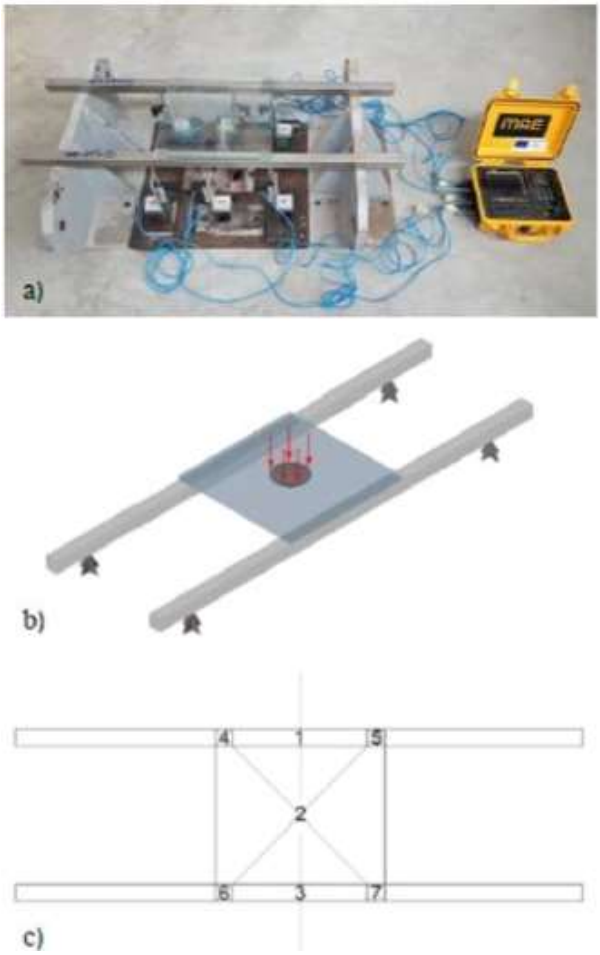

Figure 3.3 Flexural test: a) test set-up; b) static model; c) transducers position

To avoid undesired torsion deformations during the test, suitable clamps were manufactured, registering the displacements due to the loading conditions only (bending). Displacements were registered in seven points using vertical transducers (system for data 24 bit MAE), and located on the intrados (the bottom surfaces) of the profiles. The vertical transducers are analogue potentiometers (model PY2C-50P) supplied by MAE. In Figure 3.3 c) the numeration of the transducers is depicted: points 1 and 3, the medium points of the steel profiles, register the maximum displacements of the profiles; point 2 registers the maximum displacement of the glass sheets; points 4-5-6-7 register the displacements of the glass panels corners, where the glass-steel adhesive joints are

positioned. After the positioning of the sample and the application of the clamps, a metallic pivot was set in the center of the glass sheet.

The sample was subject to a first-step load of 98 N in order to settle the hybrid system; then the test started by incrementally loading the cell plates, that are located on the metallic pivot, as shown in Fig. 14. The experimental test is characterized by three steps of loading and unloading, reaching a maximum load of about 1000 N.

3.1.2 Numerical model

The numerical analysis was performed with the FEM software ABAQUS; in Figure 3.4 the geometry of the modelled system is depicted.

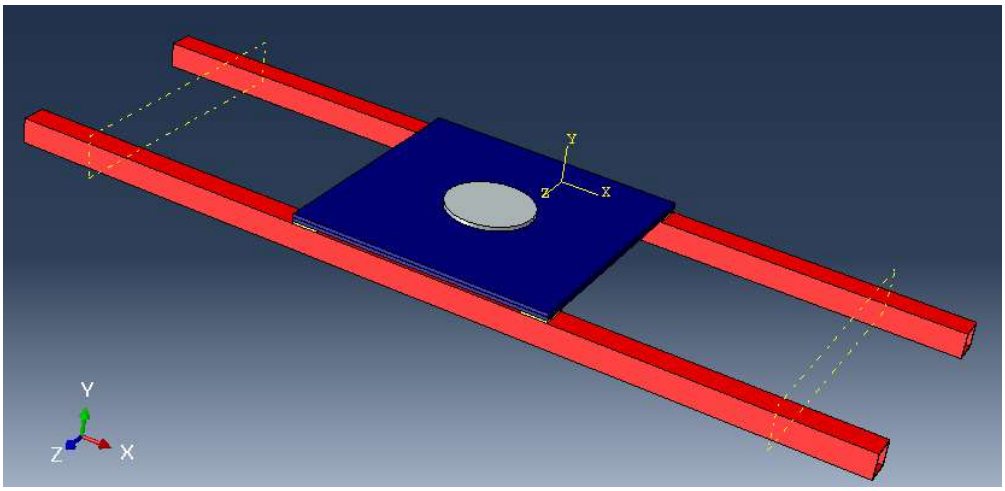

Figure 3.4 FEM model

A circular element, reproducing the basis of the metallic pivot has been introduced in the FEM model, in order to define the load-application area. The steel was modeled as an elastic-plastic material, while the glass was modeled as an elastic material, according to Table 3.I.

Table 3.I Glass and steel properties according to manufacturer's data sheet

Glass panels[a]			Steel profiles[b]			
E_t	σ_t	υ	E_t	σ_{ys}	σ_t	ε_t
[GPa]	[MPa]	/	[GPa]	[MPa]	[MPa]	[%]
70	120	0.22	200	241	586	55

[a]**According to CNR-DT 210/2013, tempered glass**

[b]**According to EN 10025-2:2004**

The glass element was considered as a laminated element, with a PVB layer (0.76mm thickness) interposed between two glass sheets (4mmthickness).

In fact, the mechanical behavior of layered glass is determined by the capacity of the interface material, see PVB, to transfer cutting actions between the plates it joins together. PVB is a material with temperature-depending mechanical characteristics.

The mesh has been modelled applying the finite element "3D STRESS" (TYPE=C3D4); Figure 3.5 pictures the mesh configuration and different size of elements.

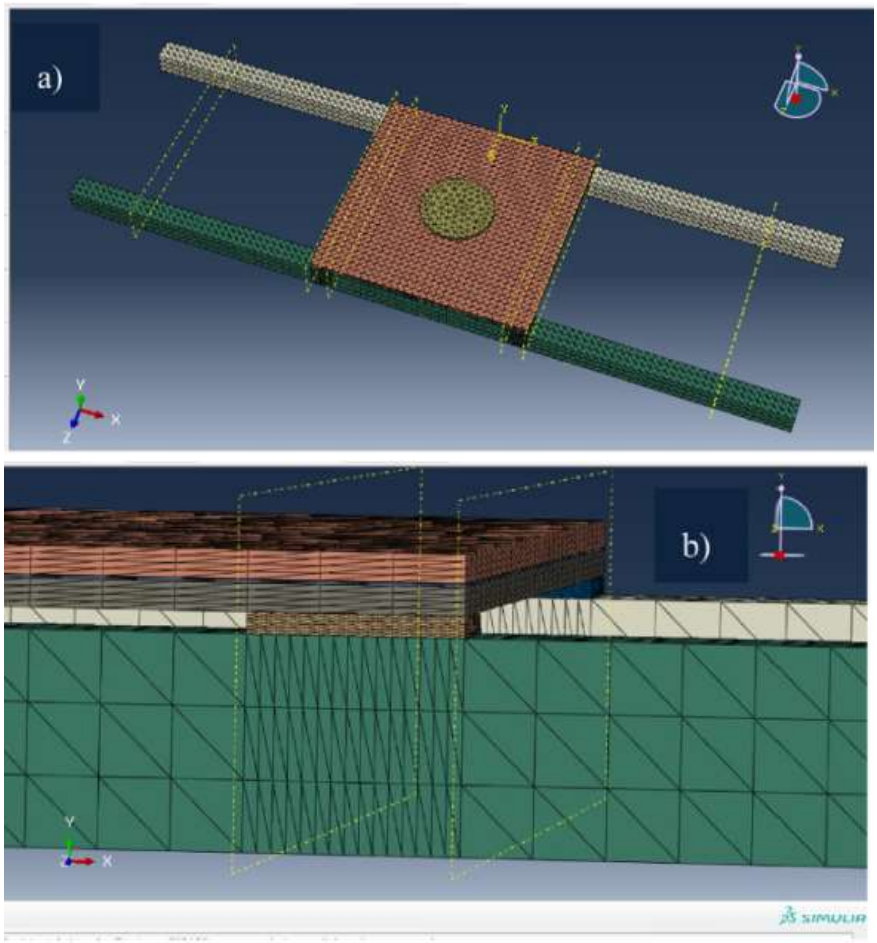

Figure 3.5 Mesh configuration: a) whole system; b) particular of the meshed joint

The selected adhesive is EPX1, as it resulted the best adhesive in term of stiffness increase; the adhesive has been modelled as an elastic material and its mechanical characteristics have been set according to Table 3.II.

Table 3.II Data of mechanical properties in tensile test of the adhesives

Adhesives	E_t		σ_t		ε_t	
	[MPa]		[MPa]		[%]	
	Mean value	Range (±)	Mean value	Range (±)	Mean value	Range (±)
EPX1	2440.0	53.30	32.2	3.20	2.1	0.69

The system has been subjected to the same load history of the experimental tests; the resulting displacements are summarized into Table 3.III, together with the percentage error, evaluated as:

$$\Delta = \frac{d_{experimental} - d_{FEM}}{d_{experimental}} x100$$

Table 3.III Displacement of hybrid samples, experimental and FEM results

Control point	$d^a_{experimental}$	d^a_{FEM}	Δ
	[mm]	[mm]	[%]
Pt. 2	1.990	1.936	2.71
Pt. 1-3	0.795	0.802	-0.88
Pt. 4-5-6-7	0.728	0.696	4.39

[a] **Corresponding to the maximum carried value equal to 1000.2 N.**

From the analysis of this table we observe a percentage error contained within 5%, so the FEM model proves the experimental results. Figure 3.6 depicts the displacement maps. Figure 3.7 depicts the stress map where the compression of the joint is evident, as proposed in the analysis of the experimental results.

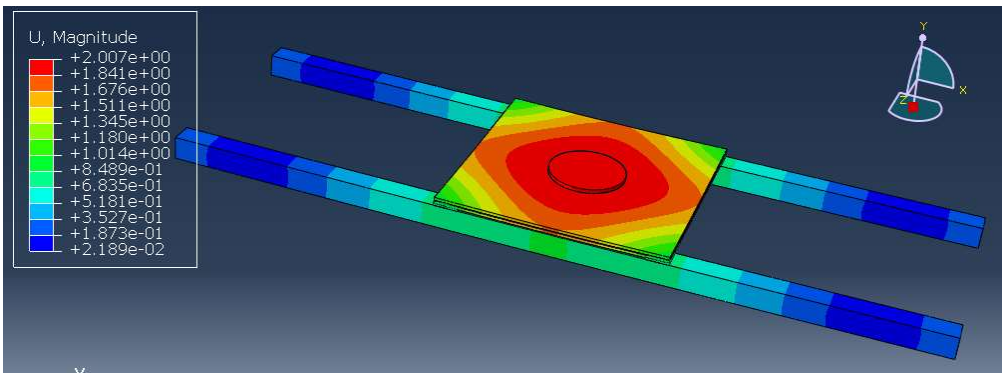

Figure 3.6 Displacement color map

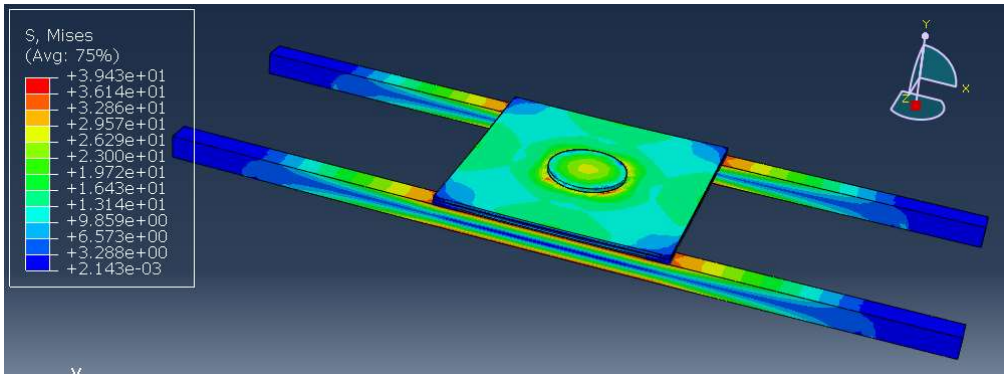

Figure 3.7 Stress map of whole system

Obviously, due to the flexural behavior of the tested system, shear stress could be present, proportional to the applied load; despite this, the stiffness increase is mainly due to the compression properties of the adhesive. In fact, thanks to the stress transmission allowed by the joint (compression), the glass panel is completely under compression due to the applied load, and this fact permits the cooperation between glass and steel. Furthermore, these results justify the use of a 3-D model, which is the only way to correctly interpret the Tensegrity floor system.

Chapter4

Strengthening systems with composite materials

In the last two decades the problems of repair and rehabilitation of civil structures found solution using composite materials and, for this reason, it became an ongoing research topic. In this section, an overview of different composite systems and their connected applicability and design problems is discussed.

4.1 Strengthening systems with externally bonded composite materials

A composite system consists of two or more materials that possess different properties, but when combined they form a new material which exhibits better properties than its individual components. The simplest composite material is usually represented only by two parts: matrix and reinforcing fiber.

The aim is always to find a good solution for rehabilitation in order to guarantee safety and sustainability of civil structures. During the life of a structure, there may come a time when repair or demolition is required. The latter of which is typically the least attractive option due to cost and inconvenience. The first developed strengthening system was the Fiber Reinforced Polymer (FRP), in which fiber of high mechanical performances is embedded into an epoxy resin matrix. The great success of FRP composites is driven by their high strength-to-weight ratio (lightweight), high tensile strength, and non-corrosive properties.

The use of FRP in the repair industry has had an increasing momentum due to the many studies that have been conducted and reported, in order to better understand the properties of FRP systems, their optimal uses, their fundamental advantages but also, their critical issues (the applicability of the system is one of the most discussed topic). In Figure 4.1 an example of FRP strengthening application in a Reinforced Concrete (RC) beam is shown.

Figure 4.1 Example of FRP strengthening applied on a concrete substrate

Despite all of these advantages, FRP has some limitations:

- UV degradation;
- lack of vapor permeability;
- inability to bond to a wet surface;
- fire problem;
- poor behavior at increased temperatures;
- its application needs skilled worker;
- low chemical compatibility with substrates.

While the use of FRP is more established, a recently emerged Fabric Reinforced Cementitious Matrix (FRCM) system is gaining the "spotlight" in the field of composites for structural application. In fact, the principal advantage of this new composite system is the easy of application, but also the durability (discussed in the following sections).

FRCM recognizes the shortcomings of FRP and compensates for these drawbacks with its inherent heat resistance and excellent compatibility with the concrete and masonry substrates.

Recently, many companies are focusing their attention on this new straightening system, trying to find the best solution between matrix and fabric. Different natures of fabric are commonly used in these last applications, like polybenzoxole (PBO), carbon, glass, aramid and etc.

4.2 Fabric Reinforced Cementitious Matrix

FRCM consists of an inorganic cement-based matrix reinforced with a continuous arrangement of one or more layers of dry fibers, commonly known as fabric.

The innovation of this new strengthening system is on combination of novel (fabric) and traditional (cementitious matrix) materials. An example of FRCM application on a concrete beam is shown in Figure 4.2, in which a first layer of mortar is applied to the concrete substrate; then fabric is embedded and a second layer of mortar is applied. The good chemical compatibility between substrate and composite system guarantees the perfectly connection, the maximum mechanical efficiency and the stress transfer.

FRCM systems exhibit favorable tensile behavior, bond properties, and durability performance, which are essential for the success of a repair system in order to increase its performance.

Technical literature reports significant improvement in the flexural, shear, and axial behavior of RC and masonry components strengthened with FRCM. There is no doubt that FRCM systems have proven excellent mechanical and structural performance.

There are many types of fibers (from low to high elastic modulus), fabric weights (low to high equivalent thickness) and fabric materials (glass, carbon, basalt and PBO) used in this system and many experimental published results confirm the efficiency of FRCM system showing excellent performance in terms of increasing flexural and shear strength of RC beams. Moreover, another key aspect is the increasing of displacement close to failure of strengthened elements, which means an increasing of their ductility. The latter is important in seismic areas in which the ductility of structures is a primary parameter for a safety design.

Figure 4.2 Example of FRCM application

4.2.1 Design of FRCM strengthening

Nowadays FRCM system is used by designers of all over the world to increase the strengthening of structural elements (beams, columns and walls) for RC and masonry constructions. American Concrete Institute 549 (ACI549.4R-13 2013) is the first code written in order to provide design rules. Moreover, ICC-ES document Acceptance Criteria 434(AC434 2013) is the acceptance criteria for the FRCM materials issued to provide interested parties with guidelines for demonstrating compliance with model building the codes. Particularly, Annex A of AC434 summarizes the test method to characterize the mechanical properties of FRCM. Test setup for mechanical characterization is shown in Figure 4.3.

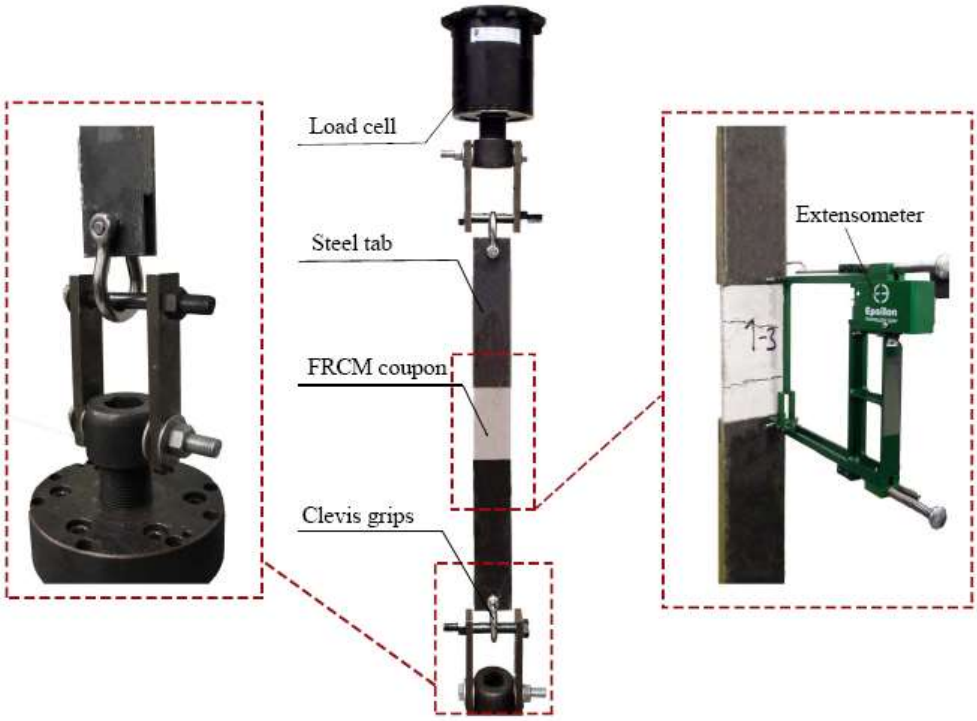

Figure 4.3 Direct tensile test setup per AC434

Most recent document CNR-DT 215 (2018) is the first Italian design code for FRCM.

4.3 Research on strengthening systems with composite material: temperature and moisture influence

Rehabilitation and strengthening of existing structures with composite materials is an ongoing research topic in the field of civil engineering. During the last fifteen years, FRP composites have been widely studied and used in this field. More recently, other laminated composite material systems were developed which use an inorganic (cement- or lime-based) matrix instead of the polymeric matrix of the FRP. These inorganic composites are known as FRCM. Depending on the application, FRCM materials can be an effective alternative to the FRP, because of their excellent performances under elevated temperatures, good chemical and aesthetical compatibility with the concrete and masonry substrates, and applicability in presence of surface moisture or on uneven substrates.

Therefore, in the field of rehabilitation of existing structures with composite materials, the durability of these materials is an interesting research topic. In fact, as shown in Figure 4.4, the Young modulus E of an epoxy resin is strongly

dependent by temperature and, for this reason, also its performances are affected by temperature variation.

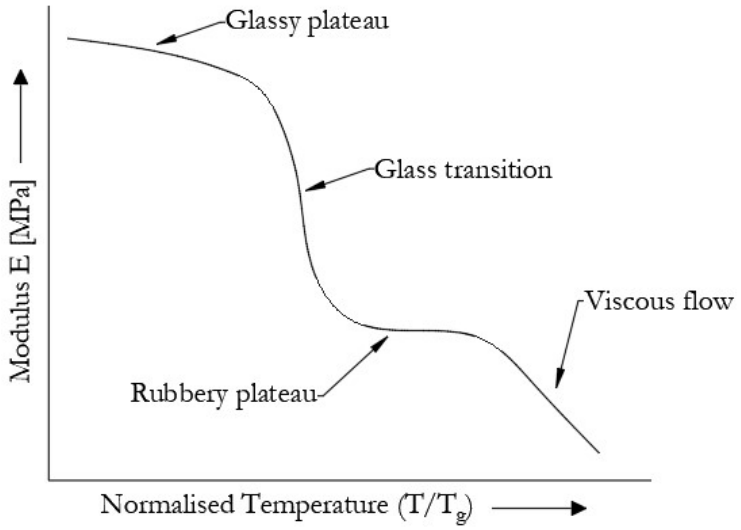

Figure 4.4 Variation of Modulus E with Temperature

The influence of environmental conditions on the bond behavior of strengthening composite systems applied to concrete substrates has been investigated by an experimental campaign, discussed in the following Chapter 5. Two different systems are analyzed, namely FRP system with carbon sheet and epoxy resin (CFRP), and FRCM system with PBO grid and cement-based mortar. The experimental campaign comprises three-point bending tests performed on 24 notched beams with the strengthening system being applied onto the bottom face of the beam in order to selectively study the bond behavior with no tensile contribution of concrete. In addition to classical curing process in air at environmental conditions, two different curing procedures are studied, namely partial immersion in water at 30°C and 50°C and 100% relative humidity for a period of 31 days.

Results in terms of load-displacement curves of the two systems are compared to each other so as to highlight the influence of the environmental conditioning on the bond behavior in the two strengthening systems. For the relatively short duration of the partial immersion process considered in this experimental campaign, the FRCM system is not sensitive to environmental conditioning, whereas the FRP system is only sensitive to curing temperatures close to the glass transition temperature of the resin/primer. An indirect method to evaluate the stress-global slip curve is elaborated in this study through an

analytical procedure, which allows a comparison with results from alternative single-lap shear tests proposed in the literature.

4.4 Numerical models on FRCM strengthening system

For a detailed strengthening design with FRCM composites, the mechanical properties of the materials are required and evaluated through experimental tests. In the United States AC434 includes the test methods to evaluate the mechanical properties of the FRCM through a direct tensile test, which uses clevis grips (see Figure 4.3).

The use of FEM codes to reproduce the behavior of composite materials is an innovative way for their study. In fact, many authors (Liu et al. 2013, 2014 and 2015) have developed new codes that allow the study of crack formation and its propagation.

In the following Chapter 6, two dimensional (2D) and three dimensional(3D) (Figure 4.5) FE models able to catch constitutive behavior of FRCM under tensile stress are described and presented. These tools can be used both in order to verify the bearing capacity of beam with an applied strengthening system and also in order to optimize their mechanical performances by doing parametric studies. Results of numerical studies are presented in the following Chapter 6.

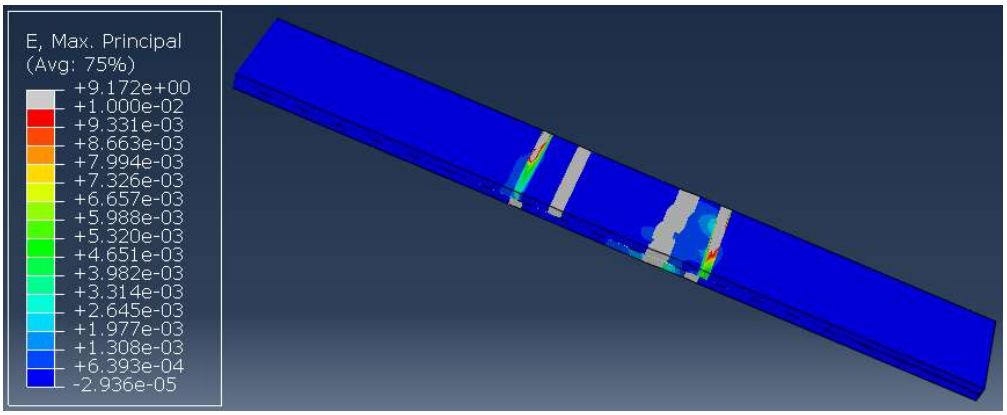

Figure 4.5 3D numerical model for direct tensile test according to AC434

Chapter5

Experimental tests on FRCM/FRP strengthening systems

In this Chapter, the durability problem of FRP an FRCM systems is investigated. The influence of environmental conditions, high temperatures and moisture, on the bond behavior of the above mentioned systems is deeply studied.

Results, in terms of load-displacement curves, are analyzed through analytical approaches and compared each other.

5.1 Introduction

Use of composite materials for rehabilitation and strengthening of concrete structures represents an effective strategy to keep them in service conditions. To this aim, fiber-reinforced polymer (FRP) systems have been widely employed due to their advantageous characteristics, such as excellent mechanical properties, low self-weight, good fatigue characteristics, flexibility and availability in different shapes (ACI 440.2R-08 2008). A well-established strengthening technique consists in externally bonding FRP sheets or strips to the concrete member in order to increase the flexural and/or shear capacity (DT 200 R1 2013, Al-Rousan et al. 2012, De Domenico et al. 2014 and Dong et al. 2013).

Despite the popularity of FRP systems, alternative solutions have emerged in the past decade that makes use of inorganic (cement-based) matrix rather than organic matrix to overcome some of the limitations of FRP systems, including:

1. debonding phenomena of FRP from concrete substrate (Mazzotti et al. 2008 and 2009), which may become more evident for high temperatures approaching the glass transition temperature of the epoxy resin;
2. poor compatibility of epoxy resin with the concrete substrate;
3. change of the bond behavior between FRP and concrete substrate in harsh environmental conditions (temperature and relative humidity).

Indeed, it has been found that protracted moisture conditions produce plasticization of the epoxy-based adhesive of FRP systems (Ghiassi et al. 2013 and Sciolti et al. 2010). This implies that the failure mode of FRP-strengthened concrete elements is strongly affected by environmental conditions. Previous experimental studies are available in the literature that demonstrate the influence of environmental conditions on the bond behavior of FRP-concrete interface(Di Tommaso et al. 2001, Ceroni et al. 2017, Ghiassi et al. 2014 and Toutanji & Gomez 1997).Different terminologies are adopted in the literature to indicate the alternative inorganic-matrix-based composite systems, such as textile reinforced mortar (TRM)(RILEM 2018) or fiber-reinforced cementitious matrix (FRCM) (ACI549.4R 2013).

Recent studies have demonstrated the effectiveness of FRCM systems for different applications, including flexural strengthening(Bencardino et al. 2018, Ebead et al. 2016, Raoof & Bournas 2017a and 2017b), shear strengthening(Gonzalez-Libreros et al 2017a and 2017b, Marcinczak et al. 2019, Loreto et al. 2015, Tetta & Bournas 2016, Triantafillou & Papanicolaou 2006 and Trapko et al. 2015)and confinement action on axially loaded concrete columns(Fossetti et al. 2017, Colajanni et al. 2014a and 2014b and Ombres 2014). These systems comprise a layer of cement-based mortar (that is usually reinforced with short polymer fibers to improve tensile strength) and an embedded grid of fibers having different nature, such as glass, aramid, basalt, carbon, steel or polybenzoxole (PBO) (D'Antino & Papanicolaou 2017). FRCM systems have the following advantages over FRP systems (Mazzotti et al. 2015):

1. larger effective bonded area of the grid, which diminishes the stress concentration that is, in turn, primarily responsible for debonding phenomena;
2. easier application without a careful surface preparation, which is instead required in the FRP system;
3. better compatibility with the underlying concrete (and also masonry (Papanicolaou et al 2007 and 2008)) substrate. The effectiveness of these systems is largely dependent upon the bond behavior between FRCM and concrete substrate, which constitutes a topic that has attracted the attention of many researchers in the past few years with analytical, numerical and experimental investigations(Raoof & Bournas 2017a, Raoof et al. 2016 and 2017c, Carloni et al. 2014, Carloni et al. 2017b, Colombi & D'Antino 2019, D'Ambrisi et al. 2013, D'Antino et al. 2014, 2015a, 2015b and 2016, Focacci et al. 2017, Ombres 2012, Sneed et al. 2014 and 2015).

Along this research line, this study aims to investigate the influence of environmental conditions on the bond behavior of both FRP and FRCM systems applied to concrete substrates. Unlike other studies from the relevant literature that addressed this problem via single-lap or double-lap shear tests, the experimental campaign of this study is based on the ASTM D7958/D7958M (2017) regulations. The test setup consists in three-point bending tests on notched beam specimens with adhesively bonded strengthening systems on the bottom surface across the notch. Strictly speaking, the above standards were conceived for evaluating the performance of FRP composite systems adhesively bonded to concrete substrates, see e.g. (McIsaac et al. 2019), but in this work the same procedure is also applied to FRCM systems for comparative purposes. Using this test setup allows evaluating the bond performance through an application of the load on the strengthened structural element, thus only indirectly transferred to the strengthening system. This test setup seems to be more similar to the real situations compared to the single-lap shear tests in which the system is directly loaded.

The influence of the environmental conditioning on the bond behavior of FRP and FRCM systems is investigated through different curing procedures. More specifically, some specimens were partly immerged (limited to the bottom part surrounding the composite-to-concrete interface) in water at controlled temperature of 30°C and 50°C and relative humidity (RH) of 100% for 31 days, while some other specimens were cured in air at laboratory environmental conditions (23°C and RH = 65–75 %).

The results in terms of force-displacement curves are critically analyzed to highlight the different behaviors between the two composite systems.

Finally, an indirect method to evaluate the stress-slip curve is elaborated through an analytical procedure, which would potentially allow a comparison with results from alternative single-lap shear tests that are more widely used in the literature.

The objectives of this experimental work are:

1) To verify the simultaneous effect of temperature and moisture protracted for a relatively short period (31 days) on the bond behavior of PBO-FRCM and CFRP systems applied to concrete substrates.
2) To use a notched beam test setup to investigate the bond behavior of the two strengthening systems. This test setup involves the application of the load on the strengthened structural element, thus

only indirectly transferred to the strengthening system. This is more similar to the loading configuration that is encountered in practical cases in comparison with the more widely used single-lap shear test where, instead, the load is directly applied to the strengthening system.

Besides the presentation and the discussion of the experimental results, the novel contribution of this work is to elaborate an indirect method for the PBO-FRCM system to obtain the stress-global slip curve based on the results of the adopted notched beam tests.

This curve is representative of the bond performance of FRCM system and could be used for comparison against alternative single-lap shear tests.

5.2 Experimental campaign

The goal of this study is to investigate the bond behavior of FRP and FRCM systems applied to concrete substrates under different environmental conditions. Notched beams were prepared and tested in three-point bending under displacement-controlled mode in accordance with ASTM D7958/D7958M (2017) regulations.

5.2.1 Materials

The beams were prepared using an ordinary Portland cement. Standard cubes of 150 mm side were tested at 28 days to determine the compressive strength of concrete in accordance with EN 12390-3 (2009) standards.

The results are listed in Table 5.I. The tensile strength of concrete was measured through three-point bending tests performed on prismatic beam specimens according to UNI EN 12390-5 (2002) standards. The relevant results are reported in Table 5.II.

The two strengthening systems are PBO-FRCM and CFRP. A representative portion of the carbon sheet and of the PBO grid used in the present experimental campaign are shown in Figure 5.1.

The properties of the mortar used for the FRCM system along with the characteristics of the PBO grid system are listed in Table 5.IIIandTable 5.IV, respectively. With regard to the CFRP system, a two-part primer and a two-part epoxy resin were used, whose main mechanical and physical characteristics are summarized in Table 5.V. Carbon woven fabric was used and the mechanical properties of the final CFRP system are reported in Table 5.VI.

Table 5.I Concrete compressive strength

sample n.	R_c †	f_c ‡
	[MPa]	[MPa]
1	49.5	41.1
2	49.9	41.4
3	40.3	33.4
4	43.6	36.2
5	50.7	42.1
6	49.4	41.0
mean	**47.2**	**39.2**
standard deviation	**4.2**	**3.5**
CoV (%)	**9.0**	**9.0**

†cubic compressive strength (value measured); ‡ cylinder compressive strength (value calculated) according to EN 12390-3 (2009) standards

Table 5.II Concrete flexural strength

sample n.	f_{cf} †	f_{ct} ‡
	[MPa]	[MPa]
1	5.99	4.99
2	5.94	4.95
3	6.16	5.13
mean	**6.03**	**5.02**
standard deviation	**0.12**	**0.10**
CoV (%)	**1.92**	**1.92**

† flexural tensile strength (value measured); ‡ axial tensile strength (value calculated) as per Italian regulations NTC2018

Table 5.III Mechanical properties of mortar used in the PBO-FRCM system

Parameter (unit)	value†
Compressive strength at 28 days (MPa)	≥ 40
Flexural strength at 28 days (MPa)	≥ 4
Young modulus (GPa)	≥ 7

† reported in the manufacturer datasheets

Table 5.IV Mechanical and geometrical properties of the PBO-FRCM grid system

Parameter (unit)	value†
Equivalent thickness of fibers (mm)	0.056
Fabric width (mm)	70
Ultimate load (kN/m)	332
Young modulus (GPa)	270
Tensile strength (MPa)	5.8
Ultimate strain (%)	2.5
Fiber density (g/cm^3)	1.56

† reported in the manufacturer datasheets

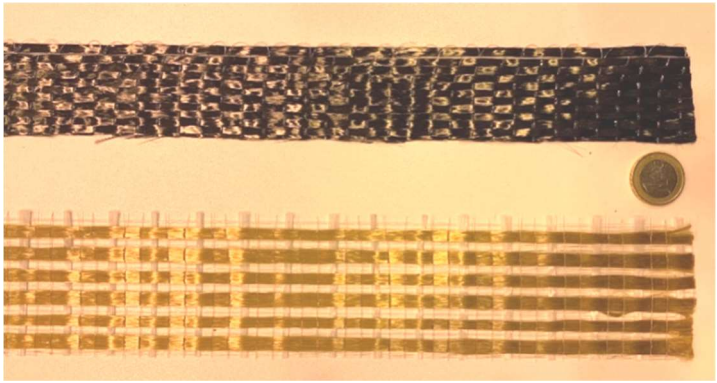

Figure 5.1 Representative carbon sheet and PBO grid used in the experimental campaign

Table 5.V Mechanical properties of primer and epoxy used in the CFRP system

Parameter (unit)	Primer†	Epoxy resin†
Catalysis ratio (A:B)	2:1	2:1
Compressive strength (MPa) (ASTM D695)	≥ 60	≥ 60
Bond strength (MPa) (EN 12188)	≥ 14	≥ 14
Glass transition temperature T_g [°C] (DSC ISO 11357-2)	+ 58	+ 67

† reported in the manufacturer datasheets

Table 5.VI Mechanical properties of CFRP system

Parameter (unit)	value†
Equivalent thickness (mm)	0.167
Tensile strength (MPa)	3468.950
Young modulus (GPa)	244.940

† reported in the manufacturer datasheets

5.2.2 Specimens preparation

The prismatic beam specimens were demolded after 24 hours from casting and then left in a controlled environment at temperature 23°C and RH 100% for 28 days as shown in figure. A wet cover was used to prevent evaporation of water during such first curing phase.

Figure 5.2 Curing process of the specimens: a) after demolding; b) wrapping of specimens to prevent evaporation of water during the 28 days curing time

After 28 days, a notch of 2mm width at the mid-span of the beam was realized with a band saw. The notch height and the other dimensions were realized in accordance with ASTM D7958/D7958M (2017) regulations. The main dimensions of the specimen and of the notch are reported in the sketch of Figure 5.3. Subsequently, the bottom surface of the concrete beam was polished and sandblasted before the application of the strengthening composite system, as illustrated in Figure 5.4.

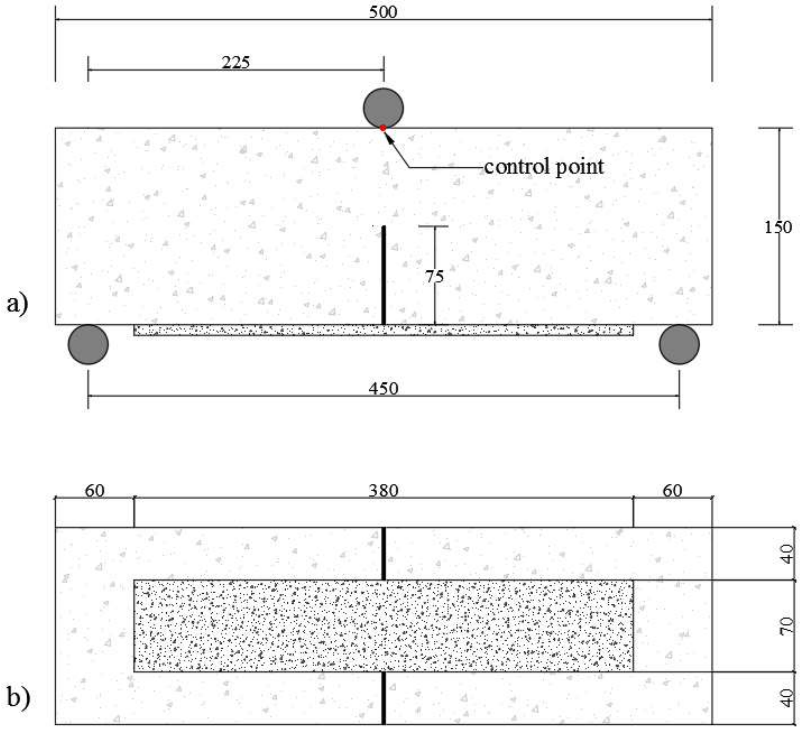

Figure 5.3 Specimen dimensions according to ASTM D7958/D7958M (2017) regulations (dimensions in mm): a) front view; b) bottom view

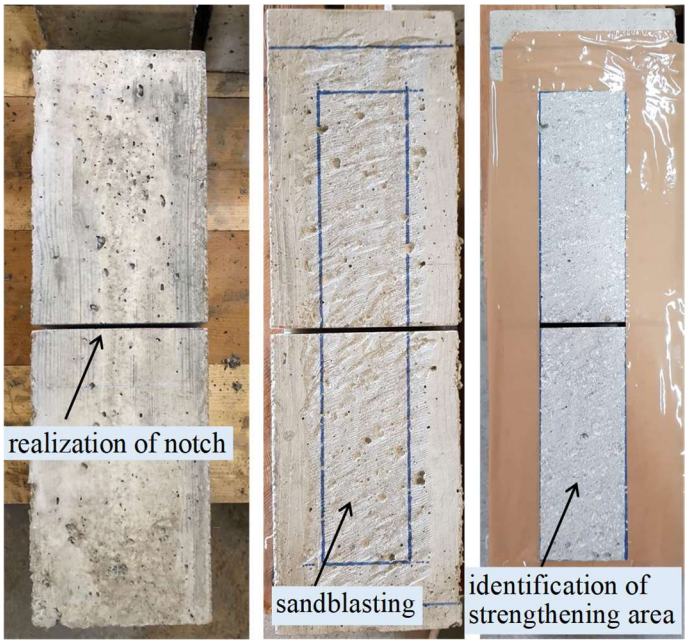

Figure 5.4 Preparation of concrete beams before application of the strengthening system

The two types of strengthening composite systems were then applied to the concrete bottom surface. With regard to the CFRP system, the main preparation phases (illustrated in Figure 5.5) are summarized below:

a. application of the primer according to the guidelines provided by the manufacturer datasheets;
b. after 24 hours, application of the first layer of resin (0.5 kg/m^2);
c. after 5 minutes, application of the carbon fabric with a small pressure;
d. after 5 minutes, application of the second layer of resin for completion (0.3 kg/m^2).

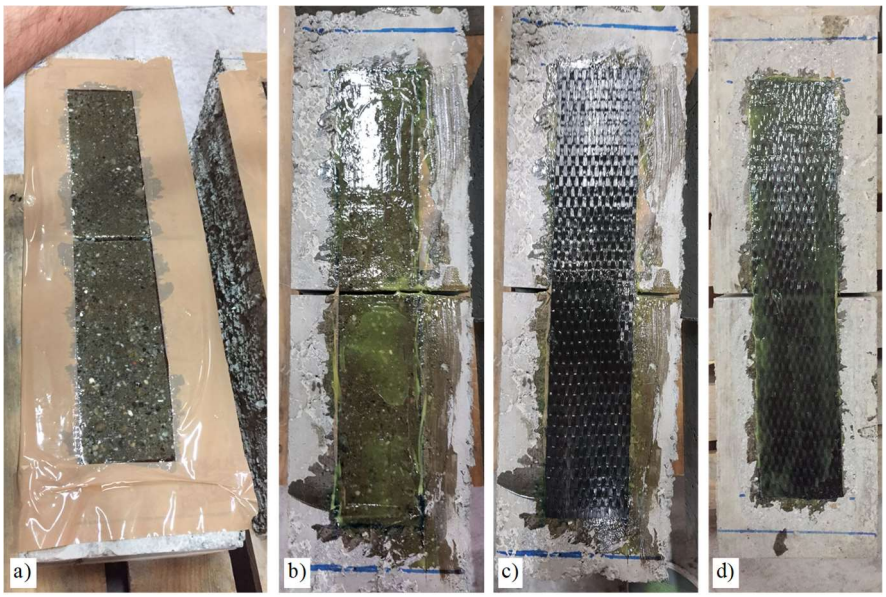

Figure 5.5 Application of FRP system: a) application of primer; b) application of first layer of resin; c) application of carbon fabric; d) application of second layer of resin

On the other hand, the main preparation phases of the FRCM system (illustrated in Figure 5.6) are the following:

a. wet of the bonding area with water;
b. application of the first layer of mortar (thickness 4 mm);
c. application of the PBO grid;
d. application of the second layer of mortar (thickness 4 mm).

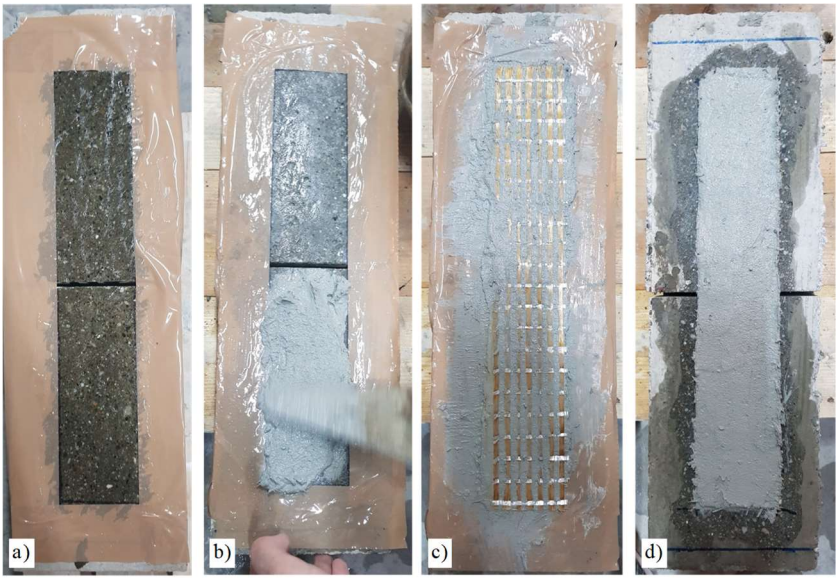

Figure 5.6 Application of the FRCM system: a) wet of bonding area; b) application of first layer of mortar; c) application of PBO grid; d) application of second layer of mortar

5.2.3 Test setup

Three-point bending tests in accordance with ASTM D7958/D7958M (2017) regulations were carried out, as previously illustrated in the sketch of Figure 5.3. The tests were performed using a universal testing equipment with 600 kN load capacity, under displacement controlled mode at a constant displacement rate equal to 0.2 mm/min for the FRCM-strengthened beams, and 0.05 mm/min for the FRP-strengthened beams. The load was recorded throughout the test with the integrated load cell of the testing equipment, while the deflection of the control point (cf. again Figure 5.3) was monitored using a linear variable displacement transducer (LVDT) rigidly connected to the roller used for the load application, as depicted in Figure 5.7. The tests were stopped when the load reduction after attainment of the peak load (descending branch) was 80%. Besides the load-displacement curve, for the FRCM-strengthened beams an indirect method to evaluate the stress-slip curve is elaborated through an analytical procedure as discussed in the next Section.

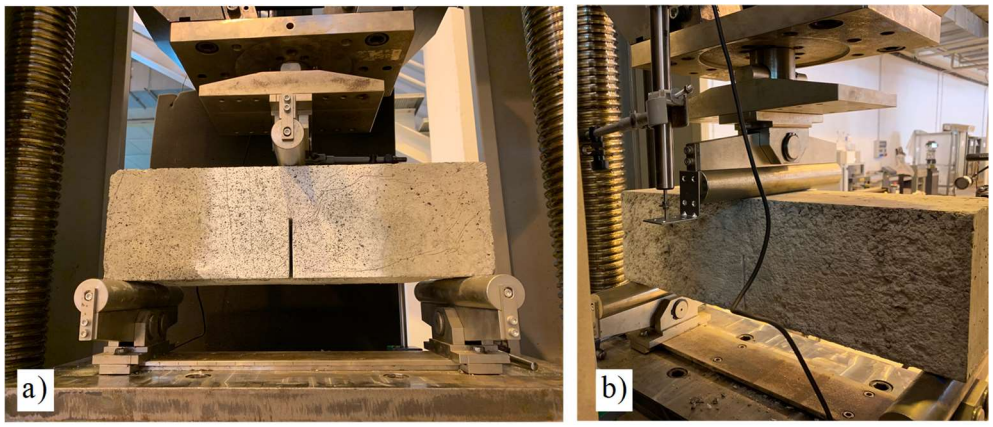

Figure 5.7 Test setup: a) front view of the specimen in three-point bending test configuration; b) details of the LVDT for the deflection measurement

5.2.4 Environmental conditioning

A total of 24 notched beams were prepared considering different environmental conditions. A group of 16 specimens (with both CFRP and PBO-FRCM system) were placed in a curing tank for 31 days with their bottom portion (having depth of around 20 mm) immerged in water at a controlled temperature as schematically illustrated in Figure 5.8. Two different temperatures were considered, namely a working temperature T_w = 30°C (8 specimens) and a critical temperature T_c = 50°C (8 specimens). Additionally, another group of 8 specimens (with both CFRP and PBO-FRCM system) were cured in air at laboratory environmental conditions (T_0 = 23°C and RH = 65-75 %).

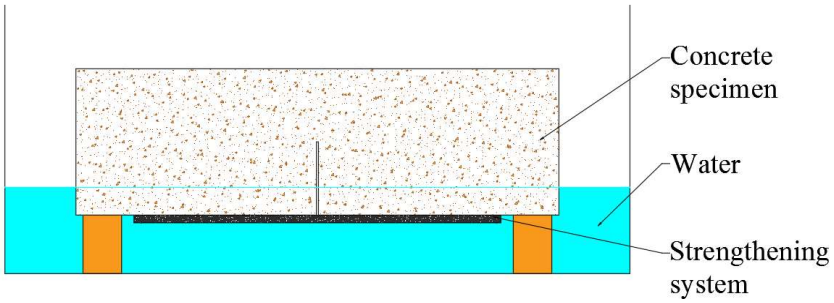

Figure 5.8 Layout of the environmental conditioning phase in curing tank at controlled temperature

The number of specimens for each class is reported in Table 5.VII Test program, where it can be noted that four repetitions for each case were made in order to obtain representative results of the different testing conditions.

Table 5.VII Test program

strengthening composite system	standard curing	partial immersion at 30°C	partial immersion at 50°C
CFRP	4	4	4
PBO-FRCM	4	4	4

The specimen nomenclature adopted in this work is "CFRP_T_i_j" for conditioned FRP-strengthened beams, and "FRCM_T_i_j" for conditioned PBO-FRCM strengthened beams, where $i = w, g$ depending on the conditioning temperature ($T_w = 30°C$ and $T_c = 50°C$), and j = 1,2,3,4 represents the number of sample within each class. The non-conditioned specimens are denoted as "CFRP_nc_j" and "FRCM_nc_j", respectively.

5.3 Experimental results

The results of the tests are presented here in terms of load-displacement curves and failure modes for both the PBO-FRCM and the CFRP system.

5.3.1 Force-displacement curves and failure modes of beams with PBO-FRCM system

In this subsection, the results in terms of force-displacement curves of notched beams are presented and the effect of the environmental conditioning is discussed. The force-displacement curves of the three classes of PBO-FRCM strengthened specimens (nc, T_w and T_c) are illustrated in the graphs of Figure 5.9, Figure 5.10 and Figure 5.11, respectively. It can be noticed that the shape of all the curves is similar, with a distinct first peak corresponding the attainment of the first cracking load of the beam, followed by a decrease of the load and a subsequent increase when the PBO fabric is fully engaged in resisting the further increase of load. Subsequently, there is another decrease of load until reaching an almost constant load level corresponding to the friction branch of the cohesive law between the PBO grid and the matrix. There is a relatively good agreement between the results of the four repetitions, especially for the T_c class of the specimens.

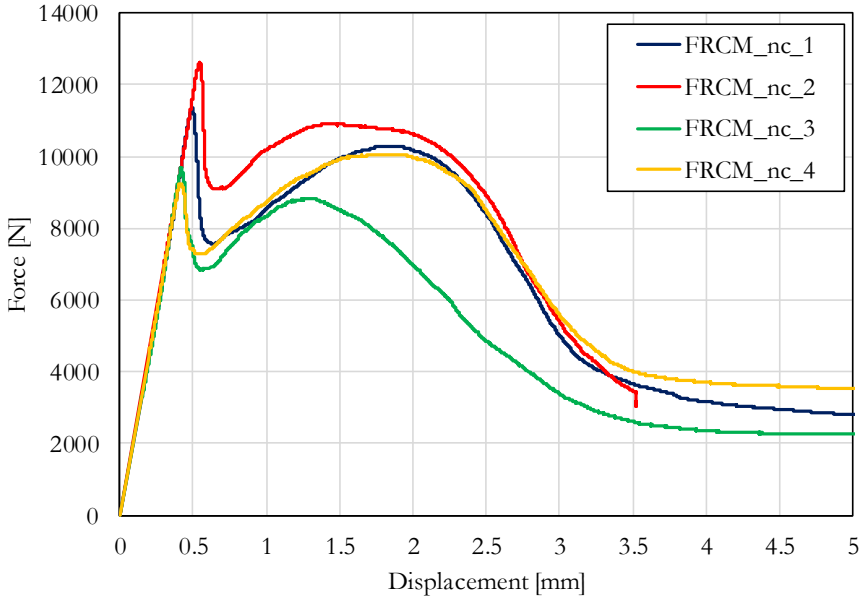

Figure 5.9 Force-displacement curves of non-conditioned beam specimens with PBO-FRCM system

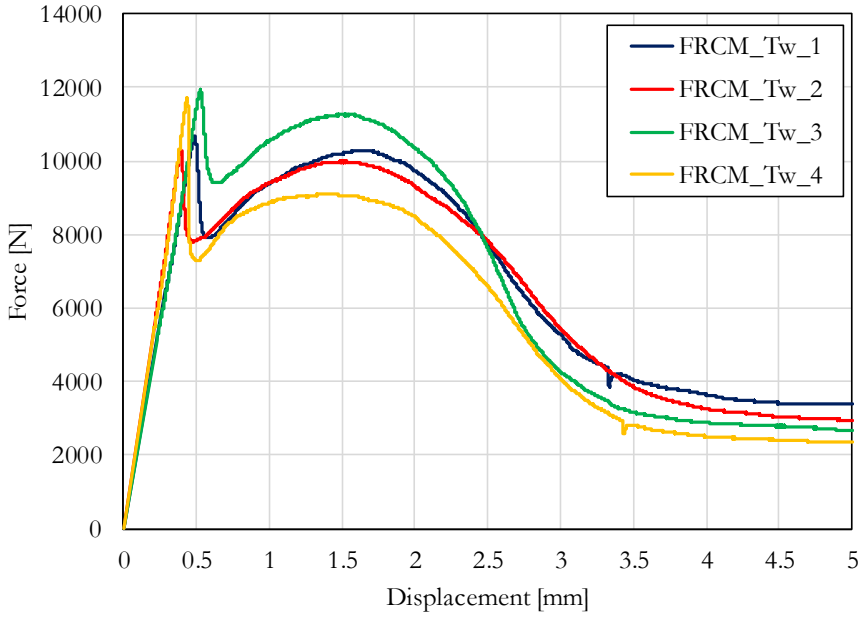

Figure 5.10 Force-displacement curves of beam specimens with PBO-FRCM system conditioned at temperature T_w=30°C

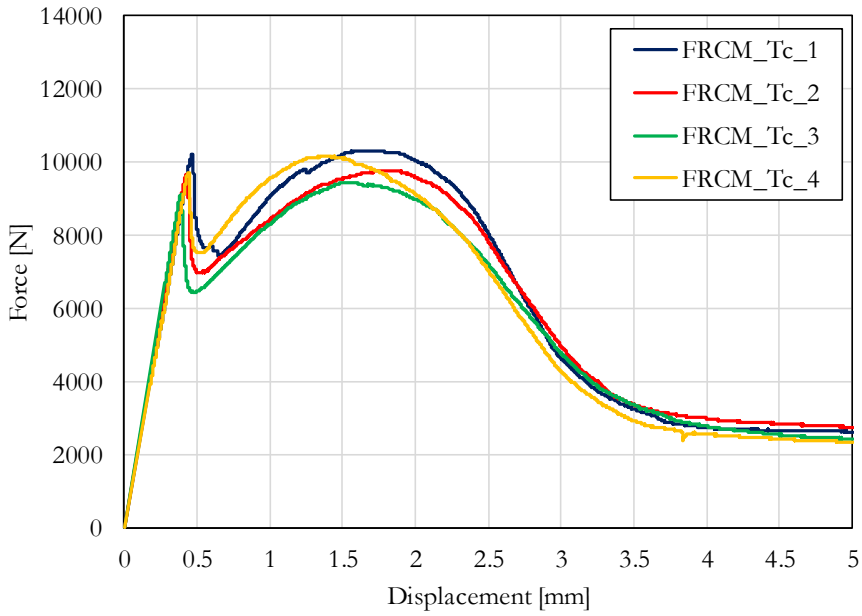

Figure 5.11 Force-displacement curves of beam specimens with PBO-FRCM system conditioned at temperature T_c=50°C

For all the tested beams with PBO-FRCM system, the failure mode is debonding of the PBO fabric from the mortar matrix.

The mortar remained attached to the concrete substrate and significant elongation of the fiber was noticed, see Figure 5.12. The crack starts from the notch tip and moves upwards until reaching the point of load application.

This particular failure mode depends by connection between PBO fabric and mortar matrix and geometrical sizes. In the following sections is described an indirect method that allow to correlate these results with the results of a different test setup (Single-Lap Shear test). In fact, Single-Lap Shear (SLS) test is the methodology used for evaluating and investigating the connection between matrix and fabric.

Many researchers from all over the world (Carloni et al. 2014) have investigated these parameters with SLS test and then, with analytical approaches (D'Antino et al. 2014), have found the cohesive law that describe the connection between mortar and fabric.

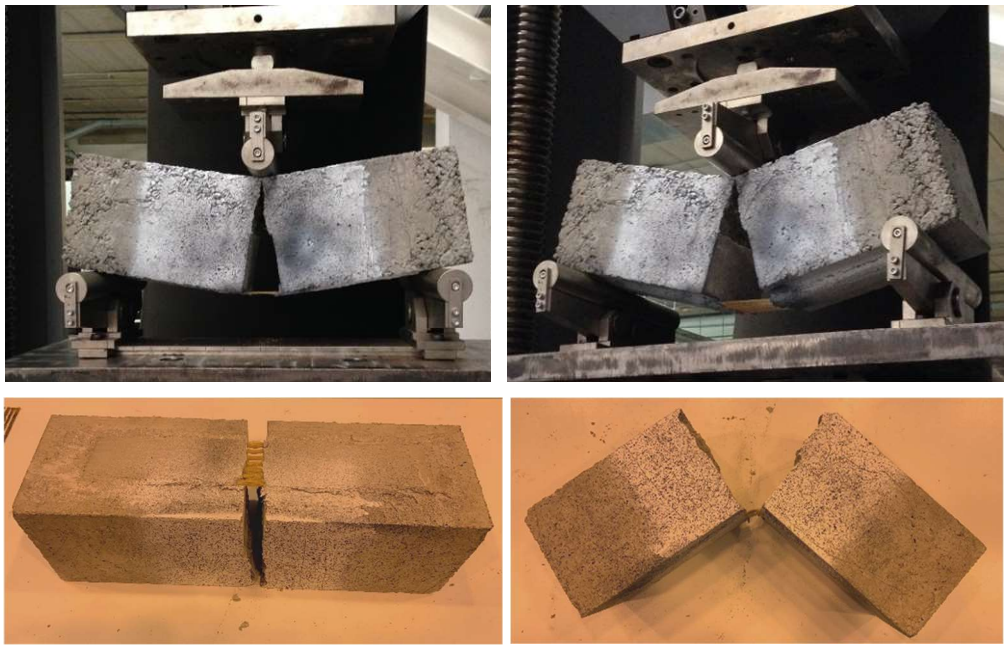

Figure 5.12 Typical failure of PBO-FRCM strengthened beams with significant elongation of the PBO fibers and mortar keeping attached to the concrete substrate

5.3.2 Force-displacement curves and failure modes of beams with CFRP system

On the other hand, the force-displacement curves of the FRP-strengthened beams are reported in Figure 5.13, Figure 5.14 and Figure 5.15 for the three classes (nc, T_w and T_c), respectively. It can be seen that the shape of the curve is quantitatively and qualitatively different from the curves of the PBO-FRCM system. Indeed, after an initial elastic branch, a degradation of the stiffness is observed, which is ascribed to the first cracking of concrete. The post-elastic branch is relatively short in comparison with the curves of the PBO-FRCM system, and the failure is sudden and brittle, typically caused by abrupt adhesive failure with subsequent detachment of the FRP sheet from the concrete substrate. It can be observed that the conditioning process at T_w = 30°C did not produce a reduction of the maximum bond strength. On the contrary, with the conditioning process at T_c = 50°C a clear degradation of the bond performance is noticed, which is consistent with the fact that such temperature is close to the glass transition temperature of the primer (cf. T_g value reported in Table 5.V). Considering that the transition phase does not occur suddenly but in a gradual manner, it can be concluded that for temperature values close to T_g the degradation phenomena clearly become manifest.

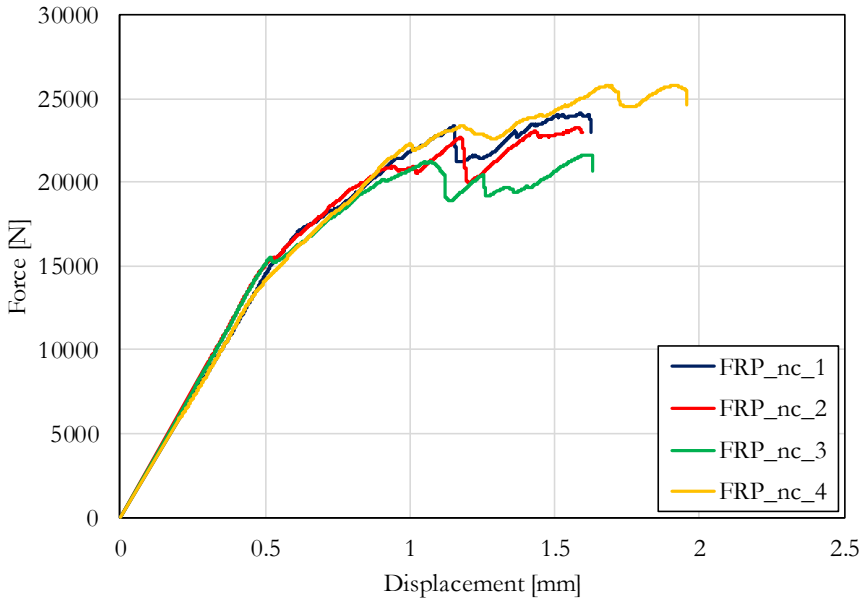

Figure 5.13 Force-displacement curves of non-conditioned beam specimens with CFRP system

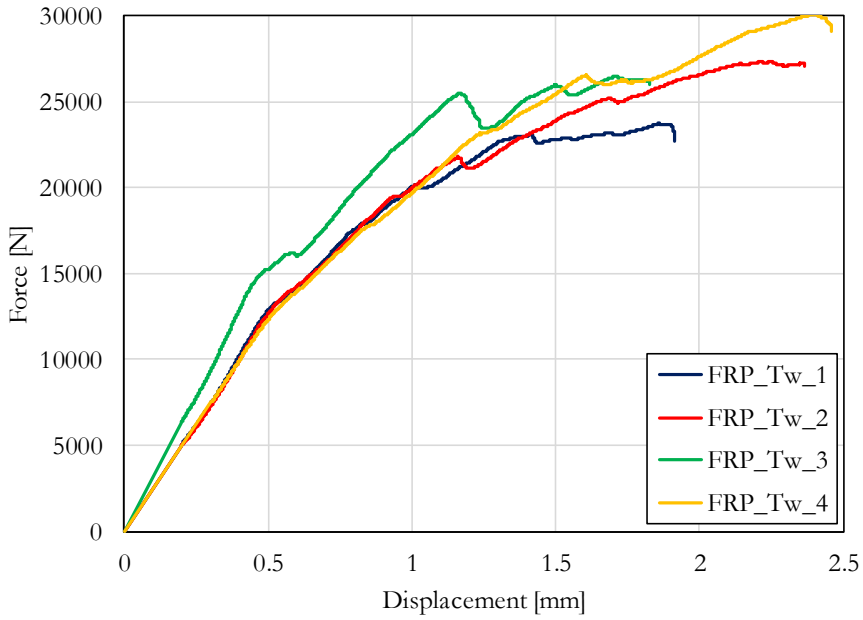

Figure 5.14 Force-displacement curves of beam specimens with CFRP system conditioned at temperature T_w=30°C

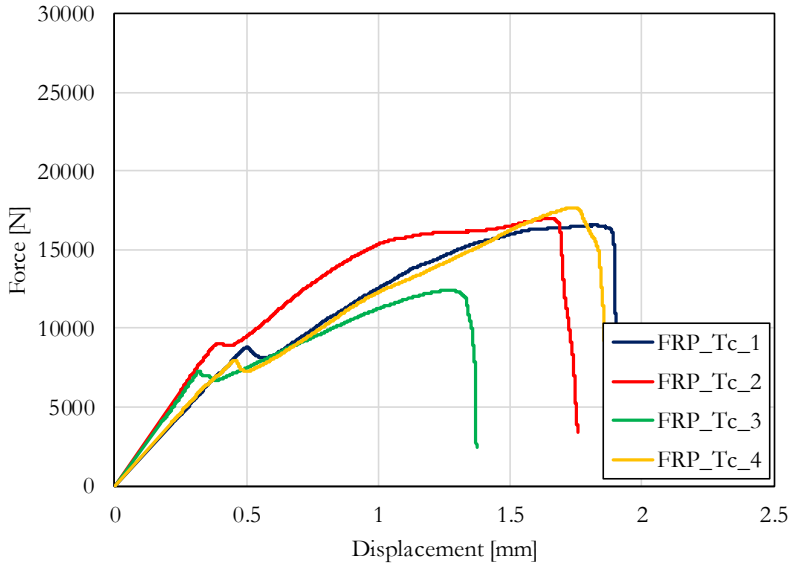

Figure 5.15 Force-displacement curves of beam specimens with CFRP system conditioned at temperature T_c=50°C

The typical failure modes of CFRP-strengthened beams are illustrated in Figure 5.16. The collapse of the beam was mainly ascribed to the adhesive failure in all the cases analyzed. However, some differences were noted between the different conditioning processes. In particular, for nc and T_w classes the adhesive failure was accompanied by a partial concrete detachment close to the mid-span of the beam. This phenomenon was not observed in the T_c classes due to a significant degradation of the bond behavior between CFRP and concrete.

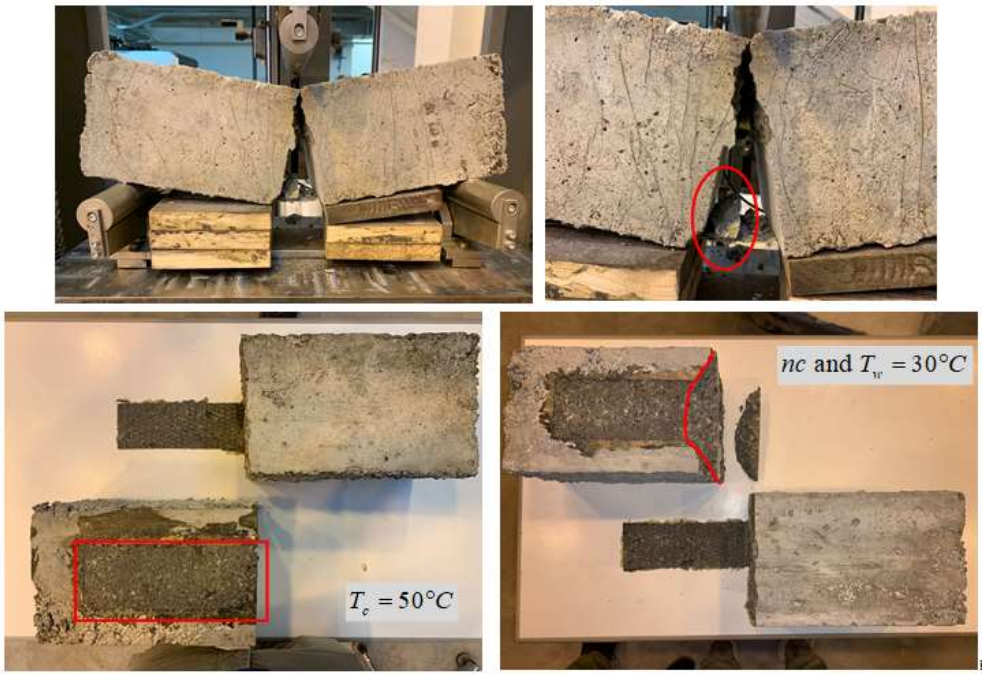

Figure 5.16 Typical failure of CFRP-strengthened beams with adhesive failure for T_c=50°C conditioning, and adhesive failure accompanied by partial concrete detachment for nc and T_w=30°C conditioning

5.4 Discussion of experimental results

In this section, experimental results are discussed and interpreted, in terms of force-displacement curves, failure modes and influence curing conditions. These are compared each other in order to verify the influence of moisture combined with high temperatures on composite systems.

An interpretation of force-displacement curve for FRCM system allows a comparison with results of a different test setup.

5.4.1 Interpretation of the force-displacement curve in the PBO-FRCM system

With regard to the PBO-FRCM system, after cracking of the beam, the failure mode was mainly ascribed to the sliding of the PBO grid from the mortar matrix. Consequently, the load-displacement curves of such beam specimens strengthened with PBO-FRCM system can be subsequently elaborated in order to extrapolate a representative stress-global slip curve at the interface between PBO fabric and mortar matrix, based on rigid body motion assumption after crack opening. In this regard, the typical shape of the load-displacement curve of PBO-FRCM strengthened notched beams is depicted in Figure 5.17.

Some characteristic points are reported in the curve, which are useful for the critical interpretation of the mechanical behavior of the strengthened beam. In particular, point A denotes the end of the linear elastic branch corresponding to the attainment of the tensile strength of concrete. With further load increase after point A, a short softening branch is observed up to point B, which is related to the residual tensile stress of cracked concrete in the range of small crack openings. In reality, a very similar descending branch in the load-displacement curve obtained through fracture mechanics tests of plain concrete was also reported in the literature (Carloni et al. 2017b and 2017c), (dashed segment A-Q). From point B onwards, the PBO-FRCM system is fully engaged and, in fact, the load-displacement curve follows a trend that resembles the typical shape of stress-global slip curve obtained with other testing procedures like single-lap and double-lap shear tests. More specifically, the load first increases from point B up to a maximum load point C and then decreases down to point D, which marks the initiation of the typical friction branch of the PBO-FRCM system (D'Antino et al. 2014).

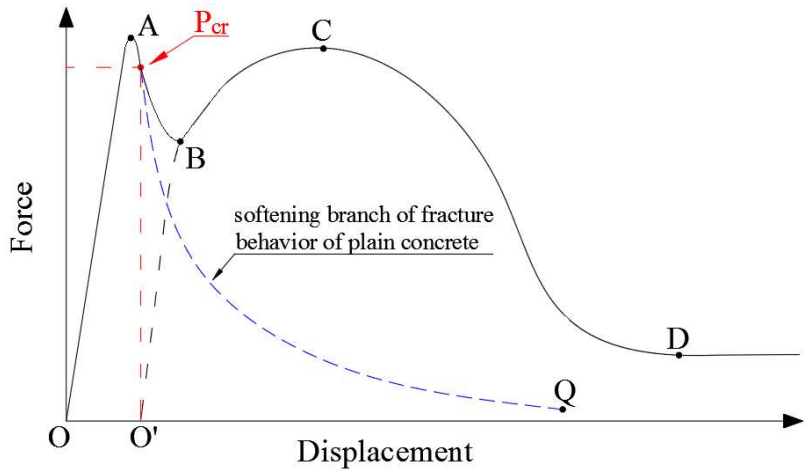

Figure 5.17 Representative Force-displacement curve of notched beam specimens

This second branch of the force-displacement curve (BCD) can be prolonged up to the zero load level (dashed line O'B). The load level corresponding to the deflection given by point O' in the beam force-displacement curve ideally indicates the cracking load of the mortar P_{cr}.

Therefore, the force-displacement curve of the beam can be interpreted in terms of two separate contributions: the beam contribution and the FRCM contribution. The FRCM contribution becomes manifest when debonding occurs, subsequent to cracking of the mortar (point P_{cr}).

Under this simplifying assumption, point O' represents the deflection level corresponding to the initiation of the debonding phenomenon, which makes it possible to correlate the results obtained by the adopted test procedure with results obtained by alternative and more widely used single-lap and double-lap shear tests.

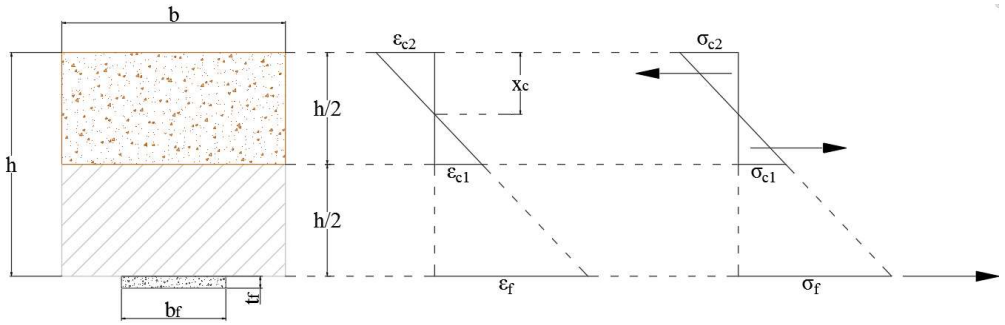

Figure 5.18 Distribution of strains and stresses in the mid-span cross-section of the beam for identification of load level of point A

To quantitatively check the validity of the mechanical interpretation of the force-displacement curve reported in Figure 5.17 against the experimental results shown in Figure 5.9 (or Figure 5.10, Figure 5.11), the equilibrium equations of the beam cross section are exploited. In particular, referring to the sketch of Figure 5.18, the translation and rotation (around centroid of FRCM system) equilibrium equations of the internal forces in the mid-span cross section of the beam are expressed as follows:

$$\begin{cases} E_c\varepsilon_{c2}\, b\frac{x_c}{2} - E_c\varepsilon_{c1}\frac{b}{2}\left(\frac{h}{2}-x_c\right) - E_{eff}A_{eff}\varepsilon_f = 0 \\ E_c\varepsilon_{c2}\, b\frac{x_c}{2}\left(h-\frac{x_c}{3}\right) - E_c\varepsilon_{c1}\frac{b}{2}\left(\frac{h}{2}-x_c\right)\left(\frac{2}{3}h-\frac{x_c}{3}\right) - \frac{F\ell}{4} = 0 \end{cases} \tag{5.1}$$

Where E_c is the Young's modulus of concrete, computed through the formula reported in Eurocode 2(UNI EN 1992-1-1:2015) from the cylinder compressive strength value f_{cm}; x_c is the neutral axis depth, b and h are the beam width and height, respectively, ε_{c1} and ε_{c2} denote the tensile and compressive strain in concrete, respectively, ε_f denotes the tensile strain in the FRCM system, F is the applied load and ℓ is the distance between the supports. The expressions (5.1) are applied to the state of incipient cracking of concrete (point A in Figure 5.17), i.e. assuming $\varepsilon_{c2} = \varepsilon_{ct}$, with $\varepsilon_{ct} = f_{ct}/E_c$ the ultimate tensile strain of

concrete. The two unknown variables in Eq. (5.1) are the neutral axis depth x_c and the load level *F*.

The goal is to compare the load level from the present section analysis with the load level of the first peak (point A) shown in the experimental force-displacement curves. It is not known whether cracking of concrete (point A) occurs prior or after cracking of mortar (point Pcr). For this reason, the contribution of the FRCM system is computed depending on the condition of the mortar (cracked or uncracked) as follows

$$\left\{E_{eff}, A_{eff}\right\} = \begin{cases} \left\{E_{mean}, A_{tot}\right\} & \text{for uncracked mortar} \\ \left\{E_f, A_f\right\} & \text{for cracked mortar} \end{cases} \tag{5.2}$$

In Eq. (5.2) E_{mean} represents the homogenized elastic modulus of the composite PBO-FRCM system comprising the PBO grid and the mortar, computed under the assumption of a perfect compatibility between the two materials before mortar cracking

$$E_{mean} = \frac{E_f A_f + E_m A_m}{A_{tot}} \tag{5.3}$$

where E_f, E_m denote the Young's modulus of fibers and mortar, respectively, while A_f, A_m indicate the corresponding effective area, with $A_{tot} = b_f \times t_f$ being the total area of the FRCM system (b_f=*70 mm* and t_f=*8 mm*). The area A_f, of the fibers is computed as

$$A_f = n \times b^* \times t^* \tag{5.4}$$

with n=7 being the number of bundles, and b^*, t^* representing the width and thickness of each bundle of fibers.

In other words, it is logical to assume that before cracking of the mortar, the FRCM system contributes to the internal equilibrium of the cross section with a homogenized modulus and the total area of the system. On the contrary, after cracking of the mortar, only the PBO fibers contribute to the internal equilibrium, so that the corresponding force is computed with area A_f, and Young's modulus E_f.

As a first step, the assumption of cracked mortar was made, the internal equilibrium conditions were solved and the actual strain at the level of the FRCM

system was computed based on the resulting neutral axis depth x_c from Eq. (5.1) . At this stage, it was possible to compare the strain of the FRCM system with the cracking strain of the mortar in order to verify the assumption of cracked mortar. With the given data of the beam and strengthening system, it was found that the strain at the FRCM level was lower than the cracking strain of the mortar. This meant that the cracking of the mortar occurred after (and not before) the attainment of the cracking of concrete, which is consistent with the sketch reported in Figure 5.17. Having verified this, the resulting neutral axis depth calculated through Eq. (5.1) was 38.96 mm and the corresponding load level was 8.78 kN, which is in reasonable agreement with the first peak load value shown in the experimental load-displacement curves. In reality, the latter value is slightly lower than the load level corresponding to the first peak of the experimental curves, which may be ascribed to the inherent uncertainties of the materials and of the simplifying assumption of plane section analysis.

For each force-displacement curve of the PBO-FRCM system, the two peaks of the curve corresponding to point A and to point C (see again Figure 5.17) are computed and listed in Table 5.VIII(denoted as F_A and F_C) together with the related mean value (out of each class of beams) and the Coefficient of Variation (CoV). A relatively low CoV value was obtained, below 10% for all cases except for the non-conditioned beams. It is easily seen that the environmental conditioning does not play a significant role on the main characteristics of the load-displacement curves. Indeed, the results corresponding to the T_w and T_c classes are not particularly different from the results related to the non-conditioned class. In order to demonstrate this behavior, in Figure 5.19 the mean results of F_A and of F_C are reported in a histogram format, along with the related error bar indicating the dispersion of the value with respect to the mean value. It can be noticed that the variation of both the peak values induced by the environmental conditioning is contained within the dispersion range of the non-conditioned class. This implies that the influence of the temperature is a factor that is not statistically significant for the considered beams strengthened with PBO-FRCM system.

This conclusion is limited to the "curing temperature" and not to the "test temperature", that could have an effect on the bond performance of the system.

Table 5.VIII Experimental results of three-point bending tests on beams with PBO-FRCM system

specimen name	F_A [kN]	μ_{F_A} [kN]	CoV_{F_A} [%]	F_C [kN]	μ_{F_C} [kN]	CoV_{F_C} [%]	Failure mode
FRCM_nc_1	11.37	10.73	12.58	10.30	10.03	8.72	DFM
FRCM_nc_2	12.62			10.92			DFM
FRCM_nc_3	9.67			8.83			DFM
FRCM_nc_4	9.25			10.07			DFM
FRCM_T_w_1	10.66	11.16	6.28	10.27	10.16	8.71	DFM
FRCM_T_w_2	10.28			9.99			DFM
FRCM_T_w_3	11.95			11.27			DFM
FRCM_T_w_4	11.73			9.12			DFM
FRCM_T_c_1	10.23	9.67	4.12	10.32	9.92	4.00	DFM
FRCM_T_c_2	9.64			9.76			DFM
FRCM_T_c_3	9.10			9.43			DFM
FRCM_T_c_4	9.70			10.15			DFM

μ_k **: mean value of** k**;** CoV **coefficient of variation; DFM: debonding of PBO fabric from matrix**

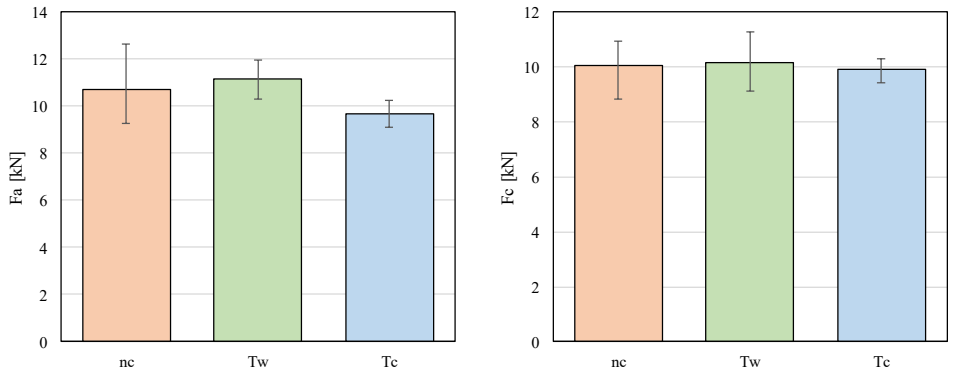

Figure 5.19 Influence of the environmental conditioning on the first peak load F_A (left) and on the second peak load F_c (right) of the Force-displacement curve of beams with PBO-FRCM system

5.4.2 Indirect method to evaluate the interfacial stress-slip curve for FRCM system

Unlike other studies from the literature that used the single-lap and double-lap shear test, the present experimental campaign is based on a beam test setup. It is, therefore, of interest to establish a procedure to allow a comparison between the two different test setups. To this aim, the observation of the beam after the achievement of the cracking of concrete revealed that the load was mainly resisted

by the FRCM system, with a very small zone of concrete in compression, see for instance the photograph of the beam reported in Figure 5.12. Based on a rigid-body assumption, it is possible to link the vertical displacement of the beam (and the corresponding vertical load) with the corresponding relative slip between PBO grid and mortar (and corresponding stress level), so as to evaluate the stress-global slip curve that is an essential piece of information for the bond performance of the PBO-FRCM system.

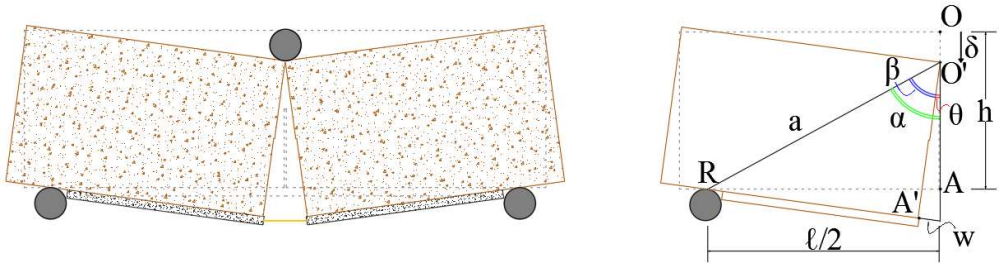

Figure 5.20 Analysis of right-body motion of the PBO-FRCM strengthened beam and evaluation of rotation angle for the determination of the stress-global slip curve of the bond behavior

With reference to Figure 5.20, it is observed that a vertical deflection of the control point equal to δ produces a rotation angle θ of each half of the beam that is given by the difference between the angles α and β . The values of the angles α and β are easily determined through simple trigonometric expressions as follows

$$\alpha = \tan^{-1}\left(\frac{\ell}{2(h-\delta)}\right)$$
$$\beta = \cos^{-1}\left(\frac{h}{\mathrm{a}}\right) \tag{5.5}$$

where $\mathrm{a} = (h-\delta)/\cos\alpha$ is the length of the segment connecting the control point O (in the deformed configuration) and the roller point R. As a result, the rotation angle θ is an explicit function of the deflection δ according to the following expression

$$\theta = \tan^{-1}\left(\frac{\ell}{2(h-\delta)}\right) - \cos^{-1}\left(\frac{h}{\mathrm{a}}\right) \tag{5.6}$$

Once the rotation angle is computed, the global slip w of the PBO grid from the mortar is given by

$$w = h \tan\theta \tag{5.7}$$

On the other hand, the tensile force T acting on the PBO grid can be evaluated through the equilibrium of the internal forces:

$$T = \frac{F\,\ell}{4h} \tag{5.8}$$

from which the corresponding stress is obtained by dividing T with the area A_f of the fibers given by (5.4)

$$\sigma = \frac{T}{A_f} \tag{5.9}$$

Consequently, from the load-displacement curve of the adopted beam test setup, it is possible to determine a stress-global slip curve $\sigma - w$ representative of the bond behavior at the interface.

As an example, the stress-global slip curve obtained through the proposed procedure for beam specimen FRCM_nc_1 is reported in Figure 5.21. The first branch (dashed line) is related to the initial beam behavior, before full engagement of the FRCM slip from the mortar matrix takes place. The second branch (solid line) is related, instead, to the bond behavior between PBO fabric and mortar. It is worth noting, not only that this second branch is qualitatively similar to the shape of the curve obtained with the single-lap test setup, but also, that the computed stress and global slip values of the proposed procedure are in reasonable agreement with the values obtained with the PBO-FRCM system reported in the literature for an effective bond length of 200 mm (D'Ambrisi et al. 2013), that is very close to the effective bond length of the present experimental campaign of 190 mm.

Single-lap Shear tests with 190 mm of bond length could be performed in order to better compare the two tests setup.

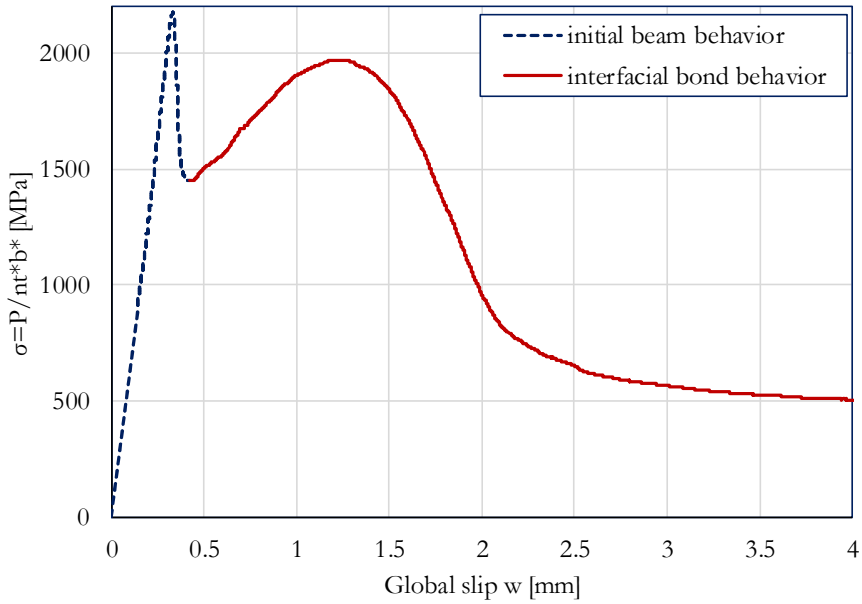

Figure 5.21 Stress-global slip curve obtained by processing the force-displacement results of the notched beam test setup for FRCM_nc_1 specimen

5.4.2 Influence of environmental conditioning on the CFRP system

A quantitative assessment of the influence of the environmental conditioning on the bond strength of the CFRP system can be evaluated by inspection of Table 5.IX. In particular, it can be noticed that the mean value of the peak load decreased more than 30 % in passing from non-conditioned to conditioned class at 50°C.

On the other hand, the peak load results, for the conditioning class at 30°C, are, on average, higher than those of the non-conditioned beams. However, as can be clearly observed in the histogram of Figure 5.22, this slight increase of maximum load overlaps with the variation range of the non-conditioned class, which implies that these results are not statistically significant.

On the contrary, the marked reduction observed in the T_c class is well below such variation range of the non-conditioned class, and this confirms that the FRP system is negatively affected by the environmental conditioning even for short duration of the conditioning phase (31 days).

This result is in line with other literature studies (Ceroni et al. 2017).

Table 5.IX Experimental results of three-point bending tests on beams with CFRP system

specimen name	F_{max} [kN]	$\mu_{F_{max}}$ [kN]	$CoV_{F_{max}}$ [%]	Failure mode
CFRP_nc_1	24.14	23.72	7.30	AF + PCD
CFRP_nc_2	23.26			AF + PCD
CFRP_nc_3	21.66			AF + PCD
CFRP_nc_4	25.81			AF + PCD
CFRP_T_w_1	23.72	26.90	9.71	AF + PCD
CFRP_T_w_2	27.32			AF + PCD
CFRP_T_w_3	26.48			AF + PCD
CFRP_T_w_4	30.06			AF + PCD
CFRP_T_c_1	16.56	15.90	14.91	AF
CFRP_T_c_2	16.98			AF
CFRP_T_c_3	12.41			AF
CFRP_T_c_4	17.66			AF

μ_k **: mean value of** k**;** CoV **coefficient of variation; AF: adhesive failure; PCD: partial concrete detachment**

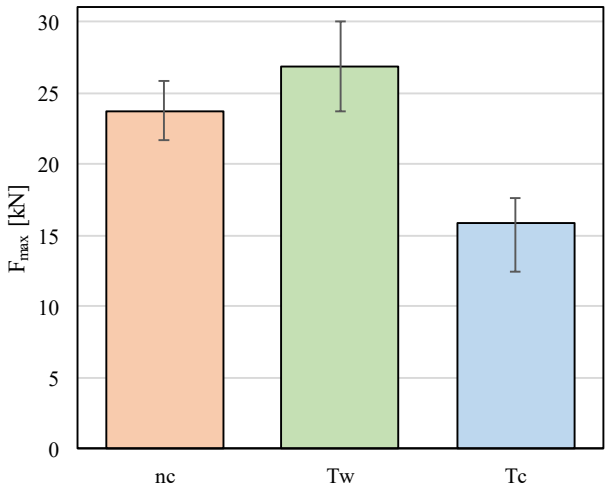

Figure 5.22 Influence of the environmental conditioning on the peak load (F_{max}) of the Force-displacement curve of CFRP-strengthened beams

From the histogram in Figure 5.22 a strong reduction of 30% of the peak load was observed for the curing period at 50°C.

5.5 Conclusion

This experimental study has dealt with the bond behavior of CFRP and PBO-FRCM systems adhesively bonded to concrete substrate through a beam test setup on notched specimens.

Different environmental conditions consisting of immersion of the strengthening system in water at temperature of 30°C (T_w) and 50°C (T_c) for a period of 31 days, as well as classical curing process in air at environmental conditions were considered.

The main contents and findings of this research work are summarized as follows:

1. The PBO-FRCM system was not affected by the environmental conditions, and the results in terms of peak load and ultimate displacement for the conditioned specimens were of comparable order to those of the non-conditioned specimens;
2. Although conceived for FRP system, the adopted test setup on notched beams was used likewise in the FRCM system. Under some simplifying assumptions, this test setup allowed the evaluation of the stress-global slip curve of the PBO grid–mortar matrix, which turned out to be in reasonable (qualitative and quantitative) agreement with the curves obtained through the more widely used single-lap shear test setup reported in literature;
3. The CFRP system was sensitive to the curing conditions at temperature of 50°C, which is close to the glass transition temperature of the primer/epoxy. Despite the relatively short period of application of this conditioning phase, this curing condition produced a reduction of the average peak load of more than 30% in comparison to the corresponding average load of the non-conditioned specimens. For the curing conditions at temperature of 30°C no reduction of the average peak load was observed.

Results presented in this experimental campaign represent a starting point of a more extensive investigation. Below are some interesting lines of future research:

- The study should be extended to include longer and smaller curing/conditioning periods (e.g. from 7 days to 6 month);

- The study should be extended to include lower and higher temperatures (closer or even above the glass transition temperature of the epoxy resin);
- Different effective bond lengths and widths should be studied in order to more carefully analyze the differences of this test setup compared to the single-lap shear test;
- Other FRCM strengthening systems with alternative fiber materials (basalt, carbon, glass, etc.) could be investigated.

Chapter 6

FEM Models of FRCM

Depending on the application, FRCM materials can be an effective alternative to the FRP, because of their excellent performance also under elevated temperatures, good chemical and aesthetical compatibility with the concrete and masonry substrates, and applicability in presence of surface moisture or on uneven substrates.

In this Chapter, numerical model of FRCM systems are presented. Augmented-Finite Element Method is the principal innovation of this section. In fact, this approach allows the formation of arbitrary crack in the material domain. Two and three-dimensional models are developed and discussed in the following parts.

6.1 2D Finite Element model using Augmented-FEM

In this paragraph, the results of a 2D numerical simulation using Augmented Finite elements are presented. The main aim is to develop a numerical strategy of modelling in order to have a tool for optimizing FRCM systems.

In addition, in this study, the focus was on PBO fabric, but the same assumptions and simplifications at base of the models can be applied for different nature of fabric (carbon, aramid, glass and etc.). Preliminary results of direct tensile model (Urso et al. 2019) have shown that the present model is able to reproduce the constitutive behavior of a FRCM material. Then, with parametric studies, the model was validated and applied to a different test setup (Single Lap Shear test). Numerical results present a good agreement with the experimental ones but due to a limitation of 2D simulation, unfortunately it was not possible applying it in a strengthened beam.

6.1.1 Introduction

Mechanical behavior of FRCM materials has been analytically studied by some authors, using a fracture mechanics approach (D'Antino et al. 2014). Analytical models were developed to predict the experimental data in order to

explain the behavior at the FRCM fabric-matrix and matrix-substrate interfaces (D'Antino et al. 2018).

These interface models are used to create the *cohesive elements*, used in the Finite Element Analysis (FEA). Currently, there are different FRCM system commercially available, which vary both in fabric types (PBO, glass, carbon, basalt, aramid) and proprietary inorganic matrices. In this study, the analytical formulation from literature were used to describe the cohesive behavior between different interfaces, and FRCM was numerically modeled using a 2D Augmented Finite Element Method (A-FEM) (Liu et al. 2014 and 2015). Two types of specimen boundary conditions were modeled: the direct tensile test and single-lap shear test.

For the direct tensile test, the geometry and boundary conditions of the numerical model were representative of an FRCM coupon per ICC-ES document AC434 (2013).

AC434 (2013) is the acceptance criteria for the FRCM materials issued to provide interested parties with guidelines for demonstrating compliance with model building the codes. Particularly, Annex A of AC434 (2013) summarizes the test method to characterize the mechanical properties of FRCM. Test setup is shown in Figure 6.1.

Figure 6.1 Direct tensile test setup configuration according to AC434

For the single-lap shear test, the geometry and boundary condition of numerical model were representative of an FRCM-concrete specimen per RILEM (2018). The aim of this recommendation is to describe a standardized shear bond test method to characterize the Textile Reinforced Mortar (TRM)-to-substrate bond behaviour.

In this configuration, shown in Figure 6.2,the fabric is pulled out from mortar matrix that is connected to a rigid block of concrete. Doing test with different length of the bonded area is possible study cohesive law between fabric and mortar. Many authors [Carloni et al.] have studied this problem and found an analytical solution.

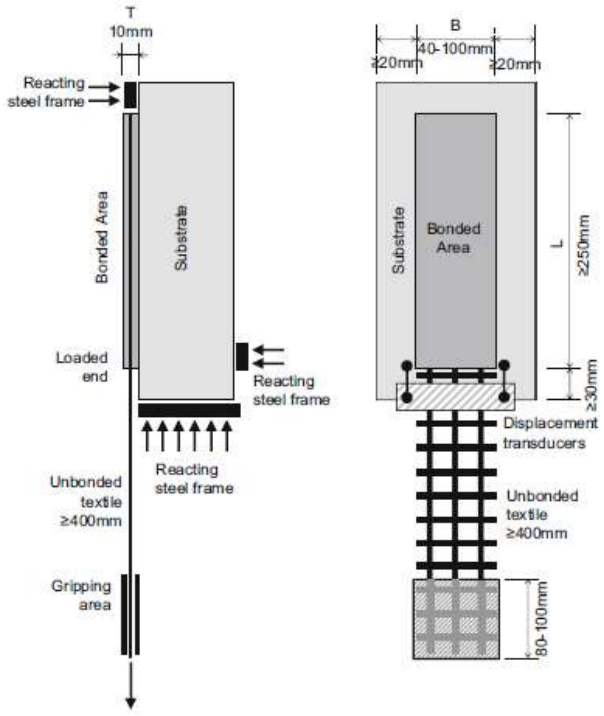

Figure 6.2 Single-lap Shear test setup configuration according to Rilem

With this test protocol is possible to study the six failure modes. Experimental results of Carloni works (Carloni et al. 2014) showed the same failure mode that is sliding of the textile within the matrix (Figure 6.3).

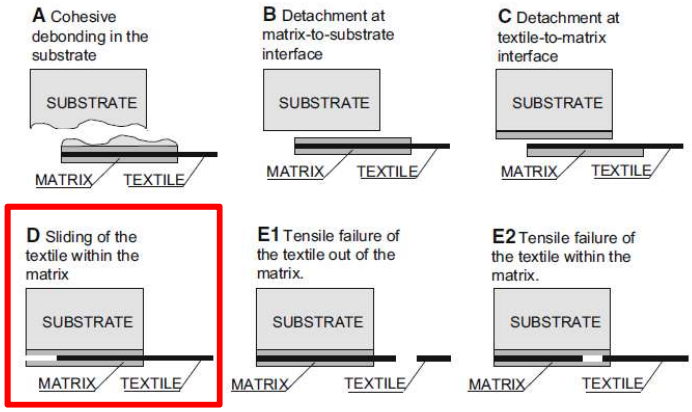

Figure 6.3 Six different failure mode for Single-Lap Shear test

Parametric studies on the effect of number of cracks, location of cracks, and number of layers were conducted in order to evaluate the effect of these parameters on final results. The A-FEM model was able to capture the tensile behavior of FRCM coupon in terms of stiffness stress, and strain.

Results show also that after reaching a certain crack number, the effect of number of cracks on the overall mechanical properties of the coupons was minimal. As evidenced in experimental tests, the two important crack location were close to steel tabs, in which a concentration of stress led to first crack.

6.1.2 Augmented Finite Element Method (A-FEM)

In this study, we shall explicitly model the initiation and propagation of cracks in concrete using a recently developed augmented finite element method (A-FEM) by Yang and colleagues. The major advantage of the A-FEM in fracture modeling is that it can account for the initiation and propagation of multiple cracks in solids without the need of introducing additional Degrees of Freedom (DoFs). (Liu et al. 2013, 2014 and 2015).

Thus, the problem size of a numerical model remains the same no matter how many cracks are generated in it. Furthermore, the method permits the derivation of explicit, fully condensed elemental equilibrium equations of mathematical exactness for piece-wise linear Cohesive Zone Method (CZM), greatly reducing the numerical error accumulation (numerical drifting). This is achieved by a non-traditional consistency-check based algorithm for the nonlinear element condensation procedure (Liu et al. 2015). The formulation also allows for repetitive augmentation of the same element to host more than one cracks, thus allowing for arbitrary crack merging or bifurcation without extra numerical cost.

Here we briefly summarize the key equations only. We choose to work with the 4-node tetrahedron element since is more amicable to complex geometries and has the simplest crack configurations if it is deemed to fracture. The two cut configuration is shown in Figure 6.4.

Before a crack is initiated, an A-FE is a standard continuum element. If the stresses in an element meets an initiation criterion, it is cut by a crack into two subdomains (Ω^+ and Ω^-), from which two new surfaces, Γ_c^+ and Γ_c^- (with unit out-normal of $\mathbf{n}_c$) are generated, as shown in Figure 6.5. The weak form of the governing equations for the mechanical and thermal equilibrium, according to the principle of virtual work, is

$$\int_{\Omega^{+/-}} \boldsymbol{\sigma} : \nabla \delta\mathbf{u} \, d\Omega = \int_{\Gamma_t^{+/-}} \bar{\mathbf{t}} \cdot \delta\mathbf{u} \, d\Gamma + \int_{\Gamma_c^{+/-}} (\boldsymbol{\sigma} \cdot \mathbf{n}_c) \cdot \delta\mathbf{u} \, d\Gamma \tag{6.1}$$

Where $\boldsymbol{\sigma}$, and $\delta\mathbf{u}$ are stresses and virtual displacements, respectively. $\bar{\mathbf{t}}$ is the surface traction between the cracked surfaces, which is continuous across the crack surfaces. $\mathbf{t}_c = (\mathbf{t}_c^- = -\mathbf{t}_c^+)$ and $q_c (= q_c^- = -q_c^+)$, are functions of crack displacement and temperature jump across the discontinuity, i.e.,

$$\mathbf{t}_c = \mathbf{t}_c(\Delta\mathbf{u}) = \mathbf{t}_c(\mathbf{u}^+ - \mathbf{u}^-) \qquad \text{on } \Gamma_c \tag{6.2}$$

For typical quasi-brittle materials such as mortar and concretes, a widely used crack initiation criterion is the maximum principal stress criterion, which states that once the maximum principal stress (averaged over the element volume) reaches the cohesive strength ($\hat{\sigma}$), a cohesive crack shall be inserted to the element with a direction perpendicular to the maximum principal direction ($\mathbf{n}$). This criterion is adopted in this study.

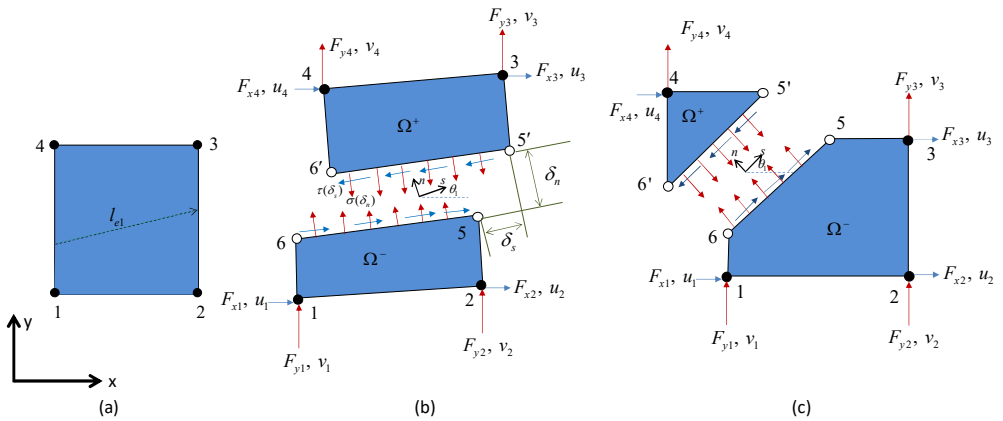

Figure 6.4 Illustration of an element from (a) a regular element, to (b) an A-FE with two quadrilateral sub-domains, or to (c) an A-FE with one triangular sub-domain and one pentagonal sub-domain

At element level, Eqn (6.1) can be discretized using linear shape functions into

$$\left(\int_{\Omega^{+/-}} \mathbf{B}^{\mathrm{T}}\mathbf{D}\mathbf{B}\ \mathrm{d}\Omega\right)\mathbf{u} = \int_{\Gamma_t^{+/-}} \mathbf{N}^{\mathrm{T}}\bar{\mathbf{t}}\mathrm{d}\Gamma + \int_{\Gamma_c} \mathbf{N}^{\mathrm{T}}\mathbf{t}_c\mathrm{d}\Gamma \tag{6.3}$$

Here $\mathbf{N}$, $\mathbf{B}$, and $\mathbf{D}$ are the shape function matrix, the strain matrix and the material stiffness matrix, respectively.

Further discretization of Eqn (6.3) into standard matrix form of the condensed elemental equilibrium has been derived in detail in (Liu et al. 2013, 2014 and 2015) and we shall not repeat it here. The element has been incorporated into a commercial software package ABAQUS as a user defined element.

The method has demonstrated a much improved numerical efficiency, accuracy, and robustness (in many cases by 2~3 orders of magnitude as compared to the eXtended-FEM (X-FEM) in ABAQUS (Liu et al. 2013, 2014 and 2015). The A-FEM is further empowered by a novel stabilizing method named inertia-based stabilizing method that can effectively overcome the severe convergence difficulty caused by rapid propagation of small cracks which frequently occur in composite and quasi-brittle materials (Gu et al. 2015).

6.1.3 Assumptions and simplifications

2D models were created using A-FEM formulation and cohesive elements. The coupon geometry for both boundary conditions is consistent with that of the AC434, with a unitary thickness. Two layers of mortar and one layer of fabric were modelled and connected by zero-thickness cohesive elements for the model with one layer of fabric. Additionally, models with two and three layers of fabric were studied in direct tension in order to validate the numerical approach and test its potential.

The assumptions of the model were the following:

i. The two layers of mortar are identical and modeled as a continuous layer with unit thickness;
ii. the fabric was modeled as a continuous layer with unit width;
iii. the cohesive law was modified based on the realistic area of fabric, A_f, and mortar, A_m (see Figure 6.6);
iv. the mortar within the fabric openings is modeled with "link-cohesive elements" in order to connect the two layers of mortar and provide stress transfer between the mortar layers.

Assumption ii. was necessary because of the limitation of a 2D model in representing the geometry in the third direction (direction perpendicular to the model's plane).

Geometrical homogenization of the fabric layer was needed to account for the discontinuity in the third direction due to grid spacing, as shown in Figure 6.5 cross-section. Thus, the cross-section became a *continuous layer of uniform thickness*. As consequence a new Young's modulus was evaluated based a weight average between fabric and mortar in that layer. This new elastic modulus was used for the analysis.

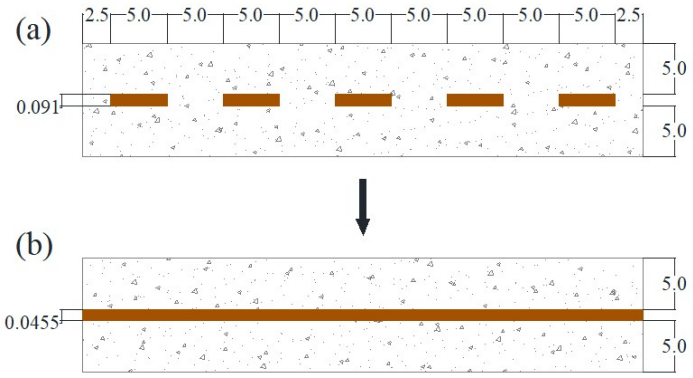

Figure 6.5 Real cross-section of sample for direct tensile test [mm], (b) Homogenized model geometry

Similar to the Young's modulus, the cohesive law (calibrated for the realistic fabric geometry) had to be adjusted to fit the assumed fabric geometry. In Figure 6.6 is represented a detail of top view of the fabric-mortar geometry in order to better understand contribution of area of fabric and area of mortar within.

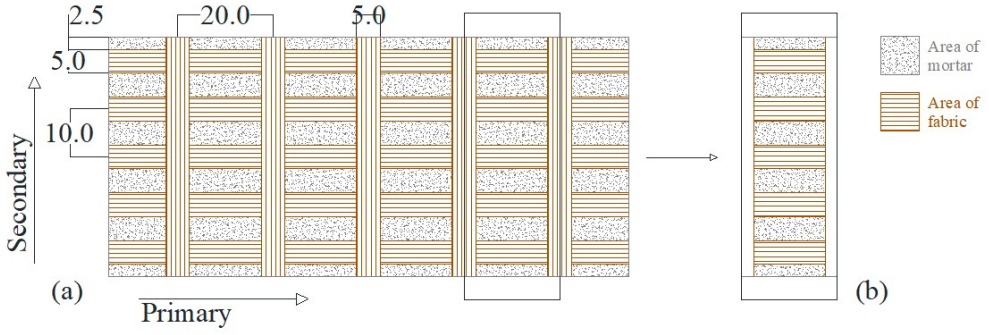

Figure 6.6 (a) Top view of the fabric mortar geometry, (b) detail of contribution of mortar within and fabric

Geometry

The model geometry and boundary conditions, shown in Figure 6.7, represent a direct tensile test coupon according to the AC434. The nominal thickness of the mortar layers was 5 mm, and the equivalent thickness of fabric layer was 0.0455 mm, per manufacturer's data sheet.

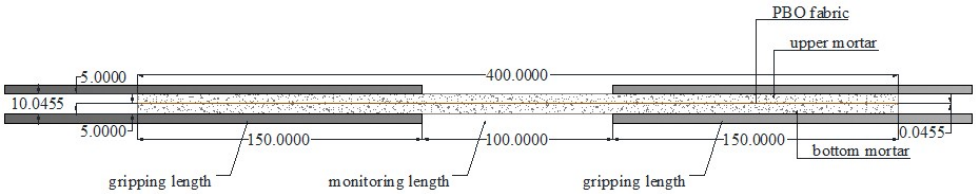

Figure 6.7 Single layer specimen for direct tensile test [mm] according to AC434

Mesh

The 2D A-FEM used 4-node bilinear finite elements identical to the 4-node elements in standard FEM in ABAQUS. Because the elements were homogeneous with an isotropic material, only two material properties were required: Young's modulus (E) and Poisson's ratio (υ).

The size of the elements used for fabric were 0.4000 mm x 0.0455 mm and for mortar were 0.4 mm x 1.0 mm in order to connect nodes in the same position, as shown in Figure 6.8. The element sizes were chosen to provide a geometric ratio less than 10, to avoid numerical convergence issues.

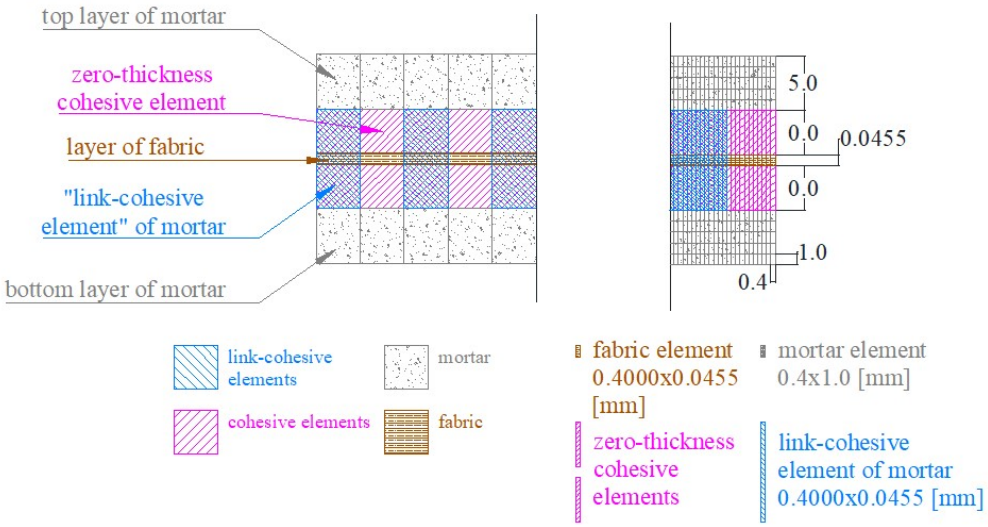

Figure 6.8 Mesh size of different elements [mm] – schematic figure

The cohesive elements had zero thickness as shown in Figure 6.8. Other elements called *link-cohesive elements* were also used to connect the two layers of mortar and to take into account the mortar-to-mortar stress transfer inside the fabric openings. It should be noted that the FRCM fabric has openings to allow a proper mortar penetration, as shown in Figure 6.5.

Boundary conditions and applied displacement (direct tension)

The boundary conditions were applied on the external nodes of the bottom and upper mortar layers, for the first 150 mm, in order to simulate the steel tabs. In those nodes, the displacements in both directions x-y were restrained, as shown in Figure 6.9.

The uniform displacement was applied on the external nodes of the bottom and upper mortar layers, for the end 150 mm in order to simulate the displacement applied by the use of steel tabs and clevis grips per AC434.

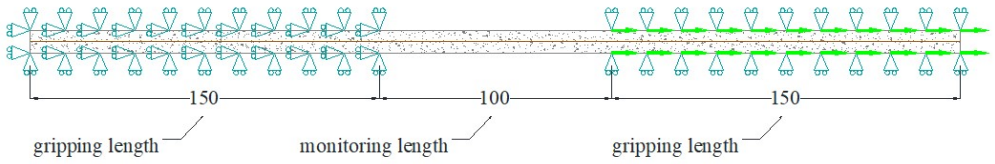

Figure 6.9 boundary and conditions for direct tension simulation

Materials

Material mechanical properties were taken from data sheet and summarized in the Table 6.I.

Table 6.I Mechanical properties of PBO fabric and mortar

Material	E [GPa]	υ	σ_c [MPa]	σ_t [MPa]	t^* [mm]
PBO fabric	270	0.3	/	5800	0.0455
Mortar	7	0.2	40	4	/

Fracture parameters for the mortar were taken from Carloni's studies(Carloni et al. 2017)and summarized in Table 6.II.

Table 6.II Fracture properties of mortar

Material	σ_t [MPa]	τ [MPa]	G_I [N/mm]	G_{II} [N/mm]
Mortar	4	2	0.05	0.2

As previously mentioned, homogenizing the middle layer of fabric, a new modulus of elasticity was evaluated:

$$E_h = \frac{E_f A_f + E_m A_m}{A_t} = 138.5\ [GPa] \quad (4)$$

Cohesive Laws for Mortar Fracture

As previously mentioned, the fracture process in A-FE is modeled with a cohesive zone model (CZM) with triangular traction-separation laws as illustrated in Figure 6.10. This simple CZM has been used to model mortar fracture successfully in many studies in literature (Liu et al. 2013, 2014 2015 and Moës & Belytschko 2002).

For each pure fracture mode, three CZM parameters are needed:

i. the cohesive strength for mode I $(\hat{\sigma})$ and mode II $(\hat{\tau})$;
ii. the critical displacements for mode I (δ_{nc}) and mode II (δ_{nc});
iii. the ratio of elastic-limit displacement (δ_{n1} and δ_{t1}) to the respective critical displacement: λ_{n1} for mode I and (λ_{t1}) for mode II. We note that these two parameters are of secondary importance and typically set to be 0.01.

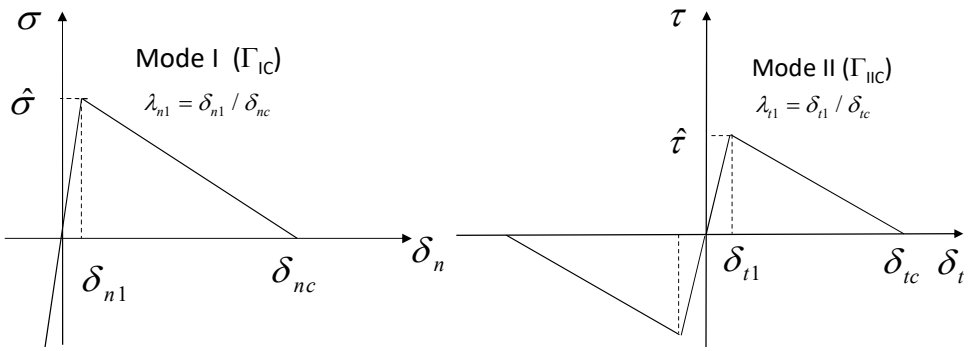

Figure 6.10 Shape of fracture laws for Mode I and Mode II

The fracture behavior of mortar was modeled with a triangular law in which maximum stress and area under the curve were known. In Mode II the fracture energy was taken from literature and the maximum stress was considered half of that in Mode I. In Table 6.IIIare summarized fracture parameters of mortar.

Table 6.III Mortar fracture parameters

Fracture Mode	σ [MPa]	δ_{n1}[mm]	δ_{nc}[mm]	τ [MPa]	δ_{t1}[mm]	δ_{tc}[mm]
Mode I	4	0.00025	0.025			
Mode II				2	0.002	0.2

Cohesive Laws for Mortar/Fabric Interface

The Mortar/fabric interface is modeled by a CZM with tri-linear laws, which was first proposed by Yang and colleagues (Yang et al. 2006)to describe those fracture processes with extrinsic toughening mechanisms, in addition to the intrinsic facture (Figure 6.11).

Since it has been well demonstrated that the most important feature of the mortar/fabric interface is the post-debonding friction (Carloni et al. 2014), these type of cohesive laws are well suited for such purposes.

Each mode is characterized by four parameters: the peak strength (i.e., σ_1 for mode I and τ_1 for mode II) and first critical displacement (i.e. δ_{n2} for mode I and δ_{t2} for mode II) describing the debonding process; the secondary strength (i.e. σ_2 for mode I and τ_2 for mode II) and the second critical displacement (i.e. δ_{nc} for mode I and δ_{tc} for mode II) describing the post-debonding friction.

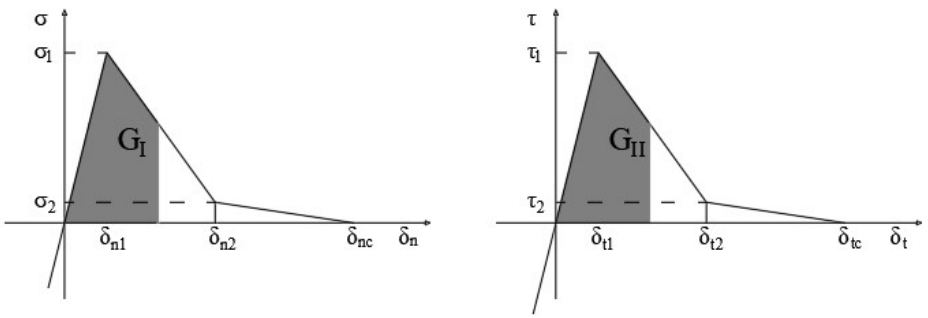

Figure 6.11 Cohesive traction-separation law

The cohesive law used to connect fabric to mortar is taken from literature (D'Antino et al. 2018) and modified in order to consider the ratio A_f/A_t. As shown in the Figure 6.6, The cohesive law was modified based on the ratio of fabric to total coupon area ($r_A=A_f/A_t=0.5$).

In particular, the cohesive law was modified multiplying the peak stress by the r_A. Resulting in the maximum strength being halved. The cohesive law is explained as a trilinear curve with a friction branch, as shown in Figure 6.12.

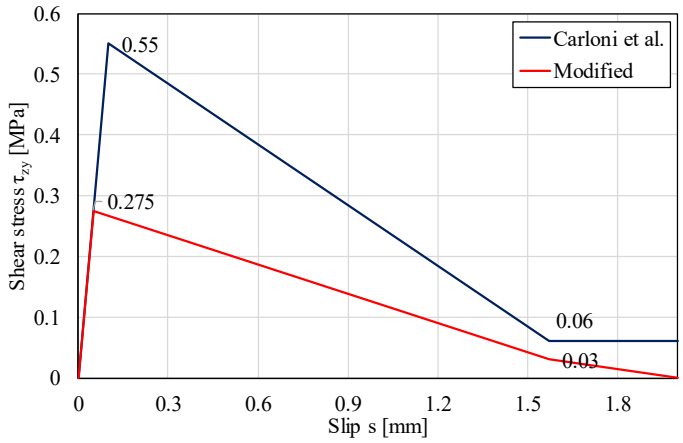

Figure 6.12 Cohesive laws

The cohesive law used to connect the two layers of mortar (link-cohesive elements) was taken from fracture law of mortar (Carloni et al. 2017a) (Table 6.III) and modified in order to consider the ratio A_m/A_t. For this reason, the maximum strength was halved. The cohesive law considered herein is also a trilinear curve.

In the A-FEM, the following parameters have to be defined:

- the number of cracks;
- the element in which the crack occurs (crack domain);
- the direction of crack propagation (cracks propagate strictly along the initial direction);
- the crack type (max principal stress criterion at any integration point), and the number of cracks.

Five cracks, equally spaced over the monitoring length, were defined in the presented model. A parametric study was carried out in order to evaluate the influence of number and location of the cracks, which is reported in the following section.

6.1.4 Numerical and experimental results of direct tensile

Results in terms of stress-strain curves (Figure 6.13), show the three branches of constitutive behavior of FRCM material.

- The first stage (uncracked) represented a situation in which both mortar and fabric are perfectly connected. With the occurrence of the first crack, which marked the end of the first stage and the

beginning of the second stage (transition), the stress in mortar is transferred to the fabric through cohesive elements and link-cohesive elements.

- In the second stage, the stiffness of the stress-strain curves is reduced drastically. Multiple cracks are formed, and strains (and consequently stresses) are redistributed by formation of each crack.
- The third stage (cracked) represented a situation where no newly formed cracks were formed, and the existing cracks opened up, or otherwise, the de-bonding at the fabric-matrix interface occurred.

The cracked stage was approximately linear until the failure happened due to complete de-bonding. Before failure, the fabric was under load and a significant amount of slippage at the fabric-mortar was observed.

Stress-strain (Figure 6.13) curve was evaluated from the model according to following rules:

- strain: taking the displacement of a control point and dividing it for monitoring length;
- stress: taking the total reaction force (N/mm) from output file and dividing it by the thickness of fabric.

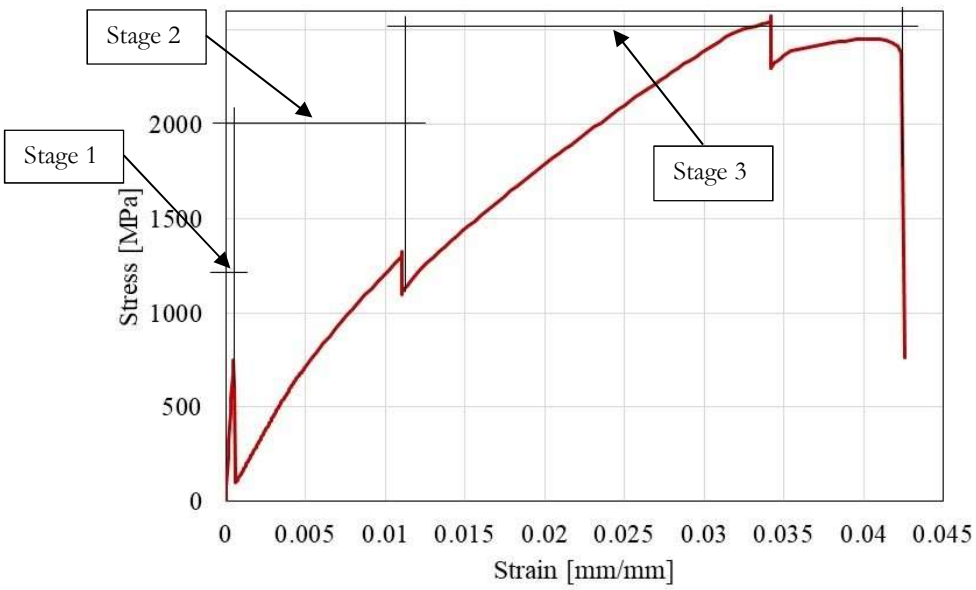

Figure 6.13 Numerical stress-strain curve

Experimental results

The results of PBO coupons (one, two and three layers of PBO fabric) tested per AC434 from the work of Pino (2016)were used to compare numerical and experimental results (Figure 6.14).The specimen geometry, boundary conditions, and loading were identical in all cases.

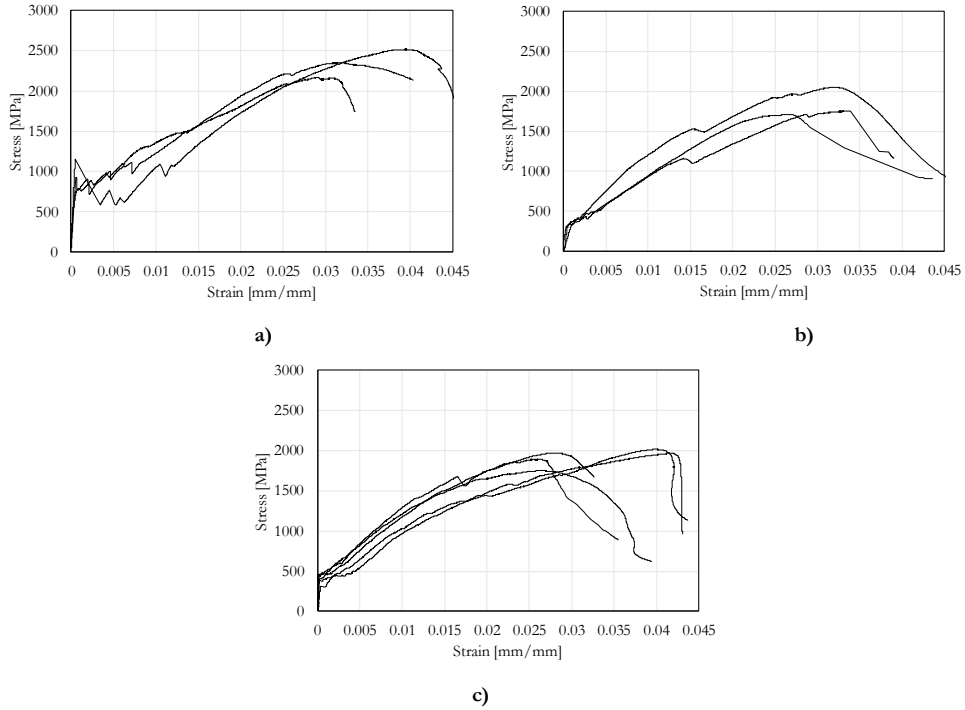

Figure 6.14 Experimental results: a) one layer, b) two layers, c) three layers

6.1.5 Parametric study and comparison

In this paragraph the parametric studies that were carried out in order to validate the model are presented. In particular, the influence of crack number was studied in order to find the right number of crack formation. Then the model with multiple layer of fabric was studied. Numerical results are compared to the experimental ones shown in Figure 6.14.

Influence of crack number

Since pre-cracks are defined in the A-FEM model, it is important to consider the effect of the number of cracks on the final results. During the first stage, in which uncracked mortar is perfectly linked to the fabric, there is no slippage at the fabric-matrix interface. When the first crack is arisen, stress in mortar is

transferred to the fabric through the cohesive elements and soon, after that fabric-matrix debonding starts, it is possible the redistribution of the stresses.

A parametric study was carried out in order to evaluate the influence of the number and location of cracks. In this parametric study, stress-strain curves were compared to that obtained from the experiments.

Five cracking configurations were tested in the model:

- 1 crack in the middle of monitoring length;
- 2 cracks (at the beginning and end of monitoring length);
- 3 cracks (one in the middle, one at the beginning and one at the end of monitoring length);
- 4 cracks (equally spaced over the monitoring length);
- 5 cracks (equally spaced over the monitoring length).

Results of parametric study showed that at least three cracks over the length of 100 mm were necessary for a good fit with experimental curve. After three cracks, adding more cracks had minor effects on the stress-strain curves, as shown in Figure 6.15.

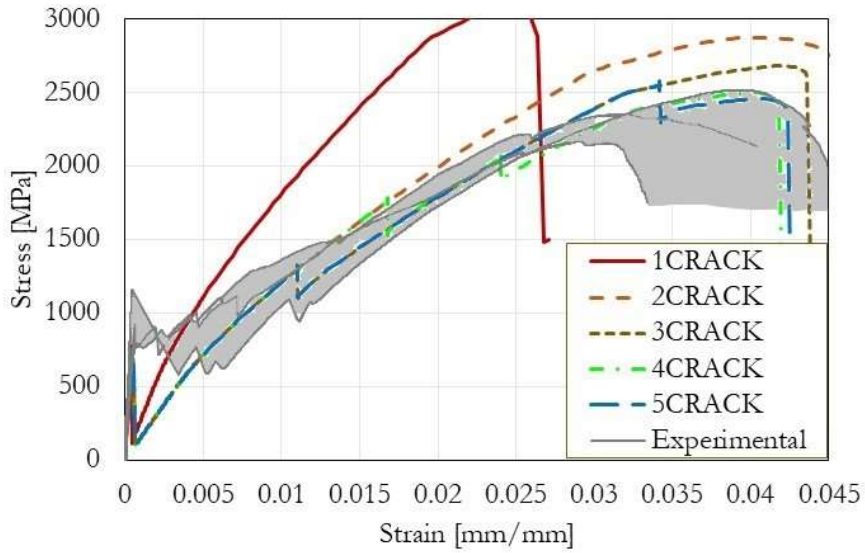

Figure 6.15 Comparison of stress-strain curves with different cracks number

A strong decrease of the load is observed in correspondence of formation of the first crack. This phenomenon is related to the limitation of a numerical model.

Multiple layers

Multiple layers of fabric were considered in order to validate the numerical model. The assumption and simplifications were identical to those of the one-layer model. A third and parties layer of mortar, 2 mm in thickness (in accordance with the experimental samples) was added between adjacent layers of fabric. Boundary condition and displacements applied were identical to those of the model with one layer of fabric.

Comparison and discussion

The numerical stress-strain curves were compared to the experimental ones as shown in Figure 6.16a) b) and c).

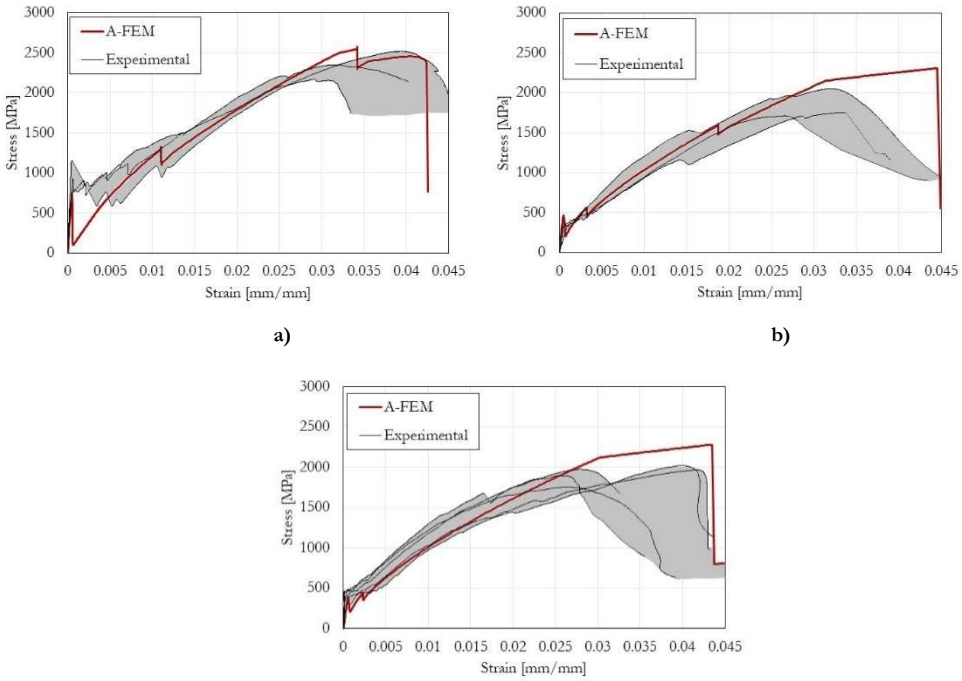

Figure 6.16 Comparison between experimental and numerical results (DT) – a) one ply model, b) two plies model, c) three plies model

Results, in terms of stress-strain curve, show that also for multiple fabric layers the model can satisfactorily predict the behavior of FRCM coupons under direct tension. The contribution of link-cohesive elements was of key importance because only using them, stress can be transferred from external layers of mortar to internal ones.

6.1.6 Single-lap shear test (SLS)

A different test set up was modeled with A-FEM and cohesive elements in order to demonstrate that this numerical approach is able to describe the FRCM behavior when bonded to a substrate. In this configuration, the fabric is pulled out from mortar matrix that is connected to a rigid block of concrete.

Experimental tests carried out by Sneed (Sneed et al. 2014) were conducted according to RILEM standard. With this test protocol, it is possible to study the six failure modes.

Geometry of specimens and boundary conditions are shown in Figure. The experimental results were taken from Carloni et al. 2017a. In this study, specimens with 330 mm bonded length and 60 mm fabric width were used.

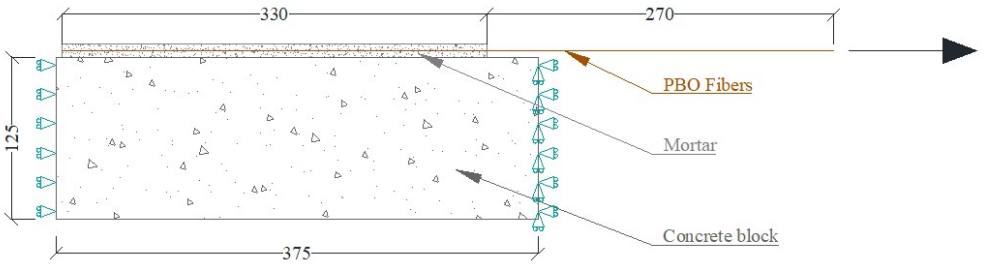

Figure 6.17 Geometry on Single-Lap Shear test specimen [mm]

Mechanical, fracture and cohesive properties used in this study were exactly the same of the direct tension test reported in Table 6.I, Table 6.II and Table 6.III

Mechanical and fracture properties of concrete were taken from literature (Carloni et al. 2017a) and are summarized in Table 6.IV.

Table 6.IV Mechanical and fracture properties of concrete block

Material	E [GPa]	υ	σ_c [MPa]	σ_t [MPa]	G_I[N/mm]	G_{II}[N/mm]
Concrete	34	0.2	42.5	3.4	0.05	0.2

6.1.7 Results of single-lap shear test model

Shear stress was evaluated from model and experiment taking the reaction force and dividing that by the equivalent thickness of the fabric ($n \times t^*$).A comparison between the numerical model and experimental results, in terms of stress vs. global slip curves, showed a good agreement (Figure 6.18). In particular, pre-peak and peak stress matched the experimental curves. After reaching the

peak stress, the model shows a total failure as result of some of the assumptions and simplifications.

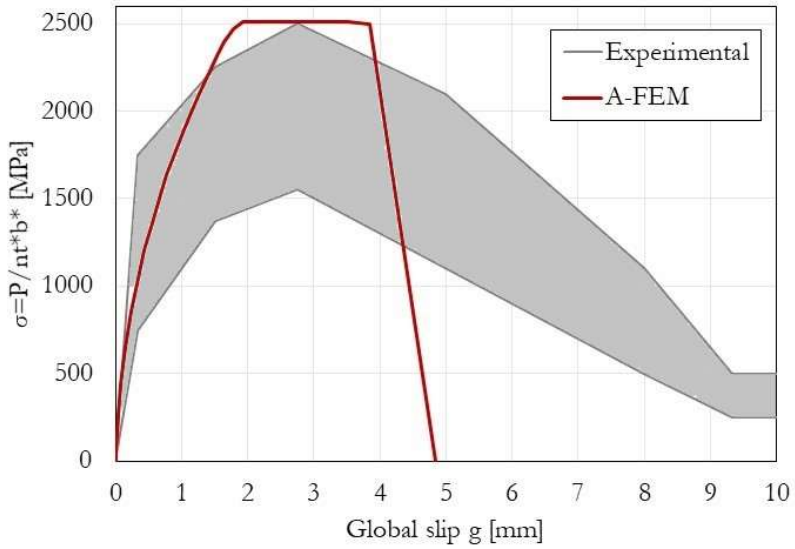

Figure 6.18 Comparison between 2D numerical and experimental results (SLS)

Many authors (D'Antino et al. 2014) studied the mechanism of bond in single-lap shear test. Figure 6.19 shows the bond mechanism. A comparison between theoretical behavior and numerical results was done to better understand the differences.

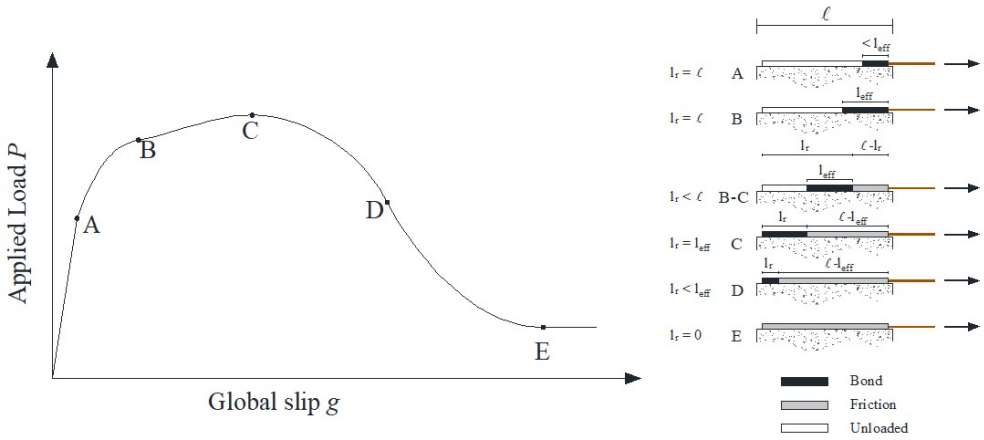

Figure 6.19 Theoretical curve that describe bond mechanism

The model carried out was able to catch the curve in Figure 6.19 up to the point C. After that point, the model was not able to catch the post-peak behavior

and an instantaneous failure occurred in the model. Figure 6.20 shows progressive evolution of bond length in the model.

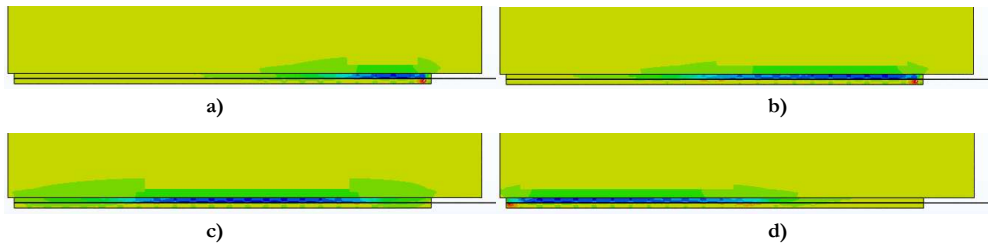

Figure 6.20 Evolution of bond length

Referred to Figure 6.19, Figure 6.20 can be explained:

a) develop of bond length up to point A;
b) increase of bond length up to point B;
c) transition of bond length up to point C;
d) achievement of point C and suddenly failure due to debonding of fabric from mortar matrix;

6.1.8 Conclusion

A numerical model for FRCM systems was developed using Augmented-FEM formulation. The A-FEM models were able to forecast the cracks formation and propagation in their domains defining few parameters related to the fracture behavior of each material.

Moreover, cohesive elements were used in order to describe the behavior at the interface between different materials. A new technique for modeling the mortar within fabric, defining "link-cohesive elements", was described. Two type of test set up were used: direct tension and single-lap shear test.

For direct tension, a parametric study was conducted on number of cracks and multiple layers of fabric. Results of these studies, in terms of stress-strain curves, have underlined a good agreement with the experimental ones including an ability to develop the three branches of a typical stress-strain curve of FRCM coupon tested per AC434. Only the last part of third branch presented some inconsistencies as affected by assumptions and simplifications of the 2D model.

For Single-Lap Shear again the model was able to develop stress-slip curves consistent with experiments, except for the post peak behavior.

At this point, new studies on 3D model, using 3D A-FEM, were done in order to better describe the constitutive behavior of FRCM. This new approach is discussed in the following section.

6.2 3D Finite Element model using Augmented-FEM

This study deals with the analysis of FRCM materials using 3D Augmented-Finite Element Method (A-FEM) approach (Naderi et al. 2016).

The tensile test on the FRCM (PBO fabric) coupon according to AC434 (2013) and single lap shear test on FRCM-concrete joint according to RILEM (2018) were numerically modelled and compared to the experimental stress-strain and stress-global slip curves.

The further aim of this study is to determine a proper A-FEM 3D model of the FRCM to be used in the structural analysis in order to optimize the system with different fabric material, different mortar strength and different geometry configuration.

6.2.1 Introduction

As consequence of results found in the previous study on 2D models, a new approach is discussed in this section. In fact, 3D models for FRCM strengthening system were studied and presented in this section.

Direct tensile test on FRCM coupon with PBO fabric according to AC434 was modelled. At the beginning of the modelling phase, some assumptions and simplifications were done; the latter were different from those of 2D models, in order to represent, as much as possible, the effective behavior.3D tetrahedron A-F Elements were used and their geometry is discussed in the following.

New cohesive laws were calibrated in order to catch experimental results and then, through parametric studies on the influence of single point of cohesive law (first stiffness, maximum strength, second stiffness and last displacement), they were validated by applying them in a model with different test setup.

Single Lap Shear test on FRCM-concrete joint was modelled and, also in this case, results present a good agreement with the experimental ones, in terms of stress-global slip curves.

6.2.2 Assumptions and simplifications

3D models were created using A-FEM formulation and cohesive elements (elements with 8 nodes). The coupon geometry for both boundary conditions is consistent with that of the AC434 (2013). Two layers of mortar (5 mm thickness) and one layer of PBO fabric were modelled and connected by zero-thickness cohesive elements (see Figure 6.21).

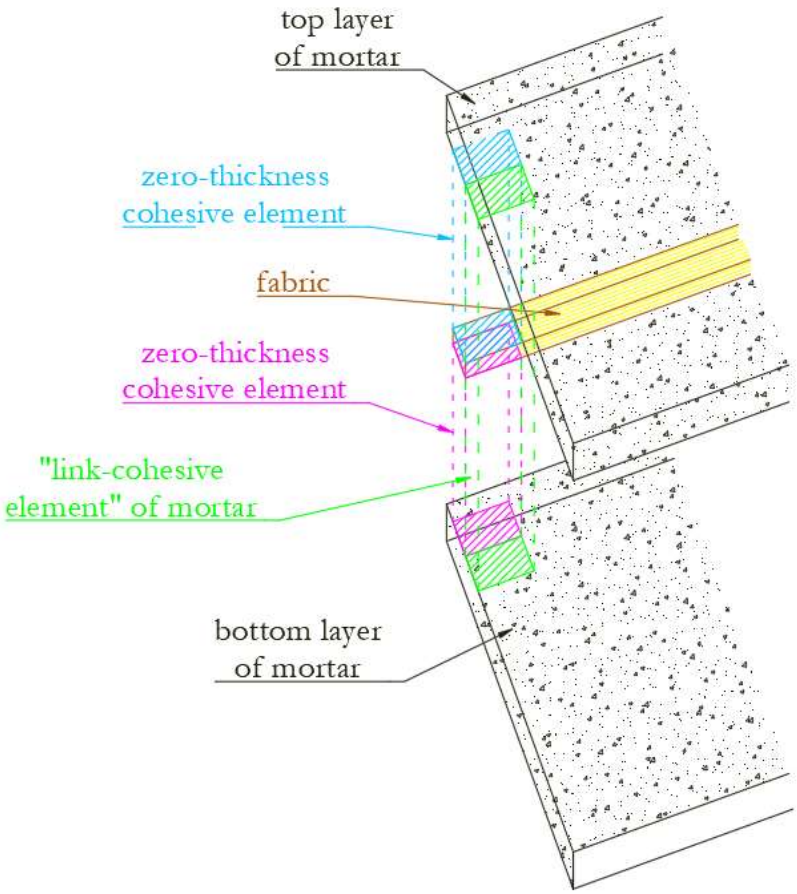

Figure 6.21 Schematic representation of elements of the models

The following assumptions were done:

i. the two layers of mortar were identical;
ii. only the contribution of the longitudinal yarns of the fabric were modeled and transversal yarns were neglected;
iii. the mortar within the fabric openings was modeled with "link-cohesive elements" in order to connect the two layers of mortar and provide stress transfer between the mortar layers;
iv. the connection between layer of mortar and layer of fabric was modelled with "zero-thickness cohesive elements".

The cohesive law between mortar and fabric was investigated through a parametric study and a new cohesive law was calibrated and discussed in following sections.

3D Tetrahedron A-FEs

In this study,3D tetrahedron A-FEs were used (Figure 6.22). The geometry was reproduced defining tetrahedron elements in order to build a brick element as shown in Figure 6.23. This procedure allowed to better manage every single node and element of the model.

For a faster definition of elements, a new algorithm was developed. Nodes of a single element must be defined following the right-hand rule. Six tetrahedron elements are needed for building a brick element. For example, to reproduce the brick element in Figure 6.23 the six tetrahedron elements are:

1. A – D – C – G;
2. A – D – F – E;
3. D – G – E – H;
4. A – B – D – E;
5. B – D – E – H;
6. B – H – E – F.

By the algorithm these combinations were reproduced in order to define the model geometry.

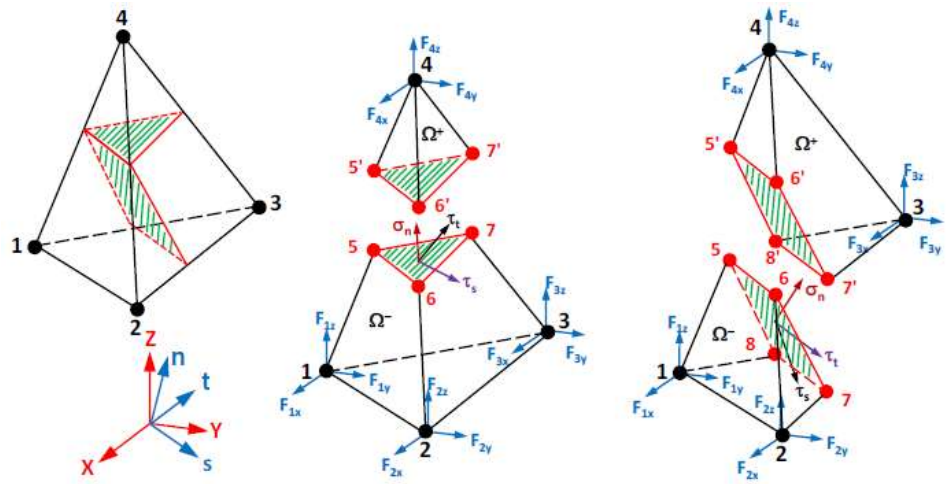

(a) (b) (c)

Figure 6.22 Element illustration for (a) a regular 4-node tetrahedron element with two possible different crack planes; (b) an A-FE with a tetrahedron and a wedge sub-domains; (c) an A-FE with two wedge sub-domains.

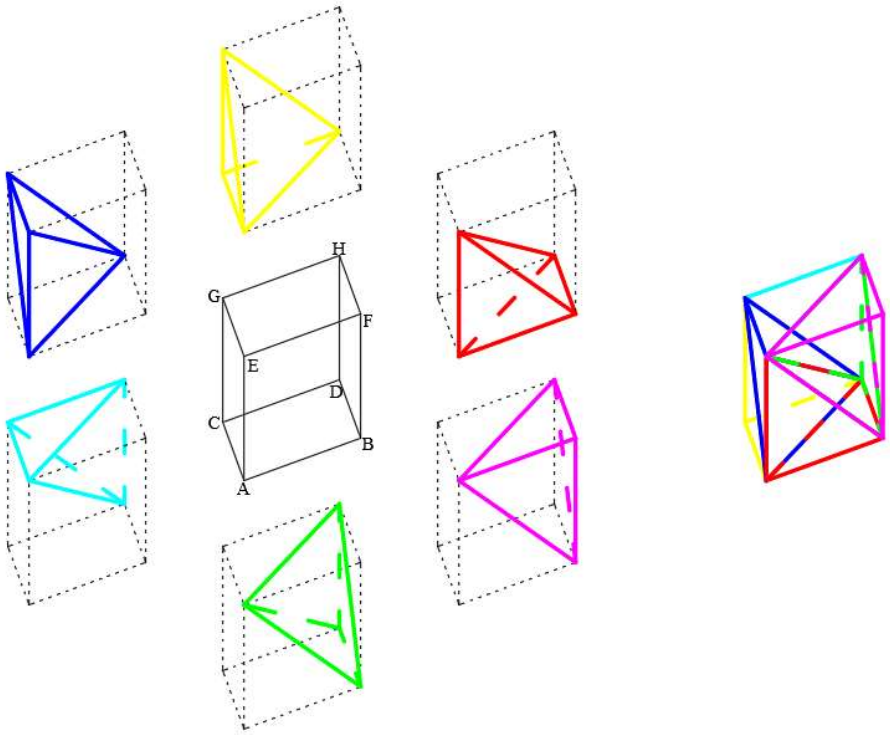

Figure 6.23 Building of a brick element through six tetrahedron elements

In the following Figures (Figure 6.24 , Figure 6.25 and Figure 6.26) some parts of the model are shown. Geometry sizes are the same of 2D model according to AC434, with a width of 50 mm and 5 yarns of fabric. In Figure 6.25 the fabric configuration without transversal fibers is shown; 8 nodes A-Fes were used.

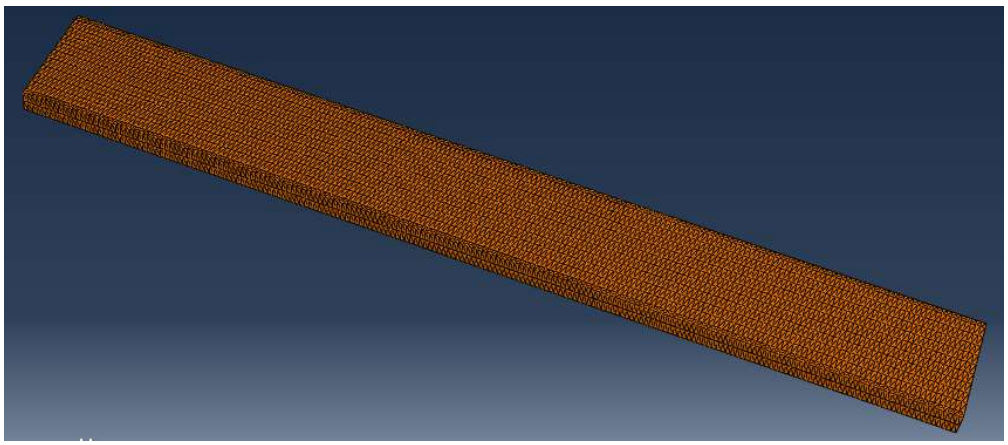

Figure 6.24 Mortar layers

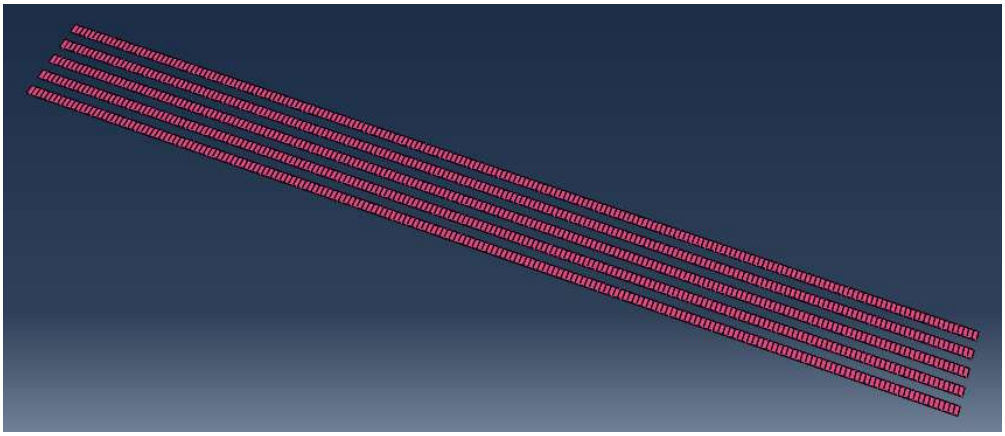

Figure 6.25 Fabric yarns

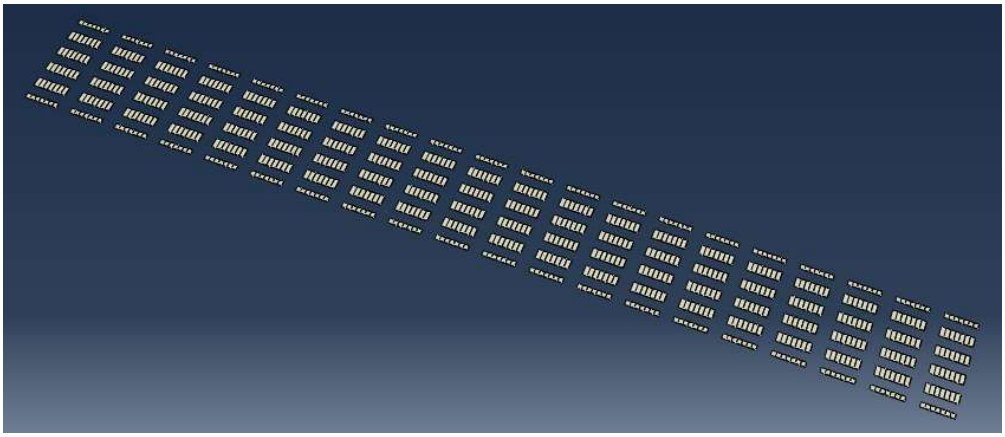

Figure 6.26 "Link-cohesive elements"

Boundary conditions and applied displacements

The boundary conditions were the same of the 2D model previously explained. The latter were applied on the external nodes of the bottom and upper mortar layers, for the first 150 mm, in order to simulate the steel tabs. In those nodes, the displacements in directions x-y-z were restrained.

Uniform displacement was applied on the external nodes of the bottom and upper mortar layers, for the end 150 mm in order to simulate the displacement applied by the use of steel tabs and clevis grips per AC434.

Materials

Material mechanical properties of PBO fabric and mortar were taken from data sheet and summarized in the Table 6.I.Fracture parameters for the mortar were taken from Carloni's studies (Carloni et al. 2017a) and summarized in Table 6.II.

Cohesive law for mortar fracture

As previously mentioned, the fracture process in A-FEs was modelled with a CZM with triangular traction-separation laws, as illustrated in Figure 6.27. This simple CZM has been used to model mortar fracture successfully in many studies in literature (Liu et al. 2013 and 2014, Moës & Belytschko 2002).

For each pure fracture mode, three CZM parameters are needed:

i. the cohesive strength for mode I ($\hat{\sigma}$), mode II ($\hat{\tau}_s$) and mode III ($\hat{\tau}_t$);
ii. the critical displacements for mode I (δ_{nc}), mode II (δ_{tc}) and mode III (δ_{sc});
iii. the ratio of elastic-limit displacement (δ_{n1}, δ_{t1} and δ_{s1}) to the respective critical displacement: λ_{n1} for mode I, λ_{t1} for mode II and λ_{s1} for mode III.

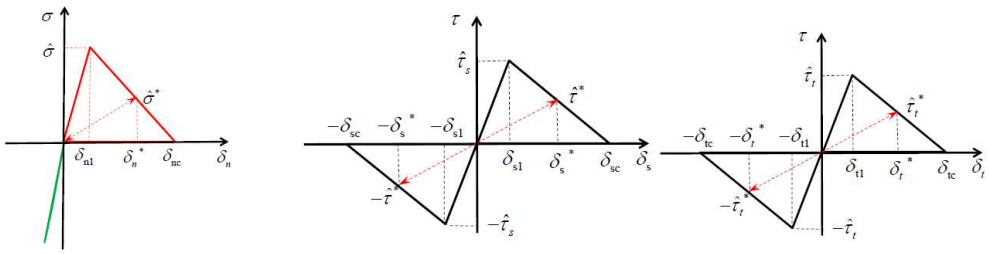

(a) **(b)** **(c)**

Figure 6.27 Cohesive laws for (a) (matrix) shear damage mode; (b) fiber tensile rupture/compressive kinking damage mode; (c) matrix tension/compression damage mode.

The fracture behavior of mortar was modeled with a triangular law in which maximum stress and area under the curve were known. In mode II and mode III the fracture energy was taken from literature and the maximum stress was considered half of that in Mode I. In Table 6.III fracture parameters of mortar are summarized.

Cracks definition

The 3D tetrahedron A-FEs allow free crack initiation or crack initiation in designated elements. To designate particular elements for crack initiation, the ABAQUS "UEL PROPERTY" data input deck in an ABAQUS input file can be used. In this case, the user needs to group all elements intended for crack initiation into an individual element set ("ELSET" in ABAQUS).

In this study pre-crack elements were defined and multiple elements were selected but results have shown that not all of them have cracked.

6.2.3 Calibration of a new cohesive law

After the definition of geometric and mechanical properties of the model, an important phase of this study was to understand the best cohesive law (fabric-mortar) to be used. As previously done for the 2D model, the cohesive law proposed by D'Antino (D'Antino et al. 2018) was considered (see Figure 6.28). Direct tensile test on coupon was the first modelled test setup.

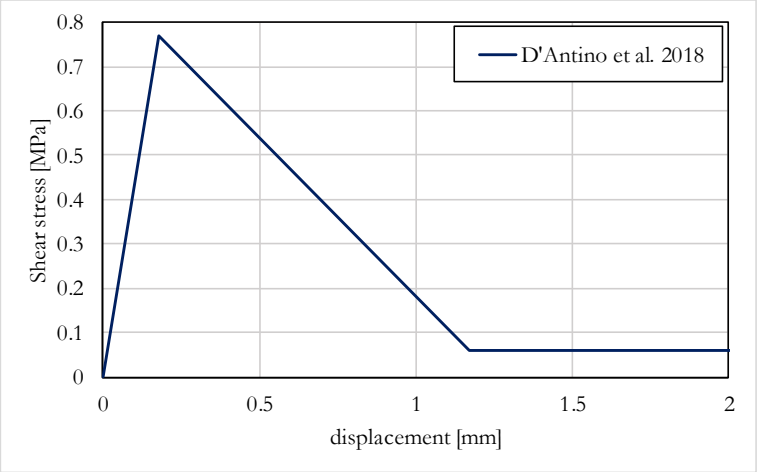

Figure 6.28 Cohesive law proposed by D'Antino et al. (2018)

In the previous cohesive law, the only difference with the modelled one consists on the last point of third branch, which had to be set equal to zero, according to the A-FEM code for cohesive elements.

From the comparison with experimental results, shown in Figure 6.29, a relevant difference in the third branch of the stress/displacement curve was observed.

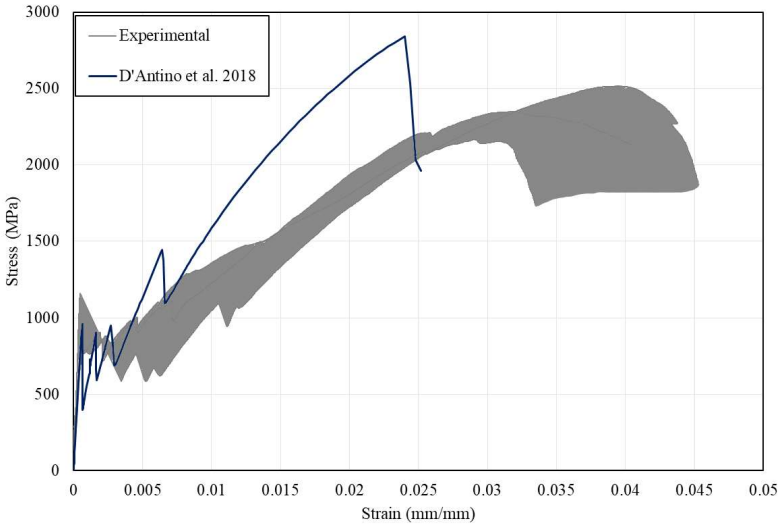

Figure 6.29 Comparison between numerical and experimental results (DT)

Numerical results were affected by assumptions and simplifications of this model and for this reason a new cohesive law was calibrated. The conducted parametric studies are following discussed.

Parametric study

Parametric studies were conducted in order to find the best combination of the different parameters. In Figure 6.30, Figure 6.32 and Figure 6.34, the investigated cohesive laws are shown. The latter are three-linear laws, as the implemented formulation in 2D models. The first investigated parameter in parametric studies was the stiffness of the first branch of the cohesive law. A shear stress was selected ($\tau_{s1} = 0.6$ [MPa]) and six different stiffnesses were defined:

- $k_1 = 0.50$;
- $k_1 = 0.55$;
- $k_1 = 0.60$;
- $k_1 = 0.65$;
- $k_1 = 0.70$;
- $k_1 = 0.75$;

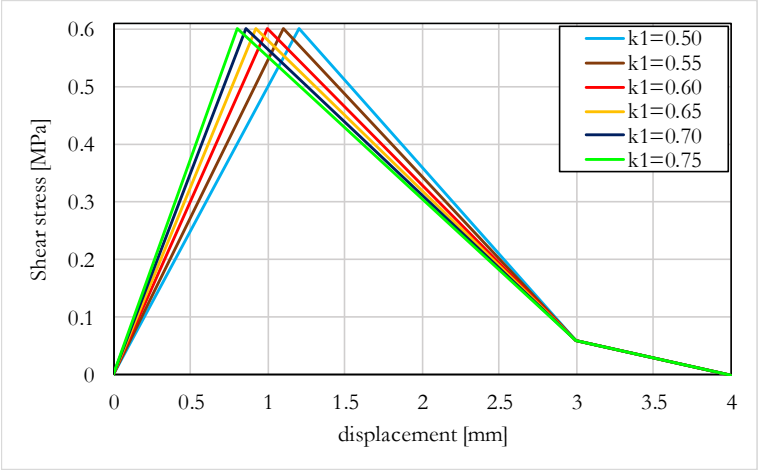

Figure 6.30 Cohesive laws with τ=0.6 - parametric study on the stiffness of the first branch (k_1)

Stress-strain (Figure 6.31) curves were evaluated from the model according to the following rules:

- strain: taking the displacement of a control point and dividing it for monitoring length;
- stress: $\sigma = \frac{F}{t^* b}$, where:
  - F is the total reaction force (N);
  - t^* is the equivalent thickness of fabric (0.0455 mm);
  - b is the specimen width (50 mm).

The comparison with experimental results are show in Figure 6.31.

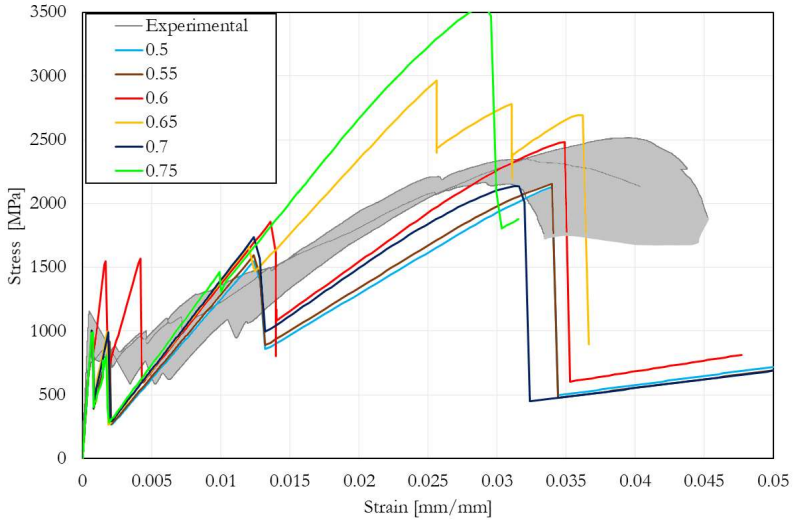

Figure 6.31 Comparison between numerical and experimental results (DT), first parametric study (τ=0.6)

The numerical results evidenced that increasing the stiffness, starting from 0.5, leads to a better fitting for $\tau_{s1} = 0.6$ [MPa], over this value the stresses are too high, with respect to experimental one. It is worth noticing that this last factor has an influence in the starting of the crack, so that, at varying from 0.6 to 0.7 the curve doesn't show the load decay at the strain 0.015 [mm/mm], and at a further increasing of the stiffness to 0.7 the load decay appears again. Then, four stiffnesses were selected (k_1 = 0.5;0.55;0.6;0.65), as shown in Figure 6.32 and Figure 6.34, and other two different shear stresses ($\tau_{s1} = 0.5 \div 0.7$ [MPa]) were chosen. Numerical results were evaluated and compared with the experimental ones (see Figure 6.33 and Figure 6.35).

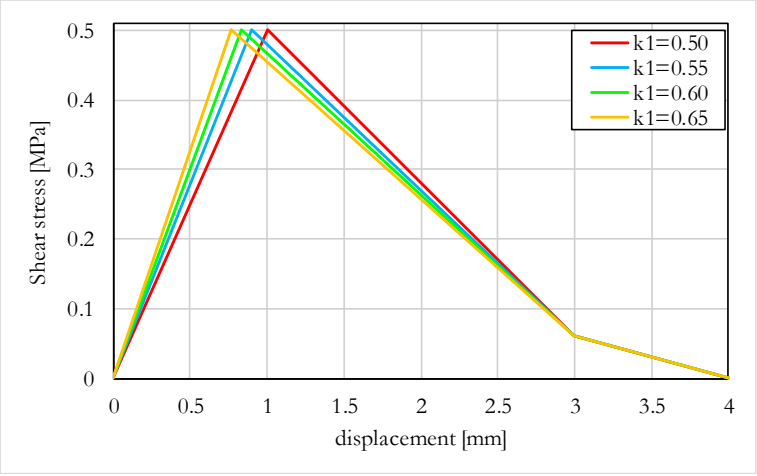

Figure 6.32 Cohesive laws with τ=0.5 - parametric study on the stiffness of the first branch

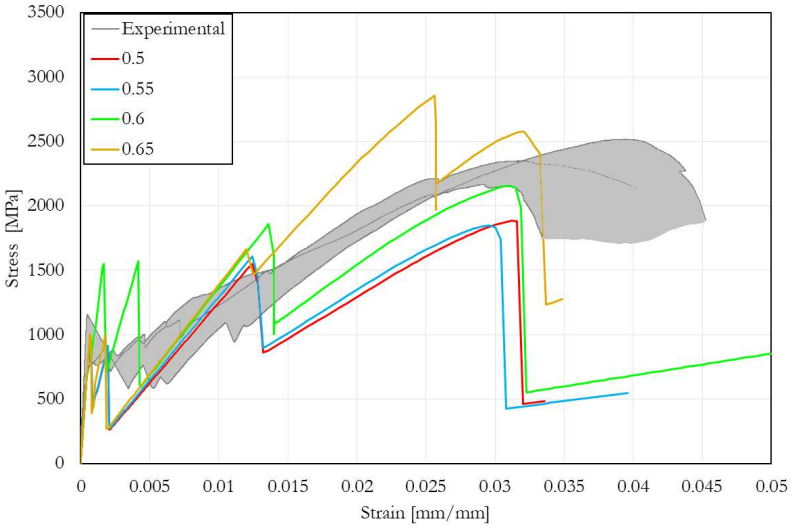

Figure 6.33 Comparison between numerical and experimental results (DT), second parametric study (τ_1=0.5)

From comparison of numerical results with the experimental ones is revealed a correlation between first stiffness k_1 and τ_{s1}. Therefore, a combined optimization of the two parameters is necessary.

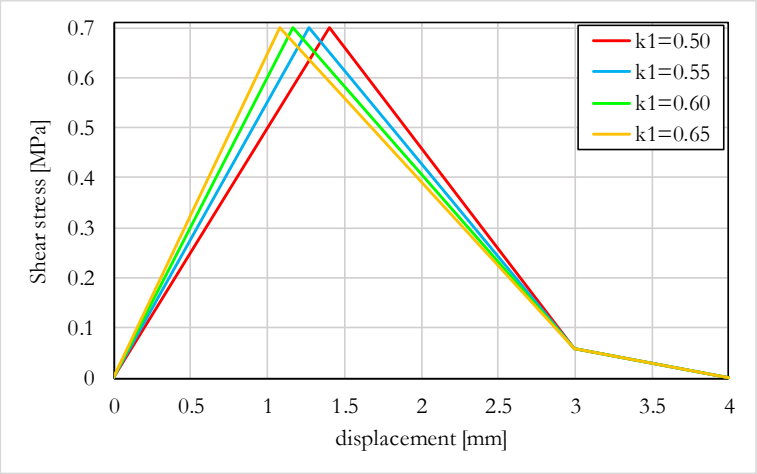

Figure 6.34 Cohesive laws with τ_1=0.7 - parametric study on the stiffness of the first branch

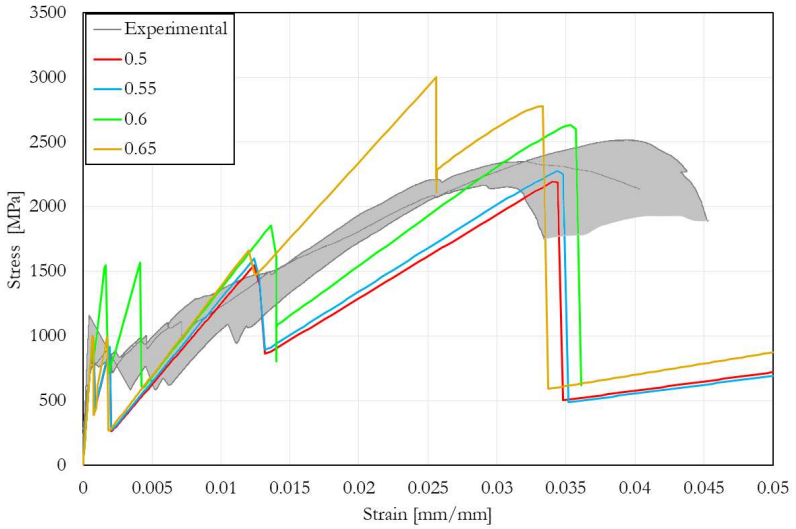

Figure 6.35 Comparison between numerical and experimental results (DT), third parametric study (τ_1=0.7)

The further parameter investigated is the second point of the cohesive law, related to the friction branch. The selected shear stress was $\tau_{s2} = 0.06\ [\text{MPa}]$, associated with three different displacements as shown in Figure 6.36.

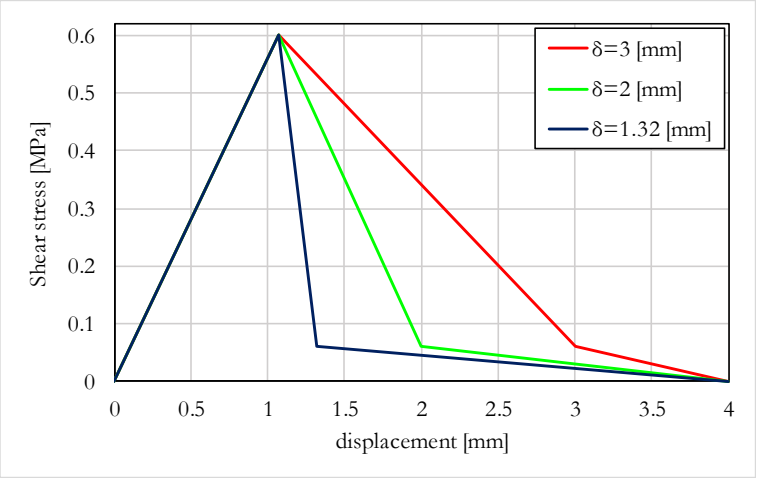

Figure 6.36 Cohesive laws with τ_1=0.6 and τ_2=0.06 - parametric study on the stiffness of the second branch

In Figure 6.37 the comparison with the experimental results is shown; in this figure the influence of the displacement, related to second point of cohesive law, is evident.

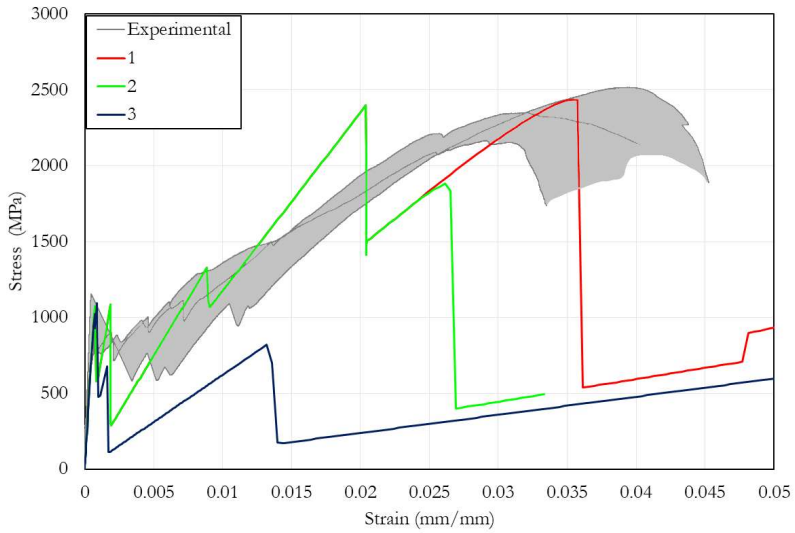

Figure 6.37 Comparison between numerical and experimental results (DT), third parametric study (τ_1=0.6)

In order to investigate the influence of the τ_{s1} value on the numerical results, three different cohesive laws (see Figure 6.38), with same stiffness and different shear cohesive stress, have been modelled. The comparison of the corresponding obtained results is shown in Figure 6.39.

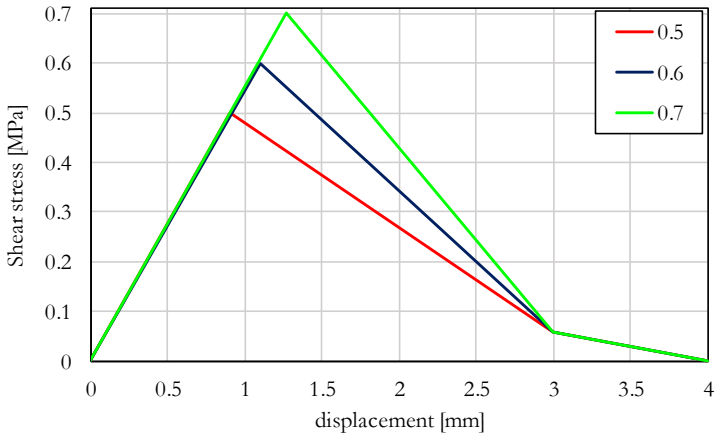

Figure 6.38 Comparison between three different cohesive laws with fixed first branch stiffness and varying τ_1 (0.5, 0.6 and 0.7)

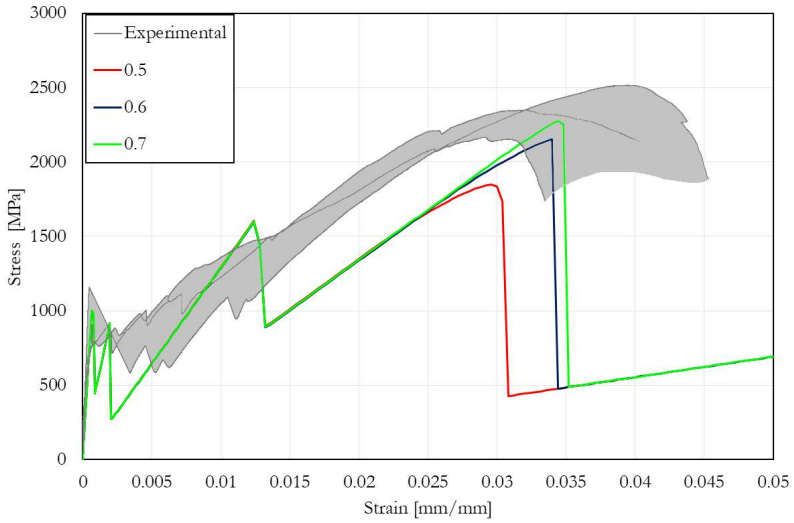

Figure 6.39 Comparison between numerical and experimental results (DT), (τ_1=0.5, 0.6 and 0.7),

In this case, since the stiffness was constant, the numerical curves have the same slope but different elongation before failure. This seems to show the independence of the two parameters investigated.

6.2.4 Comparison with experimental results (SLS)

As previously done for the 2D studied models, in this section, through the obtained results of the cohesive law, a different 3D test set up was modeled with A-FEM (see Figure 6.40) and cohesive elements in order to demonstrate that this numerical approach is able to describe the FRCM behavior when bonded to a

concrete substrate. In this configuration, the fabric is pulled out from mortar matrix that is connected to a rigid block of concrete, as shown in Figure 6.17.

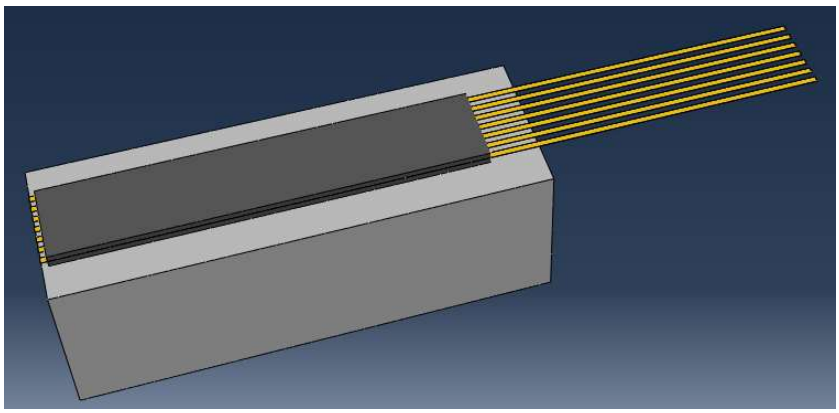

Figure 6.40 A-FEM configuration of the SLS test set up

Among the previous studied cohesive laws, the parameters of the selected one are: $\tau_{s1} = 0.6\left(MPa\right)$ and $k_1 = 0.55\left(N/mm\right)$. The obtained results, in terms of stress-global slip curve, are shown in Figure 6.41.

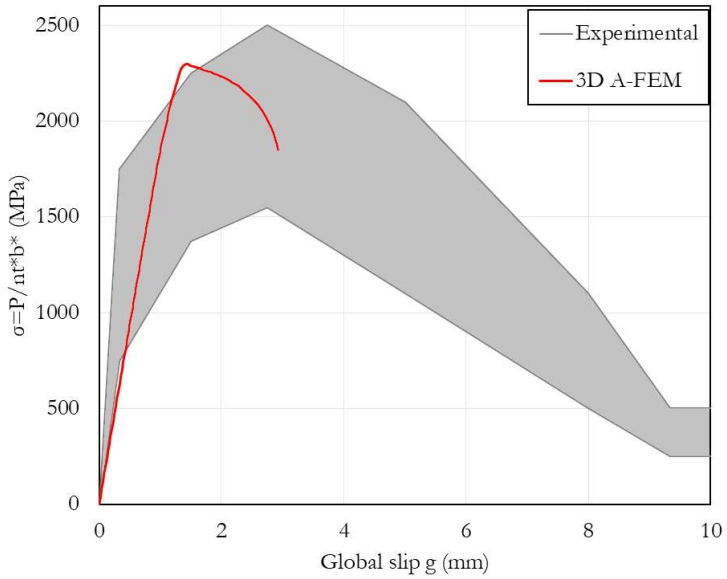

Figure 6.41 Comparison between 3D numerical and experimental results (SLS)

As shown for the 2D model, from the previous figure it can be highlighted the effectiveness of the proposed approach. In fact, the numerical results are contained within the experimental ones up to peak load. The post peak behavior, also for this approach, is affected by assumptions and simplifications.

Evolution of bond length

By opportunely hiding the top layer of mortar, it is possible to discuss the evolution of stress transfer between fabric and mortar and consequently, to highlight the evolution of bond length.

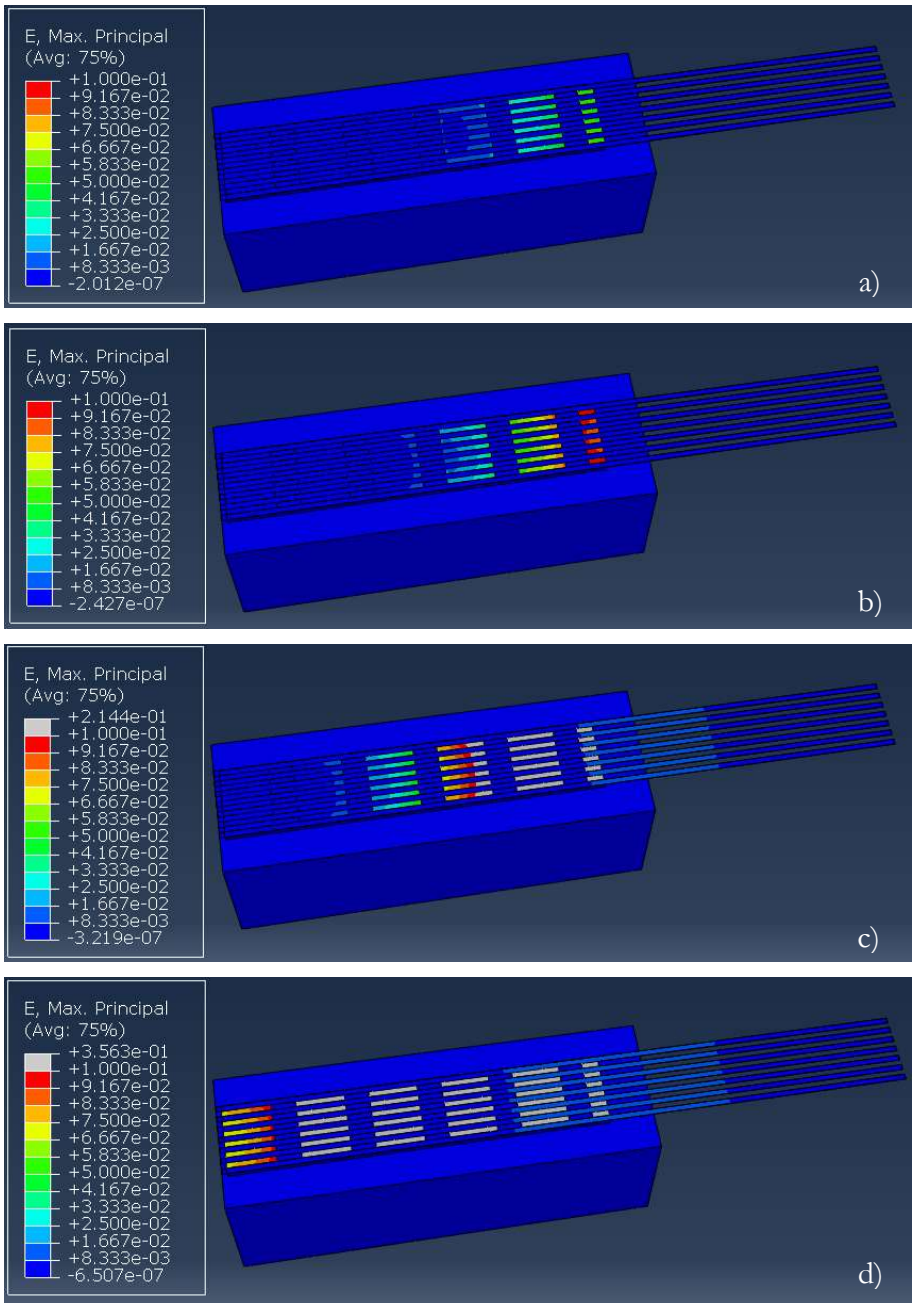

Figure 6.42 Evolution of bond length

Referred to the theoretical curve shown in Figure 6.19, Figure 6.42 can be explained:

a) develop of bond length up to point A;
b) increase of bond length up to point B;
c) transition of bond length up to point C;
d) achievement of point C and suddenly failure due to debonding of fabric from mortar matrix;

6.2.5 Discussion and conclusion

In this work a 3D new numerical model for FRCM systems was developed using Augmented-FEM formulation. The A-FEM models were able to allow cracks formation and propagation in their domains defining few parameters related to the fracture behavior of each material. Two type of test set up were modelled: direct tension and single-lap shear test.

For the direct tension, a parametric study was conducted on cohesive law in order to connect fabric and mortar. Results, in terms of stress-strain curves, have underlined a good agreement with the experimental ones.

For Single-Lap Shear again the model was able to develop stress-slip curves consistent with experiments, except for the post peak behavior. A discussion on evolution of bond length have highlighted the good agreement with the theoretical curve.

Conclusions

The mechanism of stress transfer across different materials bonded each other was the main topic investigated in the present PhD. thesis. Into this framework experimental campaigns were performed and numerical models were developed in order to describe this phenomenon.

After a short overview of the adhesives problem in Chapter 1, in Chapter 2 the attention was focused on adhesive joints for mechanical application in which aluminum, GFRP and glass materials were joined each other. Two experimental campaigns were performed, in order to evaluate the mechanical performances of double-lap joints using different type of adhesives and adherents at high test temperatures. The strong influence of temperature on mechanical behavior of adhesive joint was demonstrated. This phenomenon is strictly connected to glass transition temperature of epoxy adhesives used.

In a third experimental campaign, the mechanical characterization of adhesive with tensile tests on dog-bone specimens was performed and the same temperature effects were observed. In particular, results showed a mutation of constitutive behavior, from an elastoplastic (softening) at environmental temperature, to an elastoplastic (hardening) at 50°C, and an elastic brittle behavior at 80°C.

In Chapter 3, the mechanical performance of the adhesive joints in a steel-glass connection was investigated. The applicability of the adhesive bonds on a tensegrity floor was studied, performing experimental tests on hybrid system with a stepwise cyclic loading. A numerical model was also developed in order to validate test results and the comparison showed a good agreement in terms of displacement of control points.

The second part of the present dissertation was focused on new strengthening systems for civil application with composite materials, FRP and FRCM.

Externally bonded composite materials, FRP and FRCM, were introduced in Chapter4 and investigated in Chapters 5 and 6. In details, an experimental campaign on strengthened beams with FRP (carbon sheet fibers) and FRCM (PBO fabric) applied at different environmental conditions was conducted in order to study the durability problem. Results of this study showed the strong

effect of temperature, combined with moisture, on FRP system. On the contrary, FRCM performances resulted independent from these parameters.

Furthermore, experimental results, in term of load-displacement curves, were elaborated through an analytical procedure and an indirect method to evaluate the stress-slip curve was developed. This procedure allowed a comparison with results from alternative single-lap shear tests which are more widely used in literature.

Finally, in the Chapter 6, numerical models on FRCM system were carried out in order to develop a tool that could allow the optimization of the composite system. Augmented-FEM were implemented in numerical codes and used for 2D and 3D models. Tensile behavior of FRCM coupon was numerically simulated in all three stages of its characteristic behavior. Results of 2D simulations showed a good agreement with experimental results and validated by modelling a different test setup (SLS test).

About the 3D model, due to the different assumptions and simplifications of the model it was necessary to develop a new cohesive law, calibrated on experimental results. Parametric studies were conducted and new cohesive laws were proposed. Finally, the proposed approach was validated by modeling single-lap shear test and also in 3D models a good matching with experimental results was observed.

Bibliography

ABAQUS User's Manual, V. (2008). Version 6-7.

AC434, I. C. C. (2013). Acceptance criteria for masonry and concrete strengthening using fiber-reinforced cementitious matrix (FRCM) composite systems. *ICC-Evaluation Service, Whittier, CA*.

Al-Rousan, R., Issa, M., & Shabila, H. (2012). Performance of reinforced concrete slabs strengthened with different types and configurations of CFRP. *Composites Part B: Engineering*, *43*(2), 510-521.

Al-Samhan, A., & Darwish, S. M. (2005). Factors influencing thermo-mechanical stresses developed in bonded tools. *International journal of adhesion and adhesives*, *25*(5), 379-388.

American Concrete Institute (ACI.) (2008). Guide for the design and construction of externally bonded FRP systems for strengthening concrete structures. ACI 440.2R-08, Farmington Hills, Mich.

American Concrete Institute (ACI.) (2013) Guide to Design and Construction of Externally Bonded Fabric-Reinforced Cementitious Matrix (FRCM) Systems for Repair and Strengthening Concrete and Masonry Structures, ACI549.4R-13, Farmington Hills, Mich.

Apalak, M. K., Apalak, Z. G., Gunes, R., & Karakas, E. S. (2003). Steady-state thermal and geometrical non-linear stress analysis of an adhesively bonded tee joint with double support. *International journal of adhesion and adhesives*, *23*(2), 115-130.

Appelfeld, D., Hansen, C. S., & Svendsen, S. (2010). Development of a slim window frame made of glass fibre reinforced polyester. *Energy and Buildings*, *42*(10), 1918-1925.

ASTM D3528-96(2016), Standard Test Method for Strength Properties of Double Lap Shear Adhesive Joints by Tension Loading, ASTM International, West Conshohocken, PA, 2016, www.astm.org

ASTM D5573-99(2019), Standard Practice for Classifying Failure Modes in Fiber-Reinforced-Plastic (FRP) Joints, ASTM International, West Conshohocken, PA, 2019, www.astm.org

ASTM D638-14, Standard Test Method for Tensile Properties of Plastics, ASTM International, West Conshohocken, PA, 2014, www.astm.org

ASTM D7958 / D7958M-17, Standard Test Method for Evaluation of Performance for FRP Composite Bonded to Concrete Substrate using Beam Test, ASTM International, West Conshohocken, PA, 2017, www.astm.org

Bati, S. B., Fagone, M., & Ranocchiai, G. (2009). Analysis of the post-crack behaviour of a laminated glass beam. *Glass Performance Days 2009*, 349-352.

Bencardino, F., Carloni, C., Condello, A., Focacci, F., Napoli, A., & Realfonzo, R. (2018). Flexural behaviour of RC members strengthened with FRCM: State-of-the-art and predictive formulas. *Composites Part B: Engineering*, *148*, 132-148.

Biolzi, L., Cattaneo, S., & Rosati, G. (2010). Progressive damage and fracture of laminated glass beams. *Construction and Building Materials*, *24*(4), 577-584.

Borowicz, D. T., & Bank, L. C. (2010). Behavior of pultruded fiber-reinforced polymer beams subjected to concentrated loads in the plane of the web. *Journal of Composites for Construction*, *15*(2), 229-238.

BS EN 12390-3:2009 Testing hardened concrete. Compressive strength of test specimens.

Carloni, C., D'Antino, T., Sneed, L. H., & Pellegrino, C. (2014). Role of the matrix layers in the stress-transfer mechanism of FRCM composites bonded to a concrete substrate. *Journal of Engineering Mechanics*, *141*(6), 04014165.

Carloni, C., D'Antino, T., Sneed, L. H., & Pellegrino, C. (2017a). Three-dimensional numerical modeling of single-lap direct shear tests of FRCM-concrete joints using a cohesive damaged contact approach. *Journal of Composites for Construction*, *22*(1), 04017048.

Carloni, C., Santandrea, M., & Imohamed, I. A. O. (2017b). Determination of the interfacial properties of SRP strips bonded to concrete and comparison between single-lap and notched beam tests. *Engineering Fracture Mechanics*, *186*, 80-104.

Carloni, C., Santandrea, M., & Wendner, R. (2017c). An investigation on the "width and size effect" in the evaluation of the fracture energy of concrete. *Procedia Structural Integrity*, *3*, 450-458.

Ceroni, F., Bonati, A., Galimberti, V., & Occhiuzzi, A. (2017). Effects of Environmental Conditioning on the Bond Behavior of FRP and FRCM Systems Applied to Concrete Elements. *Journal of Engineering Mechanics*, *144*(1), 04017144.

Colajanni, P., De Domenico, F., Recupero, A., & Spinella, N. (2014a). Concrete columns confined with fibre reinforced cementitious mortars: experimentation and modelling. *Construction and Building Materials*, *52*, 375-384.

Colajanni, P., Fossetti, M., & Macaluso, G. (2014b). Effects of confinement level, cross-section shape and corner radius on the cyclic behavior of CFRCM confined concrete columns. *Construction and Building Materials*, *55*, 379-389.

Colombi, P., & D'Antino, T. (2019). Analytical assessment of the stress-transfer mechanism in FRCM composites. *Composite Structures*, *220*, 961-970.

D'Ambrisi, A., Feo, L., & Focacci, F. (2013). Experimental analysis on bond between PBO-FRCM strengthening materials and concrete. *Composites Part B: Engineering*, *44*(1), 524-532.

D'Antino, T., & Papanicolaou, C. (2017). Mechanical characterization of textile reinforced inorganic-matrix composites. *Composites Part B: Engineering*, *127*, 78-91.

D'Antino, T., Carloni, C., Sneed, L. H., & Pellegrino, C. (2014). Matrix–fiber bond behavior in PBO FRCM composites: A fracture mechanics approach. *Engineering Fracture Mechanics*, *117*, 94-111.

D'Antino, T., Colombi, P., Carloni, C., & Sneed, L. H. (2018). Estimation of a matrix-fiber interface cohesive material law in FRCM-concrete joints. *Composite Structures*, *193*, 103-112.

D'Antino, T., Pellegrino, C., Carloni, C., Sneed, L. H., & Giacomin, G. (2015b). Experimental analysis of the bond behavior of glass, carbon, and steel FRCM composites. In *Key engineering materials* (Vol. 624, pp. 371-378). Trans Tech Publications.

D'Antino, T., Sneed, L. H., Carloni, C., & Pellegrino, C. (2015a). Influence of the substrate characteristics on the bond behavior of PBO FRCM-concrete joints. *Construction and building Materials*, *101*, 838-850.

D'Antino, T., Sneed, L. H., Carloni, C., & Pellegrino, C. (2016). Effect of the inherent eccentricity in single-lap direct-shear tests of PBO FRCM-concrete joints. *Composite Structures*, *142*, 117-129.

Da Silva, L. F. M. (2010). Improving bonding at high and low temperatures. In *Advances in Structural Adhesive Bonding* (pp. 516-546). Woodhead Publishing.

Da Silva, L. F., Adams, R. D., & Gibbs, M. (2004). Manufacture of adhesive joints and bulk specimens with high-temperature adhesives. *International journal of adhesion and adhesives*, *24*(1), 69-83.

de Castro, J., & Keller, T. (2008a). Ductile double-lap joints from brittle GFRP laminates and ductile adhesives, Part I: Experimental investigation. *Composites Part B: Engineering*, *39*(2), 271-281.

de Castro, J., & Keller, T. (2008b). Ductile double-lap joints from brittle GFRP laminates and ductile adhesives, Part II: Numerical investigation and joint strength prediction. *Composites Part B: Engineering*, *39*(2), 282-291.

De Domenico, D., Fuschi, P., Pardo, S., & Pisano, A. A. (2014). Strengthening of steel-reinforced concrete structural elements by externally bonded FRP sheets and evaluation of their load carrying capacity. *Composite Structures*, *118*, 377-384.

De Felice, G., Aiello, M. A., Caggegi, C., Ceroni, F., De Santis, S., Garbin, E., ... & Leone, M. (2018). Recommendation of RILEM Technical Committee 250-CSM: Test method for Textile Reinforced Mortar to substrate bond characterization. *Materials and Structures*, *51*(4), 95.

Di Tommaso, A., Neubauer, U., Pantuso, A., & Rostasy, F. S. (2001). Behavior of adhesively bonded concrete-CFRP joints at low and high temperatures. *Mechanics of Composite Materials*, *37*(4), 327-338.

Dispenza, C. A. A. P., Pisano, A. A., & Fuschi, P. (2006). Numerical simulations of the mechanical characteristics of glass fibre reinforced C-profiles. Composites science and technology, 66(15), 2980-2989.

Dong, J., Wang, Q., & Guan, Z. (2013). Structural behaviour of RC beams with external flexural and flexural–shear strengthening by FRP sheets. *Composites Part B: Engineering*, *44*(1), 604-612.

Ebead, U., Shrestha, K. C., Afzal, M. S., El Refai, A., & Nanni, A. (2016). Effectiveness of fabric-reinforced cementitious matrix in strengthening reinforced concrete beams. *Journal of Composites for Construction*, *21*(2), 04016084.

Focacci, F., D'Antino, T., Carloni, C., Sneed, L. H., & Pellegrino, C. (2017). An indirect method to calibrate the interfacial cohesive material law for FRCM-concrete joints. *Materials & Design*, *128*, 206-217.

Foraboschi, P. (2007). Behavior and failure strength of laminated glass beams. *Journal of Engineering Mechanics*, *133*(12), 1290-1301.

Fossetti, M., Alotta, G., Basone, F., & Macaluso, G. (2017). Simplified analytical models for compressed concrete columns confined by FRP and FRCM system. *Materials and Structures*, *50*(6), 240.

Ghiassi, B., Lourenço, P. B., & Oliveira, D. V. (2014). Accelerated hygrothermal aging of bond in FRP–masonry systems. *Journal of Composites for Construction*, *19*(3), 04014051.

Ghiassi, B., Marcari, G., Oliveira, D. V., & Lourenço, P. B. (2013). Water degrading effects on the bond behavior in FRP-strengthened masonry. *Composites Part B: Engineering*, *54*, 11-19.

Giampaoli, M., Terlizzi, V., Rossi, M., Chiappini, G., & Munafò, P. (2017). Mechanical performances of GFRP-steel specimens bonded with different epoxy adhesives, before and after the aging treatments. *Composite structures*, *171*, 145-157.

Godat, A., Légeron, F., Gagné, V., & Marmion, B. (2013). Use of FRP pultruded members for electricity transmission towers. *Composite Structures*, *105*, 408-421.

Gonzalez-Libreros, J. H., Sabau, C., Sneed, L. H., Pellegrino, C., & Sas, G. (2017b). State of research on shear strengthening of RC beams with FRCM composites. *Construction and Building Materials*, *149*, 444-458.

Gonzalez-Libreros, J. H., Sneed, L. H., D'Antino, T., & Pellegrino, C. (2017a). Behavior of RC beams strengthened in shear with FRP and FRCM composites. *Engineering Structures*, *150*, 830-842.

Gu, Y. C., Jung, J., Yang, Q. D., & Chen, W. Q. (2015). An inertia-based stabilizing method for quasi-static simulation of unstable crack initiation and propagation. *Journal of Applied Mechanics*, *82*(10), 101010.

Hollaway, L. C. (2010). A review of the present and future utilisation of FRP composites in the civil infrastructure with reference to their important in-service properties. *Construction and building materials*, *24*(12), 2419-2445.

Keller, T. (2001). Recent all-composite and hybrid fibre-reinforced polymer bridges and buildings. *Progress in Structural Engineering and Materials*, *3*(2), 132-140.

Kim, H. Y., & Lee, S. Y. (2012). A steel-reinforced hybrid GFRP deck panel for temporary bridges. *Construction and Building Materials*, *34*, 192-200.

Liu, W., Schesser, D., Yang, Q. D., & Ling, D. S. (2015). A consistency-check based algorithm for element condensation in augmented finite element methods for fracture analysis. *Engineering Fracture Mechanics*, *139*, 78-97.

Liu, W., Yang, Q. D., Mohammadizadeh, S., & Su, X. Y. (2014). An efficient augmented finite element method for arbitrary cracking and crack interaction in solids. *International Journal for Numerical Methods in Engineering*, *99*(6), 438-468.

Liu, W., Yang, Q. D., Mohammadizadeh, S., Su, X. Y., & Ling, D. S. (2013). An accurate and efficient augmented finite element method for arbitrary crack interactions. *Journal of Applied Mechanics*, *80*(4), 041033.

Loreto, G., Babaeidarabad, S., Leardini, L., & Nanni, A. (2015). RC beams shear-strengthened with fabric-reinforced-cementitious-matrix (FRCM) composite. *International Journal of Advanced Structural Engineering (IJASE)*, *7*(4), 341-352.

Machalická, K., & Eliášová, M. (2017). Adhesive joints in glass structures: effects of various materials in the connection, thickness of the adhesive layer, and ageing. *International Journal of Adhesion and Adhesives*, *72*, 10-22.

Marcinczak, D., Trapko, T., & Musiał, M. (2019). Shear strengthening of reinforced concrete beams with PBO-FRCM composites with anchorage. *Composites Part B: Engineering*, *158*, 149-161.

Marques, E. A. S., da Silva, L. F., Banea, M. D., & Carbas, R. J. C. (2015). Adhesive joints for low-and high-temperature use: an overview. *The Journal of Adhesion*, *91*(7), 556-585.

Mazzotti, C., Ferracuti, B., & Bellini, A. (2015). Experimental bond tests on masonry panels strengthened by FRP. *Composites Part B: Engineering*, *80*, 223-237.

Mazzotti, C., Savoia, M., & Ferracuti, B. (2008). An experimental study on delamination of FRP plates bonded to concrete. *Construction and Building Materials*, *22*(7), 1409-1421.

Mazzotti, C., Savoia, M., & Ferracuti, B. (2009). A new single-shear set-up for stable debonding of FRP–concrete joints. Construction and Building Materials, 23(4), 1529-1537.

McIsaac, A., Mak, K., & Fam, A. (2019). Influence of Resin Biocontent and Type on Bond Strength between FRP Wet Layup and Concrete. *Journal of Composites for Construction*, *23*(4), 04019029.

Moës, N., & Belytschko, T. (2002). Extended finite element method for cohesive crack growth. *Engineering fracture mechanics*, *69*(7), 813-833.

Naderi, M., Jung, J., & Yang, Q. D. (2016). A three dimensional augmented finite element for modeling arbitrary cracking in solids. *International Journal of Fracture*, *197*(2), 147-168.

National Research Council (2014) CNR-DT 210, Istruzioni per la Progettazione, l'Esecuzione ed il Controllo delle Strutture di Vetro. Rome, Italy

National Research Council. (2013). CNR-DT 200. R1: Istruzioni per la Progettazione, l'Esecuzione ed il Controllo di Interventi di Consolidamento Statico mediante l'utilizzo di Compositi Fibrorinforzati, Rome, Italy

National Research Council. (2018) CNR-DT 215, Istruzioni per la progettazione, l'esecuzione ed il controllo di interventi di consolidamento statico mediante l'utilizzo di compositi fibrorinforzati a matrice inorganica, Rome, Italy

NTC, L. G. (2008). Norme tecniche per le costruzioni. *Italian Technical Norms for Constructions.*

NTC, L. G. (2018). Norme tecniche per le costruzioni. *Italian Technical Norms for Constructions.*

Ombres, L. (2012). Debonding analysis of reinforced concrete beams strengthened with fibre reinforced cementitious mortar. *Engineering Fracture Mechanics*, *81*, 94-109.

Ombres, L. (2014). Concrete confinement with a cement based high strength composite material. *Composite Structures*, *109*, 294-304.

Overend, M., Jin, Q., & Watson, J. (2011). The selection and performance of adhesives for a steel–glass connection. *International Journal of Adhesion and Adhesives*, *31*(7), 587-597.

Papanicolaou, C. G., Triantafillou, T. C., Karlos, K., & Papathanasiou, M. (2007). Textile-reinforced mortar (TRM) versus FRP as strengthening material of URM walls: in-plane cyclic loading. *Materials and structures*, *40*(10), 1081-1097.

Papanicolaou, C. G., Triantafillou, T. C., Papathanasiou, M., & Karlos, K. (2008). Textile reinforced mortar (TRM) versus FRP as strengthening material of URM walls: out-of-plane cyclic loading. *Materials and structures*, *41*(1), 143-157.

Qureshi, J., & Mottram, J. T. (2013). Behaviour of pultruded beam-to-column joints using steel web cleats. *Thin-Walled Structures*, *73*, 48-56.

Raoof, S. M., & Bournas, D. A. (2017a). Bond between TRM versus FRP composites and concrete at high temperatures. *Composites Part B: Engineering*, *127*, 150-165.

Raoof, S. M., & Bournas, D. A. (2017b). TRM versus FRP in flexural strengthening of RC beams: Behaviour at high temperatures. *Construction and Building Materials*, *154*, 424-437.

Raoof, S. M., Koutas, L. N., & Bournas, D. A. (2016). Bond between textile-reinforced mortar (TRM) and concrete substrates: Experimental investigation. *Composites Part B: Engineering*, *98*, 350-361.

Raoof, S. M., Koutas, L. N., & Bournas, D. A. (2017c). Textile-reinforced mortar (TRM) versus fibre-reinforced polymers (FRP) in flexural strengthening of RC beams. *Construction and Building Materials*, *151*, 279-291.

Ruredil, X. (2009). Mesh gold data sheet. *Ruredil SPA, Milan, Italy*.

San Román, J. D. C. (2005). Experiments on Double-lap Joints with Epoxy, Polyurethane and ADP Adhesives. *Composite Structure Laboratory*, *1*, 2.

Sciolti, M. S., Frigione, M., & Aiello, M. A. (2010). Wet lay-up manufactured FRPs for concrete and masonry repair: influence of water on the properties of composites and on their epoxy components. *Journal of Composites for Construction*, *14*(6), 823-833.

Sneed, L. H., D'Antino, T., & Carloni, C. (2014). Investigation of bond behavior of PBO fiber-reinforced cementitious matrix composite-concrete interface. *ACI Mater J*, *111*(5), 569-580.

Sneed, L. H., D'Antino, T., Carloni, C., & Pellegrino, C. (2015). A comparison of the bond behavior of PBO-FRCM composites determined by double-lap and single-lap shear tests. *Cement and Concrete Composites*, *64*, 37-48.

Speranzini, E., & Agnetti, S. (2013). Post-cracking behaviour of reinforced glass beams. In *COST Action TU0905 Mid-Term Conference on Structural Glass; CRC Press: Boca Raton, FL, USA* (pp. 285-292).

Srivastava, V. K. (2003). Characterization of adhesive bonded lap joints of C/C–SiC composite and Ti–6Al–4V alloy under varying conditions. *International journal of adhesion and adhesives*, *23*(1), 59-67.

Stazi, F., Giampaoli, M., Nisi, L., Rossi, M., & Munafò, P. (2016a). Mechanical performance reduction of GFRP specimens with polyester matrix exposed to continuous condensation. *Composites Part B: Engineering*, *99*, 330-339.

Stazi, F., Giampaoli, M., Rossi, M., & Munafò, P. (2015). Environmental ageing on GFRP pultruded joints: comparison between different adhesives. *Composite Structures*, *133*, 404-414.

Stazi, F., Giampaoli, M., Tittarelli, F., Di Perna, C., & Munafò, P. (2016b). Durability of different glass coatings in humid and saline environments, ageing impact on heat-light transmission and thermal comfort. *Building and Environment*, *105*, 210-224.

Tetta, Z. C., & Bournas, D. A. (2016). TRM vs FRP jacketing in shear strengthening of concrete members subjected to high temperatures. *Composites Part B: Engineering*, *106*, 190-205.

Toutanji, H. A., & Gomez, W. (1997). Durability characteristics of concrete beams externally bonded with FRP composite sheets. *Cement and Concrete Composites*, *19*(4), 351-358.

Trapko, T., Urbańska, D., & Kamiński, M. (2015). Shear strengthening of reinforced concrete beams with PBO-FRCM composites. *Composites Part B: Engineering*, *80*, 63-72.

Triantafillou, T. C., & Papanicolaou, C. G. (2006). Shear strengthening of reinforced concrete members with textile reinforced mortar (TRM) jackets. *Materials and structures*, *39*(1), 93-103.

Turvey, G. J. (2013). Testing of pultruded glass fibre-reinforced polymer (GFRP) composite materials and structures. In *Advanced Fibre-Reinforced Polymer (FRP) Composites for Structural Applications* (pp. 440-508). Woodhead Publishing.

Turvey, G. J., & Zhang, Y. (2006). Characterisation of the rotational stiffness and strength of web-flange junctions of pultruded GRP WF-sections via web bending tests. *Composites Part A: applied science and manufacturing*, *37*(2), 152-164.

UNI EN 10025-2:2005 Hot rolled products of structural steels - Part 2: Technical delivery conditions for non-alloy structural steels.

UNI EN 12390-5:2009 Prove sul calcestruzzo indurito - Parte 5: Resistenza a flessione dei provini

UNI EN 1992-1-1:2015 Eurocodice 2 - Progettazione delle strutture di calcestruzzo - Parte 1-1: Regole generali e regole per gli edifici

UNI EN 755-2:2016 Aluminium and aluminium alloys - Extruded rod/bar, tube and profiles - Part 2: Mechanical properties.

UNI EN ISO 527-1:2012Materie plastiche - Determinazione delle proprietà a trazione - Parte 1: Principi generali

UNI EN ISO 527-2:2012 Materie plastiche - Determinazione elle proprietà a trazione – Parte 2: Condizioni di prova per materie plastiche per stampaggio ed estrusione

Urso, S., Hadad, H. A., Borsellino, C., Recupero, A., Yang, Q. D., & Nanni, A. (2019). Numerical Modelling of FRCM Materials Using Augmented-FEM. In *Key Engineering Materials* (Vol. 817, pp. 23-29). Trans Tech Publications Ltd.

Viana, G. M. S. O., Costa, M., Banea, M. D., & Da Silva, L. F. M. (2017). A review on the temperature and moisture degradation of adhesive joints. *Proceedings of the Institution of Mechanical Engineers, Part L: Journal of Materials: Design and Applications*, *231*(5), 488-501.

Wu, C., & Bai, Y. (2014). Web crippling behaviour of pultruded glass fibre reinforced polymer sections. *Composite Structures*, *108*, 789-800.

Wu, C., Bai, Y., & Zhao, X. L. (2015). Improved bearing capacities of pultruded glass fibre reinforced polymer square hollow sections strengthened by thin-walled steel or CFRP. *Thin-Walled Structures*, *89*, 67-75.

Yang, Q. D., Cox, B. N., Nalla, R. K., & Ritchie, R. O. (2006). Fracture length scales in human cortical bone: the necessity of nonlinear fracture models. *Biomaterials*, *27*(9), 2095-2113.